# Jordan Journal of PHYSICS

# An International Peer-Reviewed Research Journal

# Volume 11, No. 2, August 2018, Thu Al-Hijjah 1439 H

**Jordan Journal of Physics** (*JJP*): An International Peer-Reviewed Research Journal funded by the Scientific Research Support Fund, Jordan, and published biannually by the Deanship of Research and Graduate Studies, Yarmouk University, Irbid, Jordan.

### **EDITOR-IN-CHIEF:**

# Ibrahim O. Abu Al-Jarayesh

Department of Physics, Yarmouk University, Irbid, Jordan. ijaraysh@yu.edu.jo

## **EDITORIAL BOARD:** ASSOCIATE EDITORIAL BOARD Prof. Dia-Eddin M. Arafah Prof. Mark Hagmann President, AL- al Bait University, Mafraq, Jordan. Desert Electronics Research Corporation, 762 Lacey darafah@ju.edu.jo Way, North Salt Lake 84064, Utah, U. S. A. MHagmann@NewPathResearch.Com. Prof. Nabil Y. Ayoub President, American University of Madaba, Madaba, Jordan. nabil.ayoub@gju.edu.jo **Prof. Richard Forbes** University of Surrey, FEPS (X1), Guildford, Surrey Prof. Jamil M. Khalifeh GU2 7XH, U. K. Department of Physics, University of Jordan, Amman, R.Forbes@surrey.ac.uk Jordan. jkalifa@ju.edu.jo **Prof. Roy Chantrell** Prof. Sami H. Mahmood Physics Department, The University of York, York, Department of Physics, University of Jordan, Amman, YO10 5DD, UK. Jordan. roy.chantrell@york.ac.uk s.mahmood@ju.edu.jo Prof. Nihad A. Yusuf Prof. Susamu Taketomi Princess Sumaya University for Technology, Amman, Jordan. 2-35-8 Higashisakamoto, Kagoshima City, 892-0861, E-mail: n.yusuf@psut.edu.jo staketomi@hotmail.com Prof. Marwan S. Mousa Department of Physics, Mu'tah University, Al-Karak, Jordan. mmousa@mutah.edu.jo Prof. Akram A. Rousan Department of Applied Physical Sciences, Jordan University Of Science and Technology, Irbid, Jordan. akram@just.edu.jo Prof. Mohammad Al-Sugheir Department of Physics, The HashemiteUniversity, Zarga, Jordan.

Editorial Secretary: Majdi Al-Shannaq. Manuscripts should be submitted to:

msugh@hu.edu.jo

Prof. Ibrahim O. Abu Al-Jarayesh Editor-in-Chief, Jordan Journal of Physics Deanship of Research and Graduate Studies Yarmouk University-Irbid-Jordan Tel. 00 962 2 7211111 Ext. 2075 E-mail: jjp@yu.edu.jo Website: http://Journals.yu.edu.jo/jjp

# Jordan Journal of

# PHYSICS

# An International Peer-Reviewed Research Journal

# Volume 11, No. 2, August 2018, Thu Al-Hijjah 1439 H

# INTERNATIONAL ADVISORY BOARD

### Prof. Dr. Ahmad Saleh

Department of Physics, Yarmouk University, Irbid, Jordan. salema@yu.edu.jo

# Prof. Dr. Aurore Savoy-Navarro

LPNHE Universite de Paris 6/IN2P3-CNRS, Tour 33, RdC 4, Place Jussieu, F 75252, Paris Cedex 05, France. auore@Ipnhep.in2p3.fr

### Prof. Dr. Bernard Barbara

Laboratoire Louis Neel, Salle/Room: D 108, 25, Avenue des Martyrs BP 166, 38042-Grenoble Cedex 9, France. Barbara@grenoble.cnrs.fr

### Prof. Dr. Bruno Guiderdoni

Observatoire Astronomique de Lyon, g, avenue Ch. Antre-F-69561, Saint Genis Laval Cedex, France.

<u>Bruno.guiderdoni@olos.univ-lyon1.fr</u>

# Prof. Dr. Buford Price

Physics Department, University of California, Berkeley, CA 94720, U.S.A.

bprice@berkeley.edu

### Prof. Dr. Colin Cough

School of Physics and Astronomy, University of Birmingham, B15 2TT, U. K.

c.gough@bham.ac.uk

# Prof. Dr. Desmond Cook

Department of Physics, Condensed Matter and Materials Physics Research Group, Old Dominion University, Norfolk, Virginia 23529, U. S. A.

Dcook@physics.odu.edu

# Prof. Dr. Evgeny Sheshin

MIPT, Institutskij per. 9, Dogoprudnyi 141700, Russia. sheshin@lafeet.mipt.ru

# Prof. Dr. Hans Ott

Laboratorium Fuer Festkorperphysik, ETH Honggerberg, CH-8093 Zurich, Switzerland. ott@solid.phys.ethz.ch

# Prof. Dr. Herwig Schopper

President SESAME Council, Chairman Scientific Board UNESCO IBSP Programme, CERN, 1211 Geneva, Switzerland. Herwig.Schopper@cern.ch

### Prof. Dr. Humam Ghassib

Department of Physics, The University of Jordan, Amman 11942, Jordan.

humamg@ju.edu.jo

### Prof. Dr. Khalid Touqan

Chairman of Jordan Atomic Energy Commission, Amman, Jordan.

### Prof. Dr. Nasr Zubeidey

President: Al-Zaytoonah University of Jordan, Amman, Jordan. President@alzaytoonah.edu.jo

# Prof. Dr. Patrick Roudeau

Laboratoire de l'Accelerateur, Lineaire (LAL), Universite Paris-Sud 11, Batiment 200, 91898 Orsay Cedex, France. roudeau@mail.cern.ch

# Prof. Dr. Paul Chu

Department of Physics, University of Houston, Houston, Texas 77204-5005, U. S. A.

Ching-Wu.Chu@mail.uh.edu

### Prof. Dr. Peter Dowben

Nebraska Center for Materials and Nanoscience, Department of Physics and Astronomy, 255 Behlen Laboratory (10th and R Streets), 116 Brace Lab., P. O. Box 880111, Lincoln, NE 68588-0111, U. S. A.

pdowben@unl.edu

### Prof. Dr. Peter Mulser

Institute fuer Physik, T.U. Darmstadt, Hochschulstr. 4a, 64289 Darmstadt, Germany.

Peter.mulser@physik.tu-darmstadt.de

# Prof. Dr. Rasheed Azzam

Department of Electrical Engineering, University of New Orleans New Orleans, Louisiana 70148, U. S. A. razzam@uno.edu

# Prof. Dr. Shawqi Al-Dallal

Department of Physics, Faculty of Science, University of Bahrain, Manamah, Kingdom of Bahrain.

# Prof. Dr. Wolfgang Nolting

Institute of Physics / Chair: Solid State Theory, Humboldt-University at Berlin, Newtonstr. 15 D-12489 Berlin, Germany Wolfgang.nolting@physik.hu-berlin.de

# Prof. Dr. Ingo Hofmann

GSI Darmstadt, Planckstr. 1, 64291, Darmstadt, Germany. <u>i.hofmann@gsi.de</u>

# Prof. Dr. Jozef Lipka

Department of Nuclear Physics and Technology, Slovak University of Technology, Bratislava, Ilkovicova 3, 812 19 Bratislava, Slovakia.

Lipka@elf.stuba.sk





Yarmouk University

# Jordan Journal of PHYSICS

An International Peer-Reviewed Research Journal Funded by the Scientific Research Support Fund

# **Instructions to Authors**

Instructions to authors concerning manuscript organization and format apply to hardcopy submission by mail, and also to electronic online submission via the Journal homepage website (http://jip.yu.edu.jo).

# **Manuscript Submission**

1- E-mail to: jjp@yu.edu.jo

2- Online: Follow the instructions at the journal homepage website.

Original Research Articles, Communications and Technical Notes are subject to critical review by minimum of two competent referees. Authors are encouraged to suggest names of competent reviewers. Feature Articles in active Physics research fields, in which the author's own contribution and its relationship to other work in the field constitute the main body of the article, appear as a result of an invitation from the Editorial Board, and will be so designated. The author of a Feature Article will be asked to provide a clear, concise and critical status report of the field as an introduction to the article. Review Articles on active and rapidly changing Physics research fields will also be published. Authors of Review Articles are encouraged to submit two-page proposals to the Editor-in-Chief for approval. Manuscripts submitted in Arabic should be accompanied by an Abstract and Keywords in English.

# **Organization of the Manuscript**

Manuscripts should be typed double spaced on one side of A4 sheets (21.6 x 27.9 cm) with 3.71 cm margins, using Microsoft Word 2000 or a later version thereof. The author should adhere to the following order of presentation: Article Title, Author(s), Full Address and E-mail, Abstract, PACS and Keywords, Main Text, Acknowledgment. Only the first letters of words in the Title, Headings and Subheadings are capitalized. Headings should be in **bold** while subheadings in *italic* fonts.

**Title Page:** Includes the title of the article, authors' first names, middle initials and surnames and affiliations. The affiliation should comprise the department, institution (university or company), city, zip code and state and should be typed as a footnote to the author's name. The name and complete mailing address, telephone and fax numbers, and e-mail address of the author responsible for correspondence (designated with an asterisk) should also be included for official use. The title should be carefully, concisely and clearly constructed to highlight the emphasis and content of the manuscript, which is very important for information retrieval.

**Abstract:** A one paragraph abstract not exceeding 200 words is required, which should be arranged to highlight the purpose, methods used, results and major findings.

**Keywords:** A list of 4-6 keywords, which expresses the precise content of the manuscript for indexing purposes, should follow the abstract.

**PACS:** Authors should supply one or more relevant PACS-2006 classification codes, (available at http://www.aip.org/pacs/pacs06/pacs06-toc.html)

**Introduction:** Should present the purpose of the submitted work and its relationship to earlier work in the field, but it should not be an extensive review of the literature (e.g., should not exceed 1 ½ typed pages).

**Experimental Methods:** Should be sufficiently informative to allow competent reproduction of the experimental procedures presented; yet concise enough not to be repetitive of earlier published procedures.

**Results:** should present the results clearly and concisely.

**Discussion**: Should be concise and focus on the interpretation of the results.

**Conclusion:** Should be a brief account of the major findings of the study not exceeding one typed page.

**Acknowledgments:** Including those for grant and financial support if any, should be typed in one paragraph directly preceding the References.

**References:** References should be typed double spaced and numbered sequentially in the order in which they are cited in the text. References should be cited in the text by the appropriate Arabic numerals, enclosed in square brackets. Titles of journals are abbreviated according to list of scientific periodicals. The style and punctuation should conform to the following examples:

# 1. Journal Article:

- a) Heisenberg, W., Z. Phys. 49 (1928) 619.
- b) Bednorz, J. G. and Müller, K. A., Z. Phys. B64 (1986) 189
- c) Bardeen, J., Cooper, L.N. and Schrieffer, J. R., Phys. Rev. 106 (1957) 162.
- d) Asad, J. H., Hijjawi, R. S., Sakaji, A. and Khalifeh, J. M., Int. J. Theor. Phys. 44(4) (2005), 3977.

# 2. Books with Authors, but no Editors:

- a) Kittel, C., "Introduction to Solid State Physics", 8th Ed. (John Wiley and Sons, New York, 2005), chapter 16.
- b) Chikazumi, S., C. D. Graham, JR, "Physics of Ferromagnetism", 2<sup>nd</sup> Ed. (Oxford University Press, Oxford, 1997).

# 3. Books with Authors and Editors:

- a) Allen, P. B. "Dynamical Properties of Solids", Ed. (1), G. K. Horton and A. A. Maradudin (North-Holland, Amsterdam, 1980), p137.
- b) Chantrell, R. W. and O'Grady, K., "Magnetic Properities of Fine Particles" Eds. J. L. Dormann and D. Fiorani (North-Holland, Amsterdam, 1992), p103.

# 4. Technical Report:

Purcell, J. "The Superconducting Magnet System for the 12-Foot Bubble Chamber", report ANL/HEP6813, Argonne Natt. Lab., Argonne, III, (1968).

# 5. Patent:

Bigham, C. B., Schneider, H. R., US patent 3 925 676 (1975).

# 6. Thesis:

Mahmood, S. H., Ph.D. Thesis, Michigan State University, (1986), USA (Unpublished).

# 7. Conference or Symposium Proceedings:

Blandin, A. and Lederer, P. Proc. Intern. Conf. on Magnetism, Nottingham (1964), P.71.

## 8. Internet Source:

Should include authors' names (if any), title, internet website, URL, and date of access.

# 9. Prepublication online articles (already accepted for publication):

Should include authors' names (if any), title of digital database, database website, URL, and date of access.

For other types of referenced works, provide sufficient information to enable readers to access them.

**Tables:** Tables should be numbered with Arabic numerals and referred to by number in the Text (e.g., Table 1). Each table should be typed on a separate page with the legend above the table, while explanatory footnotes, which are indicated by superscript lowercase letters, should be typed below the table.

Illustrations: Figures, drawings, diagrams, charts and photographs are to be numbered in a consecutive series of Arabic numerals in the order in which they are cited in the text. Computer-generated illustrations and good-quality digital photographic prints are accepted. They should be black and white originals (not photocopies) provided on separate pages and identified with their corresponding numbers. Actual size graphics should be provided, which need no further manipulation, with lettering (Arial or Helvetica) not smaller than 8 points, lines no thinner than 0.5 point, and each of uniform density. All colors should be removed from graphics except for those graphics to be considered for publication in color. If graphics are to be submitted digitally, they should conform to the following minimum resolution requirements: 1200 dpi for black and white line art, 600 dpi for grayscale art, and 300 dpi for color art. All graphic files must be saved as TIFF images, and all illustrations must be submitted in the actual size at which they should appear in the journal. Note that good quality hardcopy original illustrations are required for both online and mail submissions of manuscripts.

**Text Footnotes:** The use of text footnotes is to be avoided. When their use is absolutely necessary, they should be typed at the bottom of the page to which they refer, and should be cited in the text by a superscript asterisk or multiples thereof. Place a line above the footnote, so that it is set off from the text.

**Supplementary Material:** Authors are encouraged to provide all supplementary materials that may facilitate the review process, including any detailed mathematical derivations that may not appear in whole in the manuscript.

# **Revised Manuscript and Computer Disks**

Following the acceptance of a manuscript for publication and the incorporation of all required revisions, authors should submit an original and one more copy of the final disk containing the complete manuscript typed double spaced in Microsoft Word for Windows 2000 or a later version thereof. All graphic files must be saved as PDF, JPG, or TIFF images.

Allen, P.B., "..., in: Horton, G.K., and Muradudin, A. A., (eds.), "Dynamical.....", (North......), pp....

# **Reprints**

Twenty (20) reprints free of charge are provided to the corresponding author. For orders of more reprints, a reprint order form and prices will be sent with the article proofs, which should be returned directly to the Editor for processing.

# Copyright

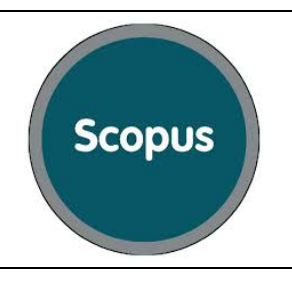
Submission is an admission by the authors that the manuscript has neither been previously published nor is being considered for publication elsewhere. A statement transferring copyright from the authors to Yarmouk University is required before the manuscript can be accepted for publication. The necessary form for such transfer is supplied by the Editor-in-Chief. Reproduction of any part of the contents of a published work is forbidden without a written permission by the Editor-in-Chief.

# Disclaimer

Opinions expressed in this Journal are those of the authors and neither necessarily reflects the opinions of the Editorial Board or the University, nor the policy of the Higher Scientific Research Committee or the Ministry of Higher Education and Scientific Research. The publisher shoulders no responsibility or liability whatsoever for the use or misuse of the information published by JJP.

# Indexing

JJP is currently indexing in:



**Emerging Sources Citation Index** (ESCI)



# Jordan Journal of $\mathbb{P} \ \mathbb{H} \ \mathbb{Y} \ \mathbb{S} \ \mathbb{I} \ \mathbb{C} \ \mathbb{S}$

# An International Peer-Reviewed Research Journal

# Volume 11, No. 2, August 2018, Thu Al-Hijjah 1439 H

# Table of Contents:

English Articles	Pages
Transport Theory of Muonic Atoms in Hydrogen Isotope Media	
M. Mahdavi	77-84
<sup>226</sup> Ra, <sup>228</sup> Ra and <sup>40</sup> K Concentrations in Some Plant Seeds Consumed in	
Jordan	85-90
Khaled A. Al-Khaza'leh	
Growth Inhibition of Natural Foods on Calcium Hydrogen Phosphate Dihydrate Crystals	91-99
G. Anushya and T.H. Freeda	
Photoluminescence Behavior of $Cu_{2+x}Zn_{1-x}SnS_4$ Thin Films by SILAR Method	101-105
J. Henry, K. Mohanraj and G. Sivakumar	
Dielectric Relaxation Studies on Binary Polar Mixtures of Diethylene Glycol with Ethyl Benzoate Using Time Domain Reflectometry  K. Umamakeshvari, A. Mohan, U. Sankar and A.Mozes Ezhil Raj	107-114
Analysis of the Force Exerted on an Accelerated Beam of Electrons by Its Own Wakefield in the Laser-Driven Rf-gun  N. M. Ershaidat and W. Salah	115-124
Communications	Pages
Synthesis and Characterization of Monovalent, Divalent and Trivalent Cation Doping of Cu <sub>2</sub> Se Thin Films Using Chemical Bath Deposition Method	125-130
A. P. Sudha, J. Henry, K. Mohanraj and G. Sivakumar	
Hydrothermally Synthesized CoSn(OH) <sub>6</sub> Nanoparticles for Electrochemical Performance	131-135
V. K. Premkumar and G. Sivakumar	
Synthesis and Characterization of CuMS <sub>2</sub> (M= Bi, Sb) Thin Films Prepared by CBD Method  T. Daniel, K. Mohanraj and G. Sivakumar	137-139

# Jordan Journal of Physics

# **ARTICLE**

# Transport Theory of Muonic Atoms in Hydrogen Isotope Media

# M. Mahdavi

Physics Department, University of Mazandaran, P.O.Box 47415-416, Babolsar, Iran.

Received on: 27/2/2017; Accepted on: 8/10/2017

Abstract: The resonance muonic molecular formation is highly dependent on the energy of muonic atoms. The energy loss of muonic atoms depends on the range of distance traveled in a medium. The resonance molecular formation rate for  $\mu$ dt is maximum if the kinetic energy of the muonic atoms (such as  $\mu$ t) which enter the  $D_2$  medium is in the range of 0.4-0.6 eV. In this research, the transport theory is used to study the effect of thickness of the suggested multi-layer system (H/T and  $D_2$ ) on the output kinetic energy of the muonic atoms,  $\mu$ t. The optimum thickness of multi-layer system is also calculated for  $\mu$ dt resonance formation. Finally, the obtained results of the used theoretical method are compared with the experimental results. It is shown that the used transport theory is a good and acceptable theory for studying the transport of muonic atoms in hydrogen isotope media.

**Keywords:** Transport theory, Muonic atoms, Resonance molecular formation, Thickness layers.

**PACS**: 36.10.Ee; 72.10.Bg; 31.30.jr.

# Introduction

When a negative muon is injected into a hydrogen target, it will slow down and form a small atomic system, muonic deuterium atom, ud or muonic tritium atom, ut, by replacing the electron in the atom. If a muonic deuterium atom, µd, is formed, the muon will be transferred to a tritium atom, due to its deeper Coulomb potential. The muonic tritium atom, ut, will collide with a deuterium molecule and form the muonic molecule µdt. Molecular formation occurs predominantly via a resonant mechanism, in which the energy released from the formation of the udt molecule is absorbed in the rotational and vibrational excitation of the molecular complex [(µdt)dee], where the compact object udt acts as a pseudonucleus. Because the size of the muonic molecule is smaller than that of ordinary molecules by its mass ratio (m<sub>u</sub>/m<sub>e</sub>) in zeroth order, the internuclear distance in udt is small enough for the fusion to take place within

 $10^{-12}$  s; a phenomenon known as muon catalyzed fusion (µCF)[1,2].

The target of a suggested solid heterogeneous multi-layer H/D/T is shown in Fig.1. When a negative muon enters the first layer of hydrogen (H/T) with a small admixture of tritium (concentration ratio,  $c_t \approx 0.001$ ), the muons are initially captured in excited atomic states of muonic hydrogen (µp or µt) in a characteristic time of pico-seconds. The subsequent deexcitation of the muonic atom occurs *via* Stark, Auger, scattering, radiative and transfer processes, which occur on the 100 ps time scale and the µp atom reaches its ground state (1s)[3, 4]. Because of the impurity (of tritium), transfer from the lighter to the heavier isotopes competes with de-excitation to ground state as[5];

$$(\mu p)_n + t \rightarrow (\mu t)_n + p + \frac{183}{n^2} eV$$
 (1)

where n is an excitation level. Elastic collisions moderate the energy of  $\mu t$  or  $\mu d$  atoms until

Corresponding Author: M. Mahdavi Email: m.mahdavi@umz.ac.ir

Article Mahdavi

thermal equilibrium is established with the surrounding medium. The muonic atoms have a kinetic energy of about 45 eV, which they subsequently lose *via* elastic collisions, mainly with protium, until they reach 20-30 eV, when the scattering cross-section falls below  $10^{-20}$  cm<sup>2</sup>, Fig. 2 [6, 7]. The mean distance between collisions becomes very large, especially at 4-20 eV and the hydrogen layer becomes effectively transparent to the muonic atoms. In all solid muonic hydrogen systems, thermalization at very low energies is inhibited, because the muonic atom interacts elastically with hydrogen "fcc" crystal (a lattice structure), which cannot absorb the kinetic energy efficiently [8]. This effect is

Ramsauer-Townsend due to mechanism. Thermalization is much slower and the muonic atoms travel appreciable distances. In a thin solid layer, the µt atoms may escape from the H/T layer into the first D<sub>2</sub> layer with a high probability [9]. Since the size of the µt is almost 9 times larger than the neutron, the transport theory for  $\mu t$  atom in the H/T and D<sub>2</sub> layers is used in this research in the same manner as the neutron interacts on hydrogen media. In the present work, a calculation method is introduced to estimate an appropriate thickness for the targets.

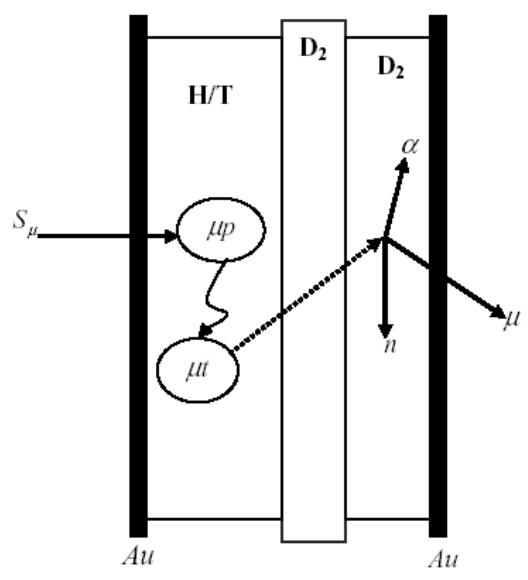


FIG. 1. The design of solid heterogeneous H/D/T mixture.

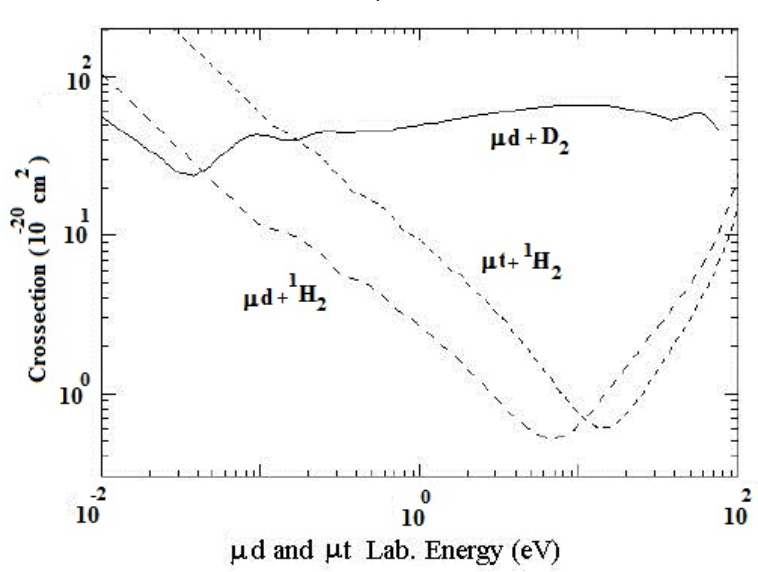


FIG. 2. The elastic scattering cross-section of μt and μd with H<sub>2</sub> and D<sub>2</sub> molecules versus lab. kinetic energy [13].

# Macroscopic Cross-Section of μt Atoms in Multi-Layer Hydrogen Isotopes

The muonic atom in passing through the H/T layer has elastic and inelastic interactions with the target (protium and tritium). The \$\mu t\$ loses its energy mainly by elastic collisions on protons until it reaches an energy range around 10 eV, where by the μt + p scattering, the μt atom either finds the chance to escape into the first D<sub>2</sub> layer (moderation layer) or muonic molecules such as utt and upt are formed. The non-resonance formation rate of the muonic molecules is much smaller than the resonance formation rate of complex molecules. Also, the resonance formation rate of these molecules is smaller than the elastic scattering rate of ut in the H/T layer. Hence, the transport equation can be applied for  $\mu t$  in the H/T layer as a weak absorbing medium, with a good approximation [9]. The macroscopic absorption cross-section in the H/T layer can be written as follows:

$$\Sigma_a = \Sigma_{utt} + \Sigma_{unt} \tag{2}$$

 $\Sigma_{\mu tt}$  and  $\Sigma_{\mu pt}$  are the macroscopic cross-sections. Also, we have:

$$\Sigma_{\mu ij} = \sigma_{\mu ij} N \tag{3}$$

where N is the atom density of the projectile therein,  $\sigma_{\mu ij}$  is the microscopic cross-section of  $\mu ij$  (i and j are hydrogen isotopes) muonic molecular formation. The muonic molecular formation rate of  $\mu tj$  (j is a hydrogen isotope) is given by [10]:

$$\lambda_{uti} = \rho \, v_{ut} \, \sigma_{uti} \tag{4}$$

where  $v_{\mu t}$  is the relative velocity of  $\mu t$  in the H/T layer and  $\rho$  is the density of target. According to classical kinetic energy,  $(E_{\mu t} = \frac{1}{2} m_{\mu t} v^2)$ . Using Eqs. (3) and (4), we have:

$$\Sigma_{\mu t j}(E) = \left(\frac{m_{\mu t}}{2}\right)^{\frac{1}{2}} (E_{\mu t})^{-1/2} \frac{N \lambda_{\mu t j}}{\rho}$$
 (5)

where  $m_{\mu t}$  and  $E_{\mu t}$  are the mass and kinetic energy of muonic tritium atom, respectively.

# Energy Loss theory of µt Atoms in Multi-Layer Hydrogen Isotopes

Suppose that the muonic tritium atom ( $\mu$ t) with a mass of  $m_{\mu\tau}$  and kinetic energy  $E_1$  has an elastic collision with a target at rest (first layer; protium or tritium, mass of  $m_p$  in the H/T layer). The kinetic energy of  $\mu$ t after collision  $E_2$  can be written as:

$$E_2 = \frac{1 + A^2 + 2A\cos\psi}{(1 + A)^2} E_1 . \tag{6}$$

The angle of scattering in the lab.,  $\theta$ , and C. m.,  $\Psi$  systems are related as follows:

$$\cos\theta = \frac{A + \cos\psi}{(1 + A^2 + 2A\cos\psi)^{1/2}} \tag{7}$$

Considering the  $\alpha$  parameter as:

$$\alpha = \left(\frac{m_{\mu t} - m_p}{m_{\mu t} + m_p}\right)^2 = \left(\frac{A - 1}{A + 1}\right)^2 \tag{8}$$

The energy of  $\mu t$  after collision is:

$$E_1 = \frac{1}{2}[(1+\alpha) + (1-\alpha)\cos\Psi]$$
 (9)

According to Eq. (9), the energy of the muonic atom after collision is dependent on the angle of scattering in the C.m. system. Therefore, the probability of the  $\mu$ t atom with initial energy  $E_1$  to reach  $E_2$  and  $E_2 + dE_2$  after collision can be written as:

$$g(E_1 \rightarrow E_2) dE_2 = P(\cos \Psi) d(\cos \Psi)$$
 (10)

The right side of Eq. (10) is the probability that the cosine of the scattering angle be between  $\cos \Psi$  and  $\cos \Psi + d \cos \Psi$  in the C.m. system. Since the hydrogen medium is a good moderator, it is supposed that the elastic scattering is isotropic in the C.m. system, then we have  $P(\cos \Psi) = \frac{1}{2}$ . Hence, we have:

$$g(E_1 \to E_2) dE_2 = \frac{1}{2} d(\cos \Psi)$$
  
 $g(E_1 \to E_2) = \frac{1}{2} \frac{d(\cos \Psi)}{dE_2} = \frac{1}{(1-\alpha)E_1}$  (11)

The average angle of scattering in the lab. system,  $\overline{\cos \theta}$ , can be calculated as follows:

$$\overline{\cos\theta} = \int_{-1}^{+1} \cos\theta \, P(\cos\Psi) d(\cos\Psi)$$

$$= \int_{-1}^{+1} \frac{(A + \cos\psi)}{2\sqrt{1 + A^2 + 2\alpha\cos\Psi}} \, d(\cos\psi) = 1 - \frac{2}{3A^2}$$
(12)

Article Mahdavi

Therefore, the forward scattering angle for the scattering of the  $\mu t$  atom in the H/T layer in the lab. system is  $\cos \theta = 0.93$ . The average energy of the  $\mu t$  atom in the interval of one collision,  $\overline{E}_2$  can be calculated as:

$$\overline{E_{2}} = \int_{\alpha E_{1}}^{E_{1}} E_{2} g(E_{1} \to E_{2}) dE_{2} = \int_{\alpha E_{1}}^{E_{1}} \frac{E_{2} dE_{2}}{(1-\alpha)E_{1}} = 0.63E1 \tag{13}$$

The average reduced energy per collision is equal to:

$$\Delta E = \overline{E_1 - E_2} = \frac{(1 - \alpha)}{2} E_1 = 0.37 E_1$$
 (14)

and the average reduced logarithmic energy,  $\xi$  is defined by:

$$\xi = \overline{ln\frac{E_1}{E_2}} = 1 + \frac{\alpha}{1+\alpha} \ln\alpha \tag{15}$$

For the  $\mu$ t atom in the H/T layer, the transport equation can be written as:

$$\frac{\partial J(\vec{r},E)}{\partial x} + \Sigma_{t}\Phi(\vec{r},E) = \int_{E}^{45} \Sigma_{s}(E' \to E' \Phi r, E' dE' + Sr, E)$$
(16)

where J,  $\Phi$  and S are the current density, flux and power source of  $\mu t$  atom in H/T layer, respectively.

# Energy Loss of ut Atoms in the H/T Layer

The flux of muonic atoms in the H/T layer is calculated supposing that the Fick's low is valid in the H/T layer; namely:

$$\vec{I}(\vec{r}, E) = -D(E)\vec{\nabla}(\vec{r}, E) \tag{17}$$

D(E),  $\Phi(\vec{r}, E)$  and  $\vec{J}(\vec{r}, E)$  are the diffusion constant, flux and vector current density, respectively. The time-independent transport equation (steady state) is valid in the presence of  $\mu$ t atom in the H/T layer. Hence:

$$\frac{\partial q(\vec{r},u)}{\partial u} + \Sigma_a(u)\Phi(\vec{r},u) - D(u)\nabla^2\Phi(\vec{r},u) = S(\vec{r},u)$$
(18)

where  $q(\vec{r}.u)$  represents the slowing down density of  $\mu t$  atom in the H/T layer and u is lethargy. According to the definition, we have:

$$u = lu \frac{E_1}{E_2} \tag{19}$$

where  $E_1$  and  $E_2$  are the kinetic energy of the  $\mu t$  atom before and after collision with hydrogen media in the lab. system, respectively.

Since in the H/T layer, the elastic scattering cross-section is larger than the absorption cross-section, the transport equation is valid for the  $\mu$ t atom in passing through the H/T layer. According to Eqs. (2) and (5), the absorption cross-section of the  $\mu$ t atom with protium and tritium can be written as:

$$\Sigma_a(E) = \sqrt{\frac{m_{\mu t}}{2}} \frac{N_t \lambda_{\mu t t} + N_p \lambda_{\mu p t}}{\rho} E_2^{-1/2}$$
 (20)

The absorption cross-section is dependent on  $E_2^{-1/2}$ . Hence, we have a suitable solution for the transport equation.

The slowing down density,  $q(\vec{r}.u)$ , is equal to the resonance escape probability of muonic molecular  $\mu$ tt and  $\mu$ pt formations (P(u)), at lethargy u. Therefore, the number of  $\mu$ t atoms that are absorbed in one cubic centimeter per second to produce  $\mu$ pt and  $\mu$ tt muonic molecules during slowing down to lethargy u is (1-P(u)). For the collision density,  $\psi$ (u), we have[11,12]:

$$\Psi(u) = \frac{P(u)}{\xi} = \frac{1 - (1 - P(u))}{\xi} = \frac{1}{\xi} - \frac{1 - P(u)}{\xi}$$
(21)

In Eq. 21, the first term describes the collision density for unit power source in non-absorbing media, while the second term is for negative source whit ((1-P(u))) power source, respectively.

In order to calculate P(u), the collision density is written as:

$$\Psi(u) = \frac{1}{\xi} + \int_0^u \frac{dP}{du'} \Psi(u') du'$$
 (22)

$$\Psi(u) = \int_{u}^{u+ln_{\alpha}^{\frac{1}{\alpha}}} \frac{\Sigma_{s}(u')}{\Sigma_{a}(u')+\Sigma_{s}(u')} \Psi(u') \frac{e^{-(u'-u)}}{1-\alpha} du' \quad (23)$$

$$q(u) = \int_{u}^{u+ln^{\frac{1}{\alpha}}} \frac{\Sigma_{s}(u')}{\Sigma_{a}(u') + \Sigma_{s}(u')} \Psi(u') \frac{e^{-(u'-u)} - \alpha}{1 - \alpha} du'$$
(24)

$$\frac{dq(u)}{du} = -\frac{\Sigma_a(u)}{\Sigma_a(u) + \Sigma_s(u)} \Psi(u)$$
 (25)

The differential integral for the formation of muonic molecules of  $\mu$ pt and  $\mu$ tt, P(u), can be calculated from Eqs. (21) and (23) as follows:

$$\frac{dP(u)}{du} = -\frac{\Sigma_a(u)}{\gamma \Sigma_a(u) + \xi \Sigma_s(u)} P(u)$$

Transport Theory of Muonic Atoms in Hydrogen Isotope Media

$$P(u) = \exp\left(-\int_0^u \frac{\Sigma_a(u')}{\gamma \Sigma_a(u') + \xi \Sigma_s(u')} du'\right)$$
$$= \exp\left(-\int_E^{E_1} \frac{\Sigma_a(E')}{\gamma \Sigma_a(E') + \xi \Sigma_s(E')} \frac{dE'}{E'}\right) (26)$$

where  $\gamma = 1 - \frac{\alpha \ln^2(\frac{1}{\alpha})}{2(1-\alpha)\xi}$ . Using Fig. 2, the elastic scattering cross-section in the region of various energies can be written as follows:

$$\Sigma_{s1}(E) = N_P \sigma_{s1}(E) = 34.2E - 200.53$$

$$10 \ eV \le E \le 45 \ eV \tag{27}$$

$$\Sigma_{s2}(E) = N_P \sigma_{s2}(E) = -616E - 862.5$$

$$0.5 \ eV \le E \le 10 \ eV$$
(28)

With the use of the previously defined  $\Sigma_S$  and  $\Sigma_a$ , we have:

$$P(u) = \exp(-\Upsilon) \tag{29}$$

where

$$\Upsilon = -\int_{E}^{45} \frac{\Sigma_{a}(E')}{\gamma \Sigma_{a}(E') + \xi \Sigma_{s}(E')} \frac{dE'}{E'}$$
 (30)

٥r

$$\Upsilon = -\int_{E}^{10} \frac{\Sigma_{a}(E')}{\gamma \Sigma_{a}(E') + \xi \Sigma_{s}(E')} \frac{dE'}{E'} - \int_{10}^{45} \frac{\Sigma_{a}(E')}{\gamma \Sigma_{a}(E') + \xi \Sigma_{s}(E')} \frac{dE'}{E'} \tag{31}$$

In order to find the dependence of the output energy of  $\mu t$  atom on the thickness of the H/T layer, Eqs. (16) and (18) are used and the mean square of the slowing down length,  $\overline{r_E^2}$ , is calculated [10].

The root-mean-square of the slowing down length,  $\sqrt{\overline{r_E^2}}$ , is the average distance in which the  $\mu t$  atom with 45 eV kinetic energy slows down to the energy of about 10 eV in the H/T layer.  $\overline{r_E^2}$  is defined by:

$$\overline{r_E^2} = \frac{\int r^2 \Phi(\vec{r}, E) \, d^3 r}{\int \Phi(\vec{r}, E) \, d^3 r}$$
 (32)

Using Eq. (18), we can write:

$$\frac{\partial q(\vec{r},u)}{\partial u} = \xi \Sigma_s(u) \Phi(\vec{r},u) - q(\vec{r},u)$$
 (33)

and

$$\Phi(\vec{r}, u) = \frac{1}{\xi \Sigma_c} \left[ \frac{\partial q(\vec{r}, u)}{\partial u} + q(\vec{r}, u) \right]$$
(34)

Substituting Eqs. (33) and (34) in Eq. (18), we have:

$$\frac{\partial q(\vec{r},u)}{\partial u} \left( 1 + \frac{\gamma \Sigma_a(u)}{\xi \Sigma_s(u)} \right) + \frac{\gamma \Sigma_a(u)}{\xi \Sigma_s(u)} q(\vec{r},u) - \frac{D(u)}{\xi \Sigma_s(u)} \nabla^2 \left( \frac{\partial q(\vec{r},u)}{\partial u} + q(\vec{r},u) \right) = S(\vec{r},u) \quad (35)$$

The Fourier transform of the slowing down density can be written as:

$$q(\vec{r}, u) = \frac{1}{(2\pi)^3} \int f(\omega, u) \exp(-i\omega r) d^3r$$
(36)

$$\frac{\partial q(\vec{r},u)}{\partial u} = \frac{1}{(2\pi)^3} \int \frac{\partial f(\omega,u)}{\partial u} \exp(-i\omega r) d^3 r$$
 (37)

$$S(\vec{r}, u) = S(\vec{r})S(u) = \delta(\vec{r})\delta(u)$$
 (38)

$$\delta(\vec{r}) = \frac{1}{(2\pi)^3} \int \exp(-i\omega r) \, d^3r \tag{39}$$

$$\nabla^2 q(\vec{r}, u) = \frac{1}{(2\pi)^3} \int (-\omega^2) f(\omega, u) \exp(-i\omega r) d^3 r \quad (40)$$

Substituting Eqs.(36)-(39) in Eq. (35), we get:

$$\frac{\partial f(\omega, u)}{\partial u} \left[ \left( \frac{\xi \Sigma_{S}(u) + \gamma \Sigma_{a}(u)}{\xi \Sigma_{S}(u)} \right) + \frac{D(u)\omega^{2}}{\xi \Sigma_{S}(u)} \right] + f(\omega, u) \left[ \frac{\gamma \Sigma_{a}(u) + D(u)\omega^{2}}{\xi \Sigma_{S}(u)} \right] = \delta(u)$$
(41)

then:

$$f(\omega, u) = f(\omega, u = 0) \exp\left(-\int \frac{\gamma \Sigma_a(u) + D(u)\omega^2}{\xi \Sigma_s(u) + \gamma \Sigma_a(u) + \omega^2 D(u)} du\right)$$
(42)

$$f(\omega, u = 0) = \left[\frac{\gamma \Sigma_a(u) + \gamma \Sigma_a(u)}{\xi \Sigma_s(u) + \gamma \Sigma_a(u) + \omega^2 D(u)}\right]_{u=0}$$
(43)

By expanding  $f(\omega, u)$  in terms of  $\omega^2$ , we derive  $\overline{r_E^2}$  for the  $\mu t$  atom in the H/T layer. Thus we have:

$$f(\omega, u) = \sum_{s=0}^{\infty} \frac{(-1)^s}{(2s+1)!} r_E^{2s} \omega^{2s} = 1 - \frac{1}{6} r_E^2 \omega^2 + \frac{1}{120} r_E^4 \omega^4 - \cdots$$
 (44)

$$\frac{1}{6}\overline{r_E^2} = -\left(\frac{\partial f(\omega, u)}{\partial \omega^2}\right)_{\omega=0} \tag{45}$$

Differentiating Eq. (44) with respect to  $\omega^2$ , we obtain:

Article 
$$\frac{1}{6} \overline{r_E^2} = \frac{1}{3(\gamma \Sigma_a(E_1) + \xi \Sigma_s(E_1))^2} + \int_E^{45} \frac{\xi \Sigma_s(E')}{(\gamma \Sigma_a(E') + \xi \Sigma_s(E'))^3} \frac{dE'}{E'} \times \exp{-E} > 1045 \quad \Sigma aE' \gamma \Sigma aE' + \xi \Sigma s1E' dE'E' - E < 1010 \quad \Sigma aE' \gamma \Sigma s2E' dE'E'$$
(46)

where  $\gamma$  and  $\xi$  parameters are constant. Knowing the energy variation of  $\Sigma_a$  and  $\Sigma_s$ , the integral of

Eq.(46) is determined. Hence, the effective thickness of the layer becomes:

$$x_{rms} = \sqrt{\overline{x_E^2}} = \sqrt{\overline{r_E^2}} \ \overline{\cos \theta} \tag{47}$$

The calculated values of effective thickness of the H/T layer,  $x_{rms}$ , versus the laboratory kinetic energy of  $\mu t$  are shown in Fig. 3. The only experimental value shown in Fig. 3 is in good agreement with the calculated values.

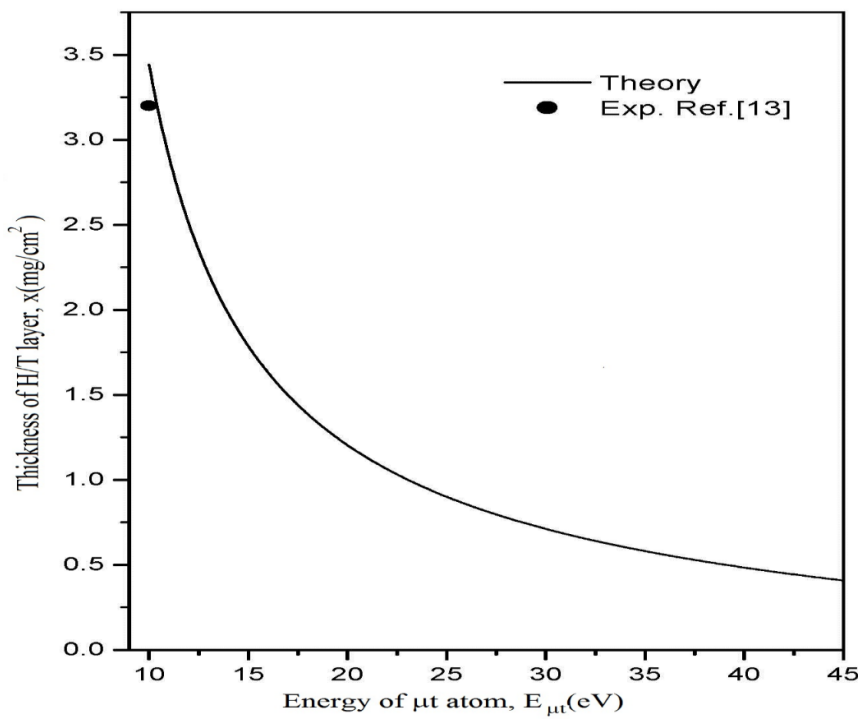


FIG. 3. Thickness of H/T layer for various output energies of µt atom in lab. system.

# Energy Loss of µt Atoms in D2 Layer

The transport conditions of  $\mu t$  atom in the first  $D_2$  layer will be studied in the second stage and the mean-square-length in which the muonic atom slows down from 10 eV to 0.5 eV can be calculated by transport theory. Consequently, the optimum thickness of the first  $D_2$  layer will be determined for the resonance formation of the muonic molecule.

The non-resonance formation rate of muonic molecule  $\mu$ dt is much smaller than the resonance molecular formation rate. Hence, in this calculation, the non-resonance molecular formation rates are ignored. The first layer of  $D_2$  acts as a moderator and the mean kinetic energy of the  $\mu$  atom arriving at the second  $D_2$ 

layer depends on the thickness of the first  $D_2$  layer. The angular scattering distribution of the  $\mu t$  atoms after collision in the lab. system is determined by Eq. (12) as;  $\cos \theta = 0.322$ . The kinetic energy of the  $\mu t$  atom per collision can be calculated by Eq. (13) as;  $\overline{E_2} = 0.661E_1$ . Also, the average reduced logarithmic energy,  $\xi$ , and  $\gamma$  in the  $D_2$  layer are 0.754 and 0.8636, respectively. Since the  $\mu t$  atoms collide only elastically with the  $D_2$  molecules, then  $\Sigma_a \approx 0$ , therefore, we write the transport equation as:

$$\frac{\partial q(\vec{r},u)}{\partial u} - \frac{D(u)}{\xi \Sigma_S(u)} \nabla^2 \left( \frac{\partial q(\vec{r},u)}{\partial u} \right) = S(\vec{r},u)$$
 (48)

The elastic scattering cross-section of  $\mu t$  atom with the  $D_2$  molecules in the energy region 0.5 eV - 10 eV is almost constant ( $\Sigma_s$ =0.1 cm<sup>-1</sup>) [5, 12].

Using Fourier transform, slowing down density is calculated and the mean-square-length of slowing down from 10 eV to 0.5 eV is calculated by:

$$\frac{1}{6}\overline{r_E^2} = -\left(\frac{\partial f(\omega, u)}{\partial \omega^2}\right)_{\omega=0} = \frac{1}{\xi_S \Sigma_S^2} \ln \frac{10}{E}$$
 (49)

and

$$r_{rms} = \sqrt{\overline{r_E^2}} = \sqrt{\frac{2}{\xi_S \Sigma_S^2}} \ln \frac{10}{E}$$
 (50)

$$x_{rms} = r_{rms} \ \overline{\cos \theta} = 0.33 \sqrt{\frac{2}{\xi_s \Sigma_s^2} \ln \frac{10}{E}}$$
 (51)

The calculated theoretical values of the mean kinetic energy of ut atoms in the lab. system arriving at the various thicknesses of the first D<sub>2</sub> layer are shown in Fig. 4 and are compared with the available experimental values. It is shown that the transport theory is an acceptable method for studying the transport theory of muonic atoms in hydrogen isotope media in low energy limit. It seems that the difference between the theoretical and the experimental data, in high energy limit, is due to consideration of the approximate method cross-section for calculation.

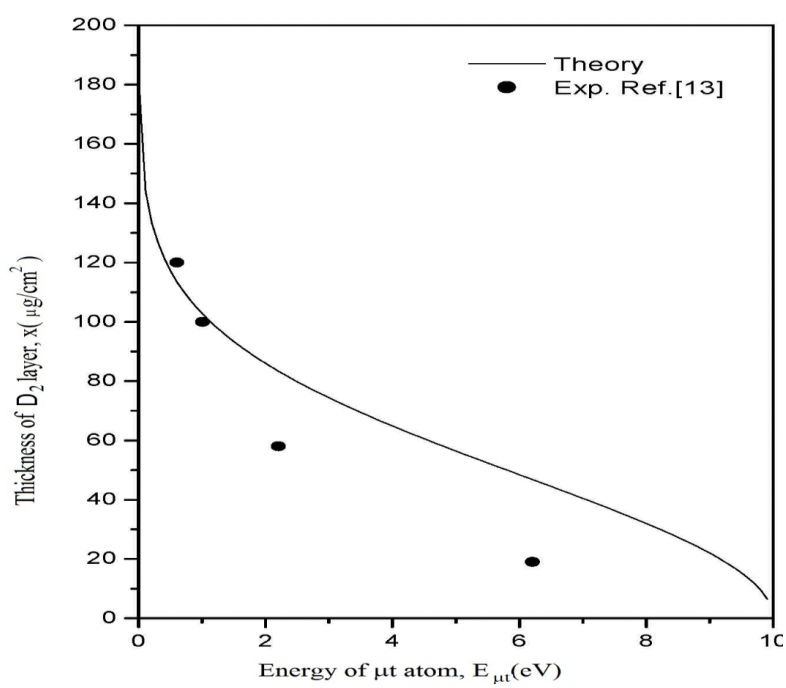


FIG. 4. Dependence of the thickness of D<sub>2</sub> layer on the output energy of μt atom in Lab. system.

# **Results of Calculations and Discussion**

The results of this study using the transport theory and available experimental values are shown in Figs. 3 and 4. The comparison shows an acceptable agreement between our method and available experimental values at low energies (E < 1 eV). For high energies (E > 1 eV), there are discrepancies which may occur due to the limitations of the media. These limitations include; non-resonance formation rate, absorption cross-section for H/T layer, motion of the target nucleus and energy dependence of elastic scattering cross-section for the first  $D_2$  layer, which is ignored. If the

thicknesses of H/T and  $D_2$  layers are selected to be  $\sim 3.2~\text{mg/cm}^2$  and  $0.1~\text{mg/cm}^2$  for the suggested system (heterogeneous solid H/D/T mixture), respectively, the  $\mu$ dt molecule formation in the second  $D_2$  layer (reaction layer) is in resonance. This study shows that the theoretical method is good and acceptable for the use of transport theory of muonic atoms in hydrogen isotope media.

# Acknowledgment

This work has been financially supported by the Research Council, University of Mazandaran, Iran. Article Mahdavi

# References

- [1] Markushin, V.E., Phys. Rev. A, 50 (1994) 1137.
- [2] Froelich, P., Adv. Phys., 41 (1992) 405.
- [3] Udovicic, V. et al., J. Fusion Energy, 30 (2011) 487.
- [4] Mulhauser, F. et al., Hyp. Int., 138 (2001) 41.
- [5] Lauss, B. et al., Phys. Rev. Lett., 76 (1996) 4693.
- [6] Marshall, G.M. et al., Hyp. Int., 108/109 (1998) 1.
- [7] Eskandari, M.R., Mahdavi, M. and Rezaie, L., IJMPE, 14 (2005) 1033.

- [8] Porcelli, T.A. et al., Phys. Rev. Lett., 86 (2001) 3763.
- [9] Mahdavi, M. and Zanganeh, V., Chin. J. Phys., 46 (2008) 278.
- [10] Kiyani, A. et al., J. Fusion Energy, 30 (2011) 473.
- [11] Tizaoui, A., J. Fusion Energy, 28 (2009) 342.
- [12] Eskandari, M.R. and Shirazi, K.R., Int. J. Mod. Phys. C, 14 (2003) 367.
- [13] Fujiwara, M.C. et al., arXiv: nucl-ex/0101007v1 22 Jan (2001).

# Jordan Journal of Physics

# **ARTICLE**

# <sup>226</sup>Ra, <sup>228</sup>Ra and <sup>40</sup>K Concentrations in Some Plant Seeds Consumed in Jordan

# Khaled A. Al-Khaza'leh

Department of Physics, Al-albayt University, P.O.BOX 130040, Mafraq 25113, Jordan.

Received on: 10/4/2017; Accepted on: 14/9/2017

**Abstract:** Eleven types of seeds consumed by Jordanian people were investigated to determine the concentration levels of  $^{226}$ Ra,  $^{228}$ Ra and  $^{40}$ K radionuclides. The calculated concentration ranges from  $0.214 \pm 0.017$  to  $7.583 \pm 0.592$   $Bq/kg_{dry}$ ,  $10.629 \pm 0.914$   $Bq/kg_{dry}$  and  $92.0 \pm 7.61$  to  $576 \pm 46.22$   $Bq/kg_{dry}$  for  $^{226}$ Ra,  $^{228}$ Ra and  $^{40}$ K, respectively. The total annual effective dose that resulted from consuming the selected seeds by ingestion was 35.17  $\mu Sv/year$ , whereas the cancer risk ranges between  $1.58 \times 10^{-6}$  from fennel and  $23.53 \times 10^{-6}$  due to beans. However, the average cancer risk value was  $7.74 \times 10^{-6}$ , which is less than the world average cancer risk value 3mSv/year.

Keywords: Radionuclides, Concentration, Annual effective dose, Cancer risk.

# Introduction

Radium belongs to the primordial radionuclide group, as it always has natural radionuclides. In addition, the radionuclides <sup>228</sup>Ra and <sup>226</sup>Ra decay through two distinct series of radionuclides (Thorium and Uranium natural series, respectively). Besides, the natural decay series of <sup>40</sup>K contributes with a lot of irradiation to the human body.

Compared to <sup>226</sup>Ra which is an alpha emitter, <sup>228</sup>Ra is rather a weak β-emitter ( $E_{max}$ = 39.0 keV [60%] and 14.5 keV [40%]). Both alpha and beta emitters cannot penetrate the dead skin layer of the body to ionize the live cells. About 90% of radium enters the human body through food under normal environmental conditions [1]. Furthermore, plant contamination could be either directly correlated to the deposition of radioactive materials from the atmosphere [2, 3] or indirectly correlated to the absorption of radionuclides from soil by roots which are eventually transported to other parts of the plant [4]. The presence of radionuclides in edible parts of crops causes human internal exposure [5, 6]. Moreover, both types of radium (226Ra and 228Ra) were known as the most radiotoxic elements [7]. In addition, the high biological half life leads to

long time internal irradiation exposure. However, <sup>40</sup>K is radiotoxic, yet naturally important [7].

In this study, we will determine the natural radionuclide (<sup>226</sup>Ra, <sup>228</sup>Ra and <sup>40</sup>K) concentrations in some plant seeds consumed by Jordanian people.

# **Materials and Methods**

Eleven types of plant seeds used very often in Jordanian food were purchased from a local market in Ramtha city. These seeds are: black pepper, black cumin, cumin, anise, coriander, fenugreek, fennel, chickpeas, beans, peas and corn. Each of these samples weight was 250g.

# **Sample Preparation**

The pre-treated samples were made according to the recommendations given by International Atomic Energy Agency [8]. First of all, the samples were dried overnight at 105°C to reach a constant weight. All the dried samples were grounded into fine powder. Next, each sample was saved in a 90 ml capacity beaker. After that, all the samples were left for about 28 days to

Corresponding Author: Khaled A. Al-Khaza'leh Email: khazalih@aabu.edu.jo

Article Khaled A. Al-Khaza'leh

allow reaching secular equilibrium of <sup>226</sup>Ra and <sup>228</sup>Ra and their daughters [14].

Furthermore, radioactivity was determined in the Gamma Spectroscopy Laboratory in Jordan Commission Atomic Energy (JAEC). Radionuclides were analyzed by gamma spectroscopy with a high-purity germanium detector (HPGe) connected to a multi-channel analyzer (MCA) of Genie-2000 software. The relative efficiency of this detector is about 50% with a resolution of 2.0 keV. The activity concentration of <sup>226</sup>Ra was determined through its daughter products <sup>214</sup>Pb (295.2 keV and 351.9 keV) and <sup>214</sup>Bi (609.3 keV). Besides, the activity of <sup>228</sup>Ra was determined through its daughters <sup>212</sup>Pb (238.6 keV) and <sup>228</sup>Ac (911.2 keV and 969 keV). However, the 40K activity can be determined by its own gamma peak of 1461 keV.

# **Theoretical Calculations**

# **Annual Effective Dose**

The annual effective dose due to ingestion occurring through contaminated food by radionuclides can be calculated using Eq. (1) [9]:

$$AD = \mu CA \tag{1}$$

where (AD) is the annual effective dose (Sv/year),  $\mu$  is the dose coefficient (Sv/Bq), C is the concentration of the radionuclide in the sample (Bq/kg) and A is the annual consumption (kg/year). The dose coefficients were  $2.8\times10^{-7}$  Sv/Bq for  $^{226}$ Ra,  $6.7\times10^{-7}$  Sv/Bq for  $^{228}$ Ra and  $6.2\times10^{-9}$  Sv/Bq for  $^{40}$ K [2].

# **Excess Lifetime Cancer Risk**

Excess lifetime cancer risk due to exposure through ingestion was calculated using Equation (2) [10-12].

$$Rc = Cd \times RF (Sv^{-1}) \tag{2}$$

where RF is the risk factor (0.05) as (ICRP 1990) and Cd is the lifetime of the effective dose. The lifetime of the effective dose is a measure of the total effective dose received over

an average lifetime of 50 years following ingestion of a radionuclide and was calculated using UNSCEAR 2000 [13]:

$$Cd = 50 \times D \tag{3}$$

where D is the total effective dose to an individual.

# **Results and Discussion**

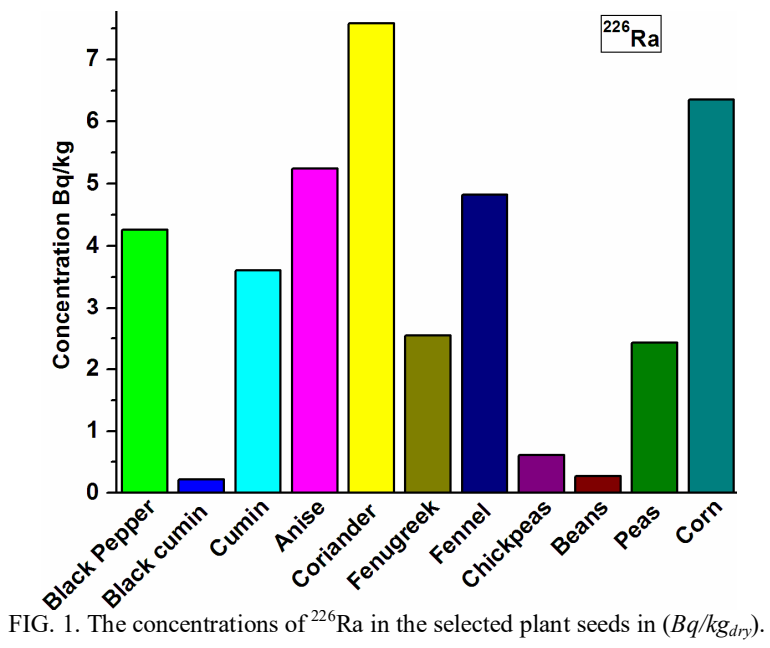
Table (1), presented in concentrations range from 0.214±0.017 Bq/kg in black cumin and 7.583  $\pm$  0.592 Bq/kg in coriander. Additionally, <sup>228</sup>Ra concentrations were not detectable in beans and chickpeas. However, the <sup>228</sup>Ra concentration for black pepper was found  $10.629 \pm 0.914$  Bg/kg. Finally, the  $^{40}$ K concentrations were found 92  $\pm$  7.612 Bq/kg and 576  $\pm$  46.22 Bq/kg for both black pepper and fennel, respectively. From the above, clearly 40K has the highest concentration in all samples (refer to Table 1). This could be correlated to the high concentration of potassium in soil, where plants absorb it in different amounts [14].

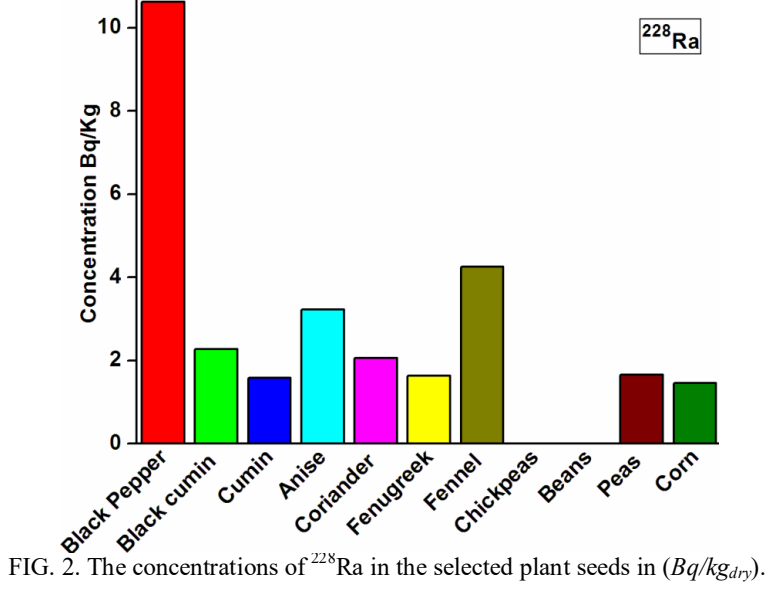
From Fig. 1, coriander has the maximum concentration of <sup>226</sup>Ra followed by corn, anise and fennel. The concentrations of <sup>226</sup>Ra in beans, black cumin and chickpeas are much less than in other seeds. On one hand, the maximum concentration of <sup>228</sup>Ra in black pepper is far less than in other seeds and not detectable in both beans and chickpeas (refer to Fig. 2). Fennel has the maximum concentration of <sup>40</sup>K followed by cumin, then by beans, anise and coriander with black pepper having the minimum concentration of <sup>40</sup>K, (refer to Fig. 3).

Fig. 4 shows a comparison between <sup>226</sup>Ra and <sup>228</sup>Ra concentrations in all seeds under study. As we can see from Fig. 4, <sup>226</sup>Ra concentrations are greater than <sup>228</sup>Ra concentrations in all samples under investigation with the exceptions in black pepper and black cumin.

TABLE 1. The concentrations of  $^{226}$ Ra,  $^{228}$ Ra and  $^{40}$ K in selected plant seeds in  $Bq/kg_{div}$ .

ilectifi at lons of		ix in sciected plant	seeds in by ng
Plant seed	<sup>226</sup> Ra	<sup>228</sup> Ra	$^{40}\mathrm{K}$
Black Pepper	4.257±0.331	10.629±0.914	92.0±7.61
Black cumin	$0.214 \pm 0.017$	$2.271\pm0.212$	$336\pm27.03$
Cumin	$3.610\pm0.294$	$1.583 \pm 0.130$	$550\pm43.92$
Anise	$5.247 \pm 0.418$	$3.220\pm0.263$	$468 \pm 37.65$
Coriander	$7.583 \pm 0.592$	$2.061\pm0.158$	$448 \pm 36.41$
Fenugreek	$2.543 \pm 0.224$	$1.629\pm0.135$	$297\pm22.94$
Fennel	$4.821 \pm 0.378$	$4.254\pm0.361$	$576\pm46.22$
Chickpeas	$0.615 \pm 0.055$	Not detectable	$320\pm26.31$
Beans	$0.273 \pm 0.023$	Not detectable	$462 \pm 36.61$
Peas	$2.425 \pm 0.220$	$1.665 \pm 0.141$	$261\pm20.41$
Corn	$6.352\pm0.493$	$1.462\pm0.120$	191±15.47





Article Khaled A. Al-Khaza'leh

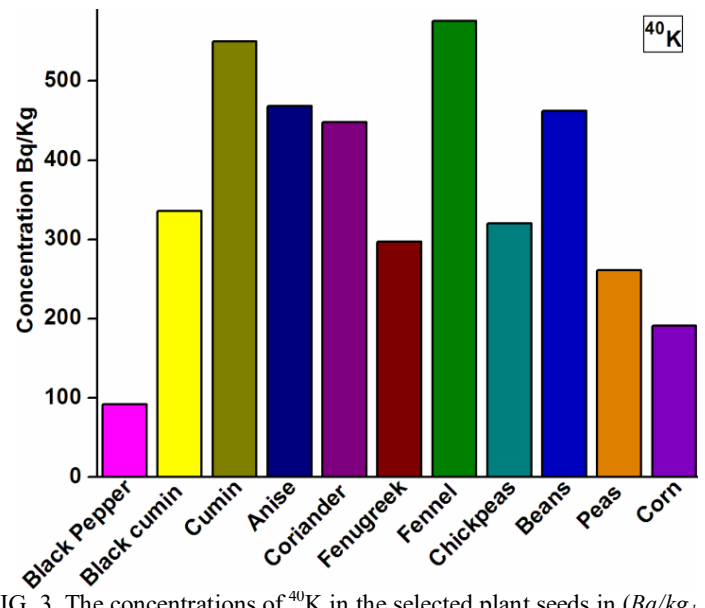


FIG. 3. The concentrations of  $^{40}$ K in the selected plant seeds in  $(Bq/kg_{dry})$ .

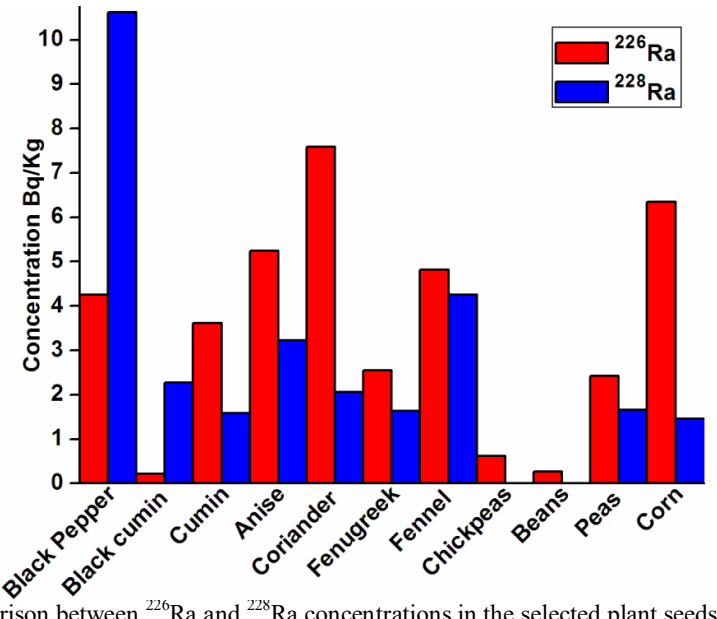


FIG. 4. Comparison between  $^{226}$ Ra and  $^{228}$ Ra concentrations in the selected plant seeds in  $(Bq/kg_{dry})$ .

It is worth to mention that the present results are comparable with other local and international results. A study in Saudi Arabia reported that the concentrations of <sup>226</sup>Ra in black pepper, black cumin, anise, coriander and fennel were 21.71, 5.9, 38.2, 69 and 16.5  $Bq/kg_{dry}$  respectively [12]. For comparison, the concentrations of <sup>226</sup>Ra in the present study were 4.3, 0.21, 5.2, 7.5 and 4.8  $Bq/kg_{dry}$  for black pepper, black cumin, anise, coriander and fennel, respectively. It can be seen that all concentrations in the present study were less than those in Saudi Arabia. However, in Pakistan, for instance, the concentration of <sup>226</sup>Ra in black pepper and peas was 1.2 Bq/kg<sub>dry</sub> [15], which means less than in our study.

Furthermore, Spain [16],in concentrations of <sup>226</sup>Ra in such seeds were comparable with those in our study, except in coriander which was higher in our study. Moreover, in Tanzania, the concentrations of <sup>226</sup>Ra in beans and corn were 21 and 25.6 Bq/kg [17] and 34 Bq/kg for corn in Nigeria [18], while in Iraq, the <sup>226</sup>Ra concentration was 0.41 Bq/kg in corn [19]. In the present study, the concentrations of <sup>226</sup>Ra were much less than those in Tanzania and Nigeria, yet, they are comparable with the results in Iraq. Additionally,

the concentrations of  $^{228}$ Ra in coriander, chickpeas and beans were < 0.11 Bq/kg, < 0.39 Bq/kg and < 0.34 Bq/kg, respectively in Spain [16], which are close to our results for both chickpeas and beans, yet  $^{228}$ Ra was not detectable in both chickpeas and beans. However, in our study, higher concentrations of  $^{228}$ Ra in coriander were present.

As a final comparison, the concentrations of  $^{40}$ K in Saudi Arabia, as Al-Ghamdi reported, were 446, 1039, 589, 964 and 786 *Bq/kg* for black pepper, black cumin, coriander, anise and fennel, respectively [12]. On the other hand, our investigations reveal lower  $^{40}$ K concentrations for the same seeds, respectively (refer to Table

1). Moreover, in Egypt,  $^{40}$ K concentrations were 507, 900, 611 and 596 Bq/kg in black pepper, cumin, coriander and beans, respectively, which are greater than the concentrations of  $^{40}$ K in our study [20]. In a Nigerian study, Jibiri and others reported that the concentrations of  $^{40}$ K in beans and corn were 453 and 243 Bq/kg, respectively compared with the concentrations of  $^{40}$ K in beans and corn in the present study [18]. In Spain,  $^{40}$ K concentrations were 380 and 370 Bq/kg in chickpeas and corn, respectively [16], while those concentrations were 130 and 419 Bq/kg for black cumin and chickpeas in Iraq [19]. Both annual effective dose and cancer risk were calculated and presented in Table 2.

TABLE 2. Annual effective doses in  $\mu Sv/year$  and cancer risk values for  $^{226}Ra$ ,  $^{228}Ra$  and  $^{40}K$  radionuclides.

Generally	Annual consumption	Annual effective dose			Total annual	Cancer risk
Plant seed	kg/y	<sup>226</sup> Ra	<sup>228</sup> Ra	$^{40}$ K	effective dose	μSv/year
Black Pepper	0.14	0.17	1	0.08	1.25	3.13
Black cumin	0.23	0.01	0.35	0.48	0.84	2.1
Cumin	0.18	0.18	0.19	0.61	0.98	2.45
Anise	0.22	0.32	0.47	0.64	1.43	3.58
Coriander	0.37	0.79	0.51	1.03	2.33	5.83
Fenugreek	0.42	0.3	0.46	0.77	1.53	3.83
Fennel	0.15	0.2	0.43	1.11	1.74	1.58
Chickpeas	3.5	0.24	0	0.53	0.77	1.93
Beans	3.2	0.24	0	9.17	9.41	23.53
Peas	2.4	1.63	2.68	3.88	8.19	20.48
Corn	1.7	3.02	1.67	2.01	6.7	16.75
Total	12.51	7.10	7.76	20.31	35.17	102.56

From Table 2, it can be seen that the annual effective dose for <sup>226</sup>Ra was maximum for corn (3.02 µSv/year) and minimum for black cumin  $(0.01 \ \mu Sv/year)$ . In addition, for <sup>228</sup>Ra, the maximum annual effective dose was recorded for peas with 2.68 µSv/year, followed by corn with 1.67  $\mu Sv/year$ , while <sup>228</sup>Ra was not detected in both beans and chickpeas. Finally, the maximum annual effective dose of 40K was recorded for beans with 9.17 µSv/year, followed by peas with 3.88  $\mu Sv/vear$ . Black pepper has the minimum dose of 0.08  $\mu$ Sv/year. Apparently, the annual effective dose depends not only on the concentration of radionuclide in the individual seed (Bq/kg), but also on the annual consumption (kg/year). This can explain the variations in the above calculated annual effective doses. In general, beans have the maximum total annual effective dose of 9.41 µSv/year, followed by peas with 8.19  $\mu Sv/year$  and corn with 6.7  $\mu Sv/year$ , with the minimum dose of 0.77  $\mu Sv/year$  in chickpeas.

Clearly, about 58% of the total annual dose resulting from the studied radionuclide was for  $^{40}$ K with 20.31  $\mu$ Sv/year, while  $^{228}$ Ra and  $^{226}$ Ra are forming 22% and 20%, respectively. Additionally, the total annual effective dose for all seeds was 35.17  $\mu$ Sv/year, which is quite below the upper limit of 3 mSv as specified by ICRP recommendations [13].

Furthermore, beans have the maximum cancer risk of  $23.53 \times 10^{-6}$ , followed by peas and corn with  $20.48 \times 10^{-6}$  and  $16.75 \times 10^{-6}$ , respectively, while the cancer risk is minimum for fennel with  $1.58 \times 10^{-6}$  (refer to Table 2). In addition, the total cancer risk for seeds under study is  $102.56 \times 10^{-6}$ . However, the average risk value is  $7.74 \times 10^{-6}$ , which could be less than those reported in other studies of  $58 \times 10^{-6}$  [12]

Article Khaled A. Al-Khaza'leh

and  $48\times10^{-6}$  [10]. Compared to the world average risk of  $290\times10^{-6}$ , the present study shows a lower cancer risk.

# Conclusion

The concentrations of  $^{226}$ Ra,  $^{228}$ Ra and  $^{40}$ K in selected food seeds in Jordan were measured and compared with those reported in other international studies. The concentrations range from 0.214  $Bq/kg_{dry}$  in black cumin to 7.54  $Bq/kg_{dry}$  in coriander for  $^{226}$ Ra. While  $^{228}$ Ra concentrations were not detectable in chickpeas and beans,  $^{228}$ Ra concentration was 10.62

 $Bq/kg_{dry}$  in black pepper. Furthermore, <sup>40</sup>K concentrations in black pepper and fennel were 92  $Bq/kg_{dry}$  and 576  $Bq/kg_{dry}$ , respectively. The annual effective dose ranges from 0.77  $\mu Sv/year$  in chickpeas to 9.41  $\mu Sv/year$  in beans, which is less than the upper limit 3mSv according to ICRP [13]. On the other hand, the average cancer risk was  $7.4 \times 10^{-6}$ , which is less than the world average risk [12]. Our investigations suggest that consuming the selected seeds by Jordanian people has no significant health risk. However, other consumed foods by Jordanians require further investigations.

# References

- [1] Muth, H., Rajewsky, B., Hantke, H.J. and Aurand, K., Health Phys., 2 (1960) 239.
- [2] Monte, L. Quaggia, S. and Pompei, S., J. Environ. Radioact., 11 (1990) 207.
- [3] Badran, H.M., Sharshar, T. and Elnimer, T., J. Environ. Radioact., 67 (2003) 181.
- [4] Toba, T. and Ohta, T., J. Hydrol., 313 (2005) 208
- [5] Pulhani, V., Dafauti, S., Hegde, A., Sharma, R. and Mishra, U., J. Environ. Radioact., 79 (2005) 331.
- [6] Alsaffar, M.S., Jaafar, M.S., Kabir, N.A. and Ahmad, N., JRRAS, 8 (2015) 300.
- [7] Atwood, D.A., "Radionuclides in the Environment", (John Wiley and Sons, 2013).
- [8] International Atomic Energy Agency. "Measurement of Radionuclides in Food and the Environment", Guide Book. Technical Report Series No. 295. Vienna: IAEA; 1989.
- [9] Saeed, M.A., Wahab, N.A., Hossain, I., Ahmed, R., Abdullah, H.Y., Ramli A.T. and Bashir, A.T., J. Phys. Sci., 6(32) (2001) 7335.
- [10] Amin, R.M. and Ahmed, F., Adv. Appl. Sci. Res., 4(5) (2013) 350.
- [11] El-Taher, A. and Al-Zahrani, J.H., Indian J. Pure Appl. Phys., 52 (2014) 147.

- [12] Al-Ghamdi, A.H., J. Am. Sci., 10(11) (2014) 164.
- [13] United Nations Scientic®, "Committee on the Effects of Atomic Radiation". UNSCEAR 2000. Report to General Assembly, pp. 93-156 (NewYork: United Nations, 2000).
- [14] Al-Absi, E., Al-Abdullah, T., Shehadeh, H. and Al Jundi, J., Radiat. Prot. Environ., 38 (2015) 29.
- [15] Khan, K., Akhter, P., Orfi, S.D. and Khan, H.M., Intern. Conf. on Isotopic and Nuclear Analytical Techniques for Health and Environment, Vienna, Austria (2003).
- [16] Hernandez, F., Hernandez-Armas, J., Catalan, A., Fernandez-Aldecoa, J.C. and Landeras, M.I., Radiat. Prot. Dosim., 111(2) (2004) 205.
- [17] Nkuba, L.L. and Mohammed, N.K., J. Sci., 40 (2014) 51.
- [18] Jibiri, N.N., Farai, I.P. and Alausa, S.K., Radiat. Environ. Biophys., 46 (2007) 53.
- [19] Ahmed, A.H. and Samad, A.I., JZS- A, 16 (4) (2014).
- [20] Abd El-Wahab, M. and Morsy, Z.Y., Conf. on Radiation Physics & Protection, Beni Sueif-Fayoum, Egypt (2006).

# Jordan Journal of Physics

# **ARTICLE**

# Growth Inhibition of Natural Foods on Calcium Hydrogen Phosphate Dihydrate Crystals\*

# G. Anushya and T.H. Freeda

Physics Research Centre, S.T. Hindu College, Nagercoil -629002. Tamilnadu, India.

Affiliated to Manonmaniam Sundaranar University, Abishekapatti, Tirunelveli-627012, Tamilnadu, India.

**Abstract:** A large number of people are suffering from health problems due to urinary stones. The prevalence of urinary stones is increasing and approximately 12,000 patients are admitted in hospitals every year due to this condition. Brushite [CaHPO<sub>4</sub>·2H<sub>2</sub>O] or calcium hydrogen phosphate dihydrate (CHPD), which is known as urinary crystal, is a stable form of calcium phosphate. This study aims to investigate the influence of natural foods on the formation of calcium hydrogen phosphate (CHPD) crystals to elucidate the inhibitory effect of urinary stone formation from a different perspective. Natural foods used in this study are Solanum lycopersicum (Tomato), Daucus carota (Carrot) and Vitis vinifera (Grapes). Tomato is the edible fruit of Solanum lycopersicum, which belongs to the nightshade family, Solanaceae. Grapes are a fruit, botanically a berry, of the deciduous woody vines of the flowering plant genus vitis. The carrot is a biennial plant in the umbellifer family Apiaceae. The effects of natural foods, the invitro crystallization and growth inhibition of calcium hydrogen phosphate dihydrate crystals are studied using single diffusion gel growth technique. The grown crystals were characterized by total mass determination, X-ray diffraction, UV-Vis and Dielectric studies. The crystalline size is reduced for natural foods added CHPD crystals compared with pure CHPD. The grown crystals are more transparent and of a size of around 53 and 49 nm. Some variations in dielectric properties are observed due to the addition of fruit extracts.

Keywords: Natural foods, Growth inhibition, CHPD crystals.

# Introduction

Many people suffer from problems resulting from urinary stones. The presence of amorphous calcium phosphate is a common finding in urinary sediments and it is the most commonly encountered crystal material in urine [1-2]. The disease frequency is on the rise due to life style and dietary habits [3-4]. Calcium-containing stones are the most common variety of urinary stones, comprising about 75% of all urinary calculi, which are found in the form of pure calcium oxalate (50%), calcium phosphate (5%) or a mixture of both (45%). Some of the oxalates are found in

either pure or in mixed form with phosphate and reported with uric acid or ammonium urates [5-6]. Also, calcium phosphate is present in urinary calculi as either apatite [Ca<sub>10</sub> (PO<sub>4</sub>)<sub>6</sub>(OH)<sub>2</sub>] or brushite [CaHPO<sub>4</sub>.2H<sub>2</sub>O] [7-8]. Urinary stones are characterized by their high recurrence rate, if patients are not treated appropriately. Recent approaches to the treatment of urinary stones make use of Laser Lithotripsy, Percutaneous Nephrolithotomy and Extra-corporeal Shockwave Lithotripsy [9-10]. Though they provide immediate clearance of urinary stones, they cause long-term side effects [11-13]. Patients suffering from brushite

Article Anushya and Freeda

stone disease are less likely to be rendered stone free after surgical intervention; hence, a drug for the prevention of this disease or its recurrence would be of great interest.

In Ayurvedic system of medicine, Solanum lycopersicum (tomato), Daucas carota (carrot) and Vitis vinifera (grapes) were used for the treatment of various human ailments, like kidney stone, diabetes, urinary tract infection and immune system. Most of the previous papers deal with the drug therapy for the inhibition of urinary stones, but the juice therapy on the growth inhibition of these crystals was not reported. Considering the above facts, the current study is carried out to find out the inhibiting effect of fruit extracts, which are used as natural foods; viz., tomato, carrot and grapes, on brushite crystals.

The growth of crystals in a gel medium has attracted the attention of many investigators [14-16]. This is because gel method is the most versatile and simple technique for growing urinary crystals [17–19], where the gel acts as an inert and ideal medium during the growth of many crystalline compounds and *in-vitro* biomolecules [20].

$$CaCl_2.2H_2O + CaC_4H_6O_4 + H_3PO_4$$

In order to understand the inhibitory effect of natural foods on the growth of CHPD crystals, extracts of 0.5ml of tomato, 0.5ml of carrot and 0.5ml of grapes are mixed with calcium chloride and calcium acetate and the crystals are grown as before. The grown crystals are elongated, plate- like and star shaped. The crystal growth was complete in about 25 days. The grown crystals are carefully removed and collected in a clean petri dish and then harvested by removing the gel using distilled water.

Powder X-ray diffraction data is collected using an automated X-ray diffractometer with  $CuK_{\alpha}$  radiation ( $\lambda = 1.54060$  Å). The UV-visible spectrum of the sample is recorded in the wave number range of 200-600 nm using UV-Vis Double Beam Spectrophotometer 2201.

Dielectric studies are carried out with the help of Agilent 4284A LCR meter at different temperatures and at different frequencies ranging from 20 Hz to 1 MHz.

In this work, we study the inhibitory effect of natural foods on the growth of calcium hydrogen phosphate dihydrate crystals using single diffusion gel growth technique.

# Experimental

The high quality AR grade chemicals from Merck are used further without purification. Glass test tubes of 25 mm diameter and 150 mm length were used as crystal growth apparatus. Sodium meta silicate (Na<sub>2</sub>SiO<sub>3</sub> .9H<sub>2</sub>O) solution with a specific gravity of 1.03g/cc is mixed with orthophosphoric acid in an appropriate amount, so that the desired value of the pH could be set for the mixture. After setting the gel, an aqueous solution of calcium chloride and calcium acetate of a particular molarity (1M) is gently poured on the set gels in test tubes by using a pipette without damaging the gel surface. After pouring the supernatant solution, the test tubes were capped with airtight stopples. The following reaction is expected to take place, leading to the formation of calcium hydrogen phosphate dihydrate crystals:

# $\longrightarrow$ CaHPO<sub>4</sub>.2H<sub>2</sub>O + CaCO<sub>3</sub> + HCl

The dielectric constant of the crystals is calculated using the formula:

$$\epsilon_r = C_c/C_a$$

where  $C_c$  is the capacitance of the crystal and  $C_a$  is the capacitance of the air medium of the same dimension as the crystal.

The a.c. conductivity is calculated using the equation:

 $\sigma_{ac} = \varepsilon_0 \varepsilon_r \omega \tan \delta$ ,

where ' $\omega$ ' is the angular frequency and 'tan  $\delta$ ' is the loss tangent.

# **Results and Discussion**

# Growth

Calcium hydrogen phosphate dihydrate (brushite) crystals were successfully grown using the single diffusion gel growth technique. The addition of supernatant solution; namely, calcium acetate and calcium chloride over the set gel enabled the diffusion of Ca<sup>2+</sup> into the gel, which reacts with PO<sub>4</sub><sup>3+</sup>, resulting in the appearance of precipitate instantaneously at the

interface between the gel and the supernatant solution. After 4 to 5 hours just below the precipitate, circular white discs, commonly called Liesegang rings, were observed. Tiny plate- like brushite crystals started growing just

below the Liesegang rings in about 4 to 8 days and also inside the gel medium. The crystal growth was complete in about 25days. Figs. 1 and 2 show good quality star and plate- shaped crystals grown in gel media.



FIG. 1. Brushite crystals grown in gel media.



FIG. 2. Brushite + juices (0.5ml tomato + 0.5 ml carrot + 0.5 ml grapes).

The incorporation of fruit solution caused a decrease in the number of grown brushite crystals and their average size. By carefully

observing the yield of crystals per test tube, we present in Fig. 3 the promotery/inhibitory effect of the pure and the fruit extracts.

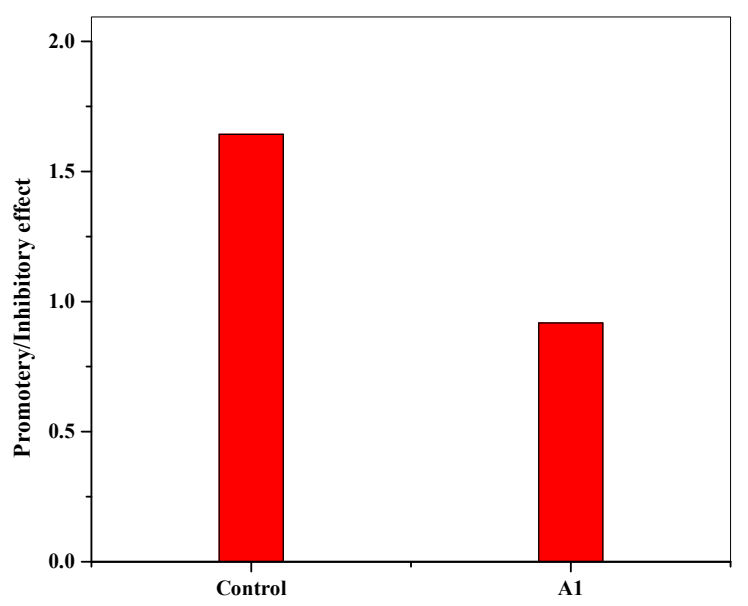


FIG. 3. Promotery/inhibitory effect of brushite crystals.

In Fig. 3 above, A<sub>1</sub> represents the fruit solution added brushite crystals.

# Powder X-ray Diffraction

The X-ray diffraction patterns of the grown crystals (shown in Figs. 1 and 2) are shown in Fig. 4 (a and b), respectively. Brushite is crystallized in the monoclinic crystal system. The crystallographic parameters are in good

agreement with the literature values (JCPDS data) [72-0713]. The highly resolved peak occurs at specific 2θ Bragg angles in the crystals, indicating the crystalline nature of the grown crystals. It is also observed that the peak values shift towards higher angles, indicating the chances of incorporation of additional ions available in the used fruit extracts within the framework of CHPD.



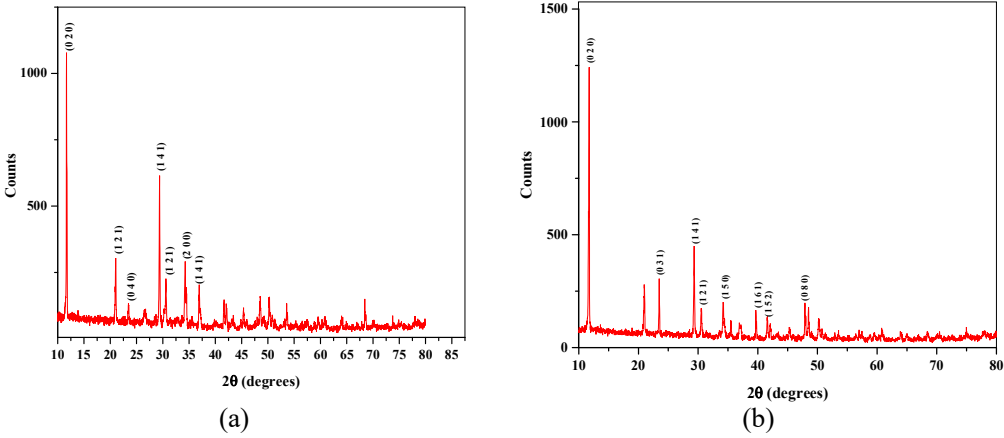


FIG. 4. PXRD patterns of (a) pure CHPD crystals; (b) fruit extracts added CHPD crystals.

TABLE 1. Lattice parameters and unit cell volume.

Complex	Unit	t cell parame	Linit cell velume V (Å)3	
Samples	A (Å)	B (Å)	C (Å)	Unit cell volume V (Å) <sup>3</sup>
Pure CHPD	5.2125	15.1781	5.605	443.444
Fruit extracts added CHPD (A <sub>1</sub> )	5.1958	15.1580	5.9963	472.177

The crystalline size of the CHPD crystals was calculated by using Scherrer equation:

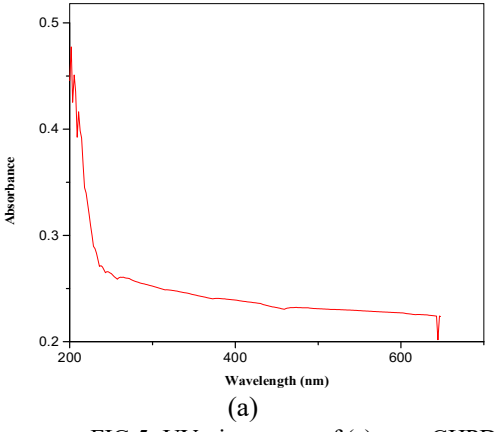
$$D = \frac{K\lambda}{\beta \cos \theta}$$

where D is the crystalline size, K is a constant usually taken as 0.89,  $\lambda$  is the wavelength of X-ray radiation,  $\beta$  is the full width at half maximum value and  $\theta$  is the Bragg diffraction angle. From the PXRD spectrum, the

crystalline size of undoped CHPD was found to be 53.72 nm, while for fruit extracts incorporated CHPD, it was found to be 49.51 nm.

# **UV-Vis Spectral Analysis**

The UV-visible absorption spectra recorded for both grown samples (Figs. 1 and 2) are shown in Fig. 5 (a and b), respectively.



1.0 0.9 (a) 0.8 0.6 0.5 0.4 200 300 400 500 600 700 800 900 Wavelength (nm) (b)

FIG 5. UV-vis spectra of (a) pure CHPD crystals; (b) fruit solution added CHPD crystals.

The UV-visible spectrum gives information about the structure of the molecules. The ultraviolet and visible light absorption involves promotion of electrons from the ground state to higher energy state. Careful analysis of the spectrum revealed no significant absorption in the entire spectrum for both pure and fruit extracts added brushite. This indicates that the

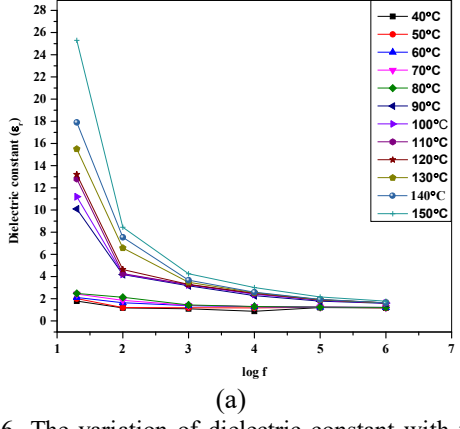
grown crystals were transparent in the entire spectral range between 370 and 600 nm. The band gap for the brushite crystals grown in the control system was found to be 5.48 eV. For the fruit extracts added brushite crystals, the band gap energy decreased to 5.38 eV.

# **Dielectric Studies**

### **Dielectric Constant**

Figs. 6 (a and b) show the variation of dielectric constant with frequency for various temperatures ranging from 40°C - 150°C for pure CHPD and fruit extracts added CHPD crystals. It is noticed that for all temperatures, the dielectric constant decreases as the frequency increases for pure CHPD crystals. Similar behaviour is observed for fruit extracts

added crystals as well. The dielectric constant of a material is usually composed of four components of polarization; namely, electronic polarization, orientation polarization, ionic polarization and space charge polarization. The electronic and ionic polarizations are independent of temperature, whereas orientation polarization and space charge polarization are temperature-dependent.



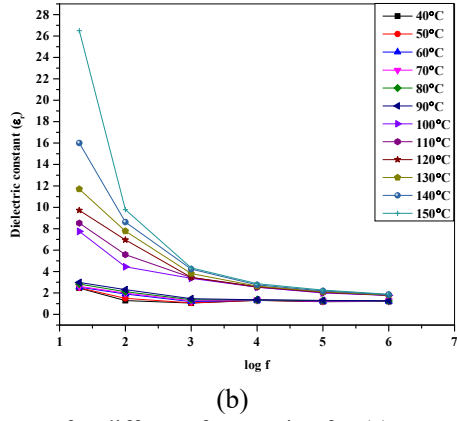
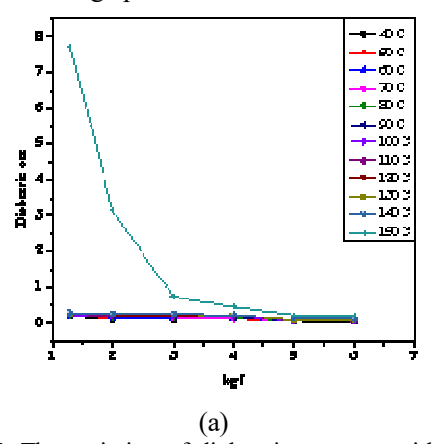


FIG. 6. The variation of dielectric constant with temperature for different frequencies for (a) pure CHPD crystals; (b) fruit extracts added CHPD crystals.

From Fig. 6 (a and b), it is clear that at low frequency (20Hz) and at low temperature (40°C), all the four types of polarization are active, but when the frequency increases, the variation of dielectric constant shows which prevailing. contribution is When temperature is above 100°C and the frequency is very low, say 20Hz, the dielectric constant is maximum. This is because of the contribution of space charge polarization. As we further increase the frequency, the dielectric constant decreases. This is because of the decrease in the space charge polarization.

# **Dielectric Loss**

The variation of dielectric loss ( $\tan \delta$ ) with frequency at different temperatures for pure CHPD and fruit extracts added CHPD is shown in Fig. 7 (a and b), respectively. The amount of energy dissipated by the material when it is subjected to external fields is called dielectric loss. It was found from Fig. 7 that the dielectric loss increases with the increasing value of applied field. The high value of dielectric loss at high frequencies indicates the low power dissipation in the crystals.



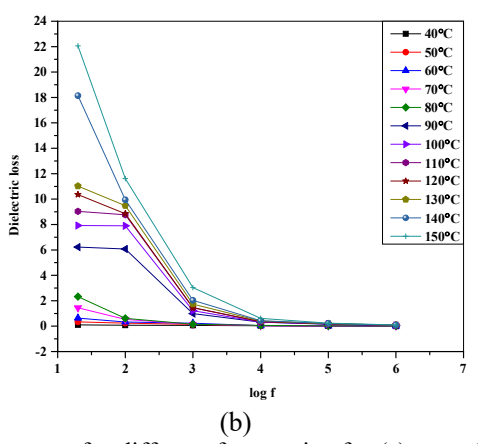


FIG. 7. The variation of dielectric constant with temperature for different frequencies for (a) pure CHPD crystals; (b) fruit extracts added CHPD crystals

Article Anushya and Freeda

# AC conductivity & Activation energy

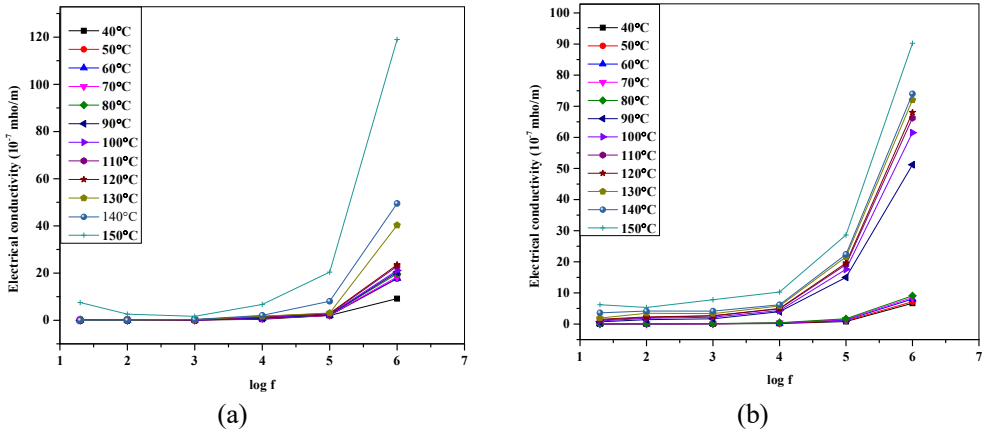
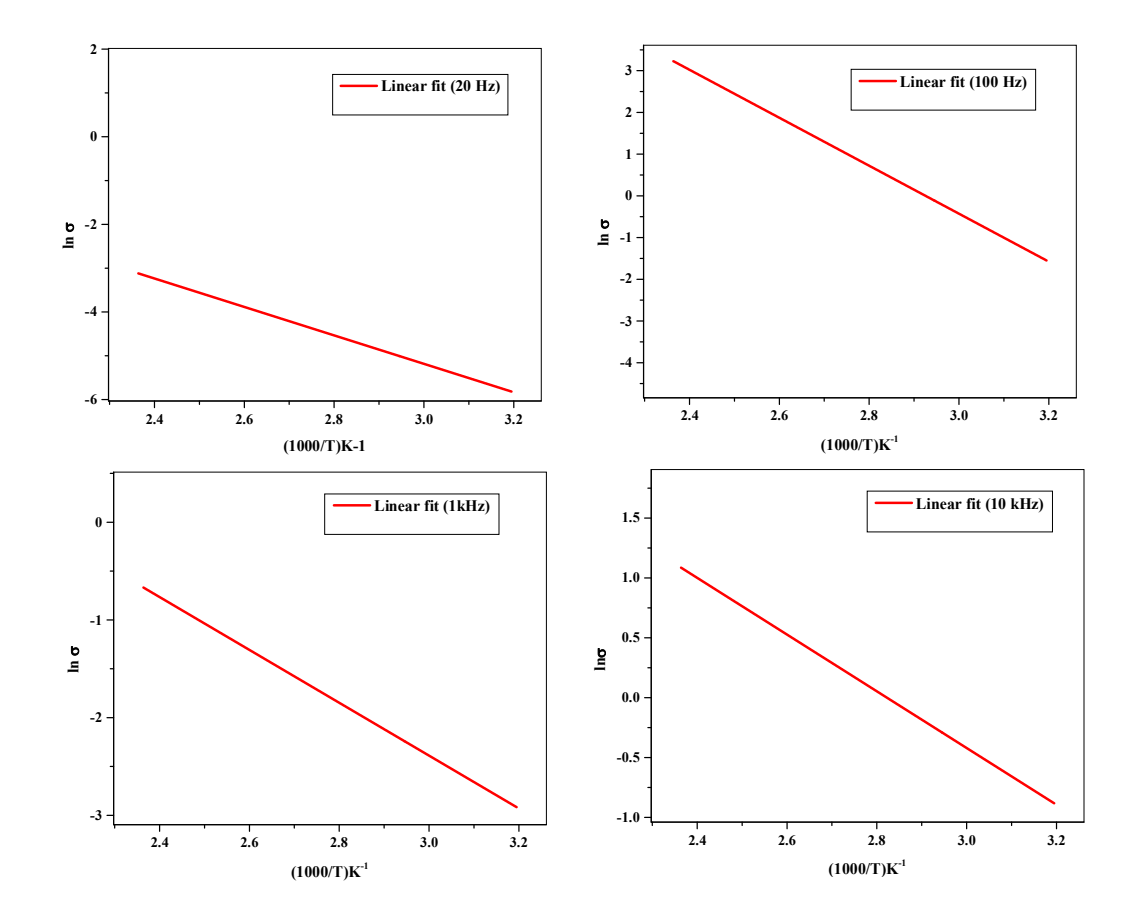


FIG. 8. The variation of a.c. conductivity with temperature for different frequencies for (a) pure CHPD crystals; (b) fruit extracts added CHPD crystals.



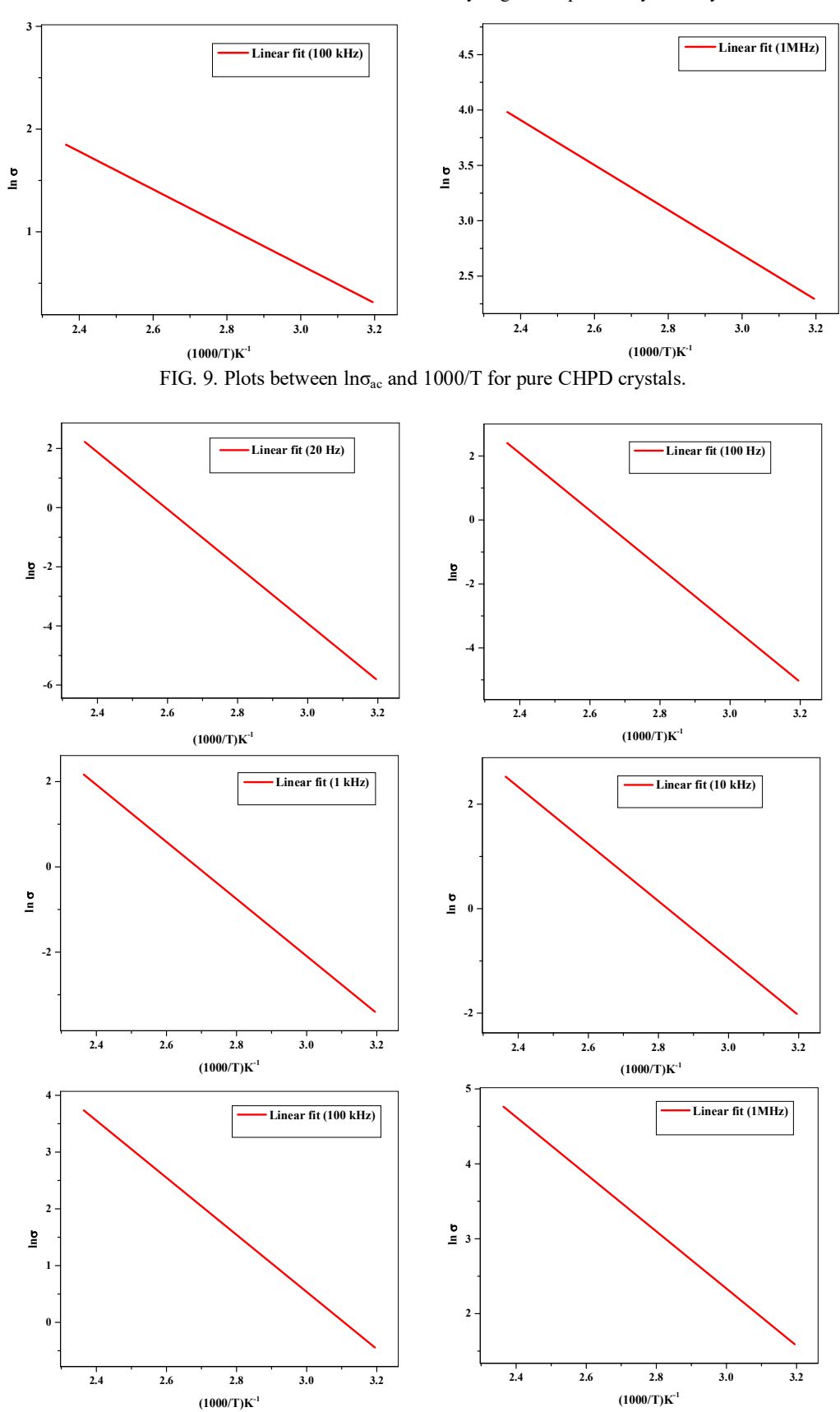


FIG. 10. Plot between  $ln\sigma_{ac} and\ 1000/T$  for fruit extracts added CHPD crystals.

Article Anushya and Freeda

TABLE 2. Values of activation energy (E<sub>g</sub>) at 20 Hz, 100 Hz,1 kHz, 10 kHz, 100 kHz and 1MHz for pure CHPD and fruit extracts added CHPD crystals.

Comples	20 Hz	100 Hz	1 kHz	10 kHz	100 kHz	1 MHz
Samples	(eV)	(eV)	(eV)	(eV)	(eV)	(eV)
Pure CHPD	0.27986	0.49542	0.23309	0.20411	0.15896	0.17482
Fruit extracts added CHPD	0.83197	0.77041	0.57718	0.47100	0.43350	0.32894

The a.c. conductivity  $(\sigma_{ac})$  of a material depends on the dielectric nature of the sample. There is a strong correlation between the temperature dependence and the frequency response of electrical conductivity of materials. In the present case, the frequency-independent conductivity is observed upto 100~kHz, whereas above this frequency it exhibits frequency dispersion. At low frequencies, the bulk a.c. conductivity  $(\sigma_0)$  is almost frequency-independent, but at higher frequencies, the a.c. conductivity increases following power law behavior, such that  $\sigma ac = A\omega^s[9]$ .

The conductivity values at different temperatures are represented by Arrhenius plots.

Arrhenius equation for conductivity is expressed as follows:

$$\sigma = \sigma_0 \exp\left(-E_g/KT\right) \tag{1}$$

where  $\sigma_0$  is the pre-exponential factor,  $E_g$  is the activation energy, K is the Boltzmann's constant and T is the absolute temperature.

Taking the natural logarithm of both sides, the above equation becomes:

$$\ln(\sigma) = \ln(\sigma_0) - E_g / KT \tag{2}$$

Graph of  $ln(\sigma)$  vs. 1000/T is plotted to calculate the value of activation energy.

From Table 2, it is found that the juiceincorporated CHPD crystals exhibit high activation energy and the value of activation energy decreases with increasing frequency. Non-systematic variation of  $E_g$  values was observed for pure CHPD crystals. The value of activation energy given in Table 2 shows that the charge carriers are ionic [21]. Thus, the results obtained indicate that the electrical properties of CHPD crystals could be tuned significantly by addition of fruit extracts.

# Conclusion

Brushite crystals are grown by single diffusion gel growth technique. Powder XRD studies show that the grown brushite crystals exhibit monoclinic structure and the lattice parameters are in good agreement with the literature values [JCPDS no. 72-0713). Reduction in crystalline size with addition of fruit extracts is observed as compared with pure CHPD crystals. The UV-vis analysis showed good transparency of the grown crystals. Electrical parameters, such as dielectric constant and dielectric loss, were found to decrease with increasing the value of frequency of the applied field and a.c. conductivity increased with increasing the value of frequency of the applied field. Activation energy values of the samples have been evaluated. The incorporation of fruit extracts was exhibited very well in the activation energy values with comparison to pure CHPD crystals. This study shows that fruit extracts prepared from natural foods have good inhibitory effect on the growth of the brushite urinary stone crystals considered.

# References

- [1] Smith, L.H. and Werness, P.G., Transactions of the American Clinical and Climatological Association, 95 (1983) 183.
- [2] Fan, J. and Chandoke, P.S., The Journal of Urology, 161 (1999) 1685.
- [3] Menon, M. and Resnick, M., "Urinary Lithiasis: Etiology, Diagnosis and Medical Management". In: P.C. Walsh, A.B. Retic and D. Vaughan (Eds.), "Campbell's Urology", 7<sup>th</sup> Ed., (WB Saunders and Co., Philadelphia, 2003) pp. 2661–2733.
- [4] Trinchieri, A., Urological Research, 34 (2006) 151.
- [5] Christina, A.J., Priya Mole, M. and Moorthy, P., Methods and Findings in Experimental and Clinical Pharmacology, 24(6) (2002) 357.
- [6] Trinchieri, A., Castelnuovo, C., Lizzano, R. and Zanetti, G., Urological Research, 33(3) (2005) 194.
- [7] Joshi, V.S. and Joshi, M.J., Cryst. Res. Technol., 38 (2003) 817.
- [8] Parekh, B.B. and Joshi, M.J., Cryst. Res. Technol., 42 (2007) 127.
- [9] Mott, N.F. and Austin, I.G., Adv. Phys., 18 (1969) 41.
- [10] Lechevallier, E., Saussine, C. and Traxer,O., Prog. Urol., 18 (12) (2008) 912.

- [11] Delius, M., J. Urol., 140(2) (1988) 390.
- [12] Abe, T., Akakura, K., Kawaguchi, M., Ueda, T., Ichikawa, T. and Ito, H., J. Endourol., 19 (7) (2005) 768.
- [13] Chacko, J., Moore, M., Sankey, N. and Chandhoke, P.S., J. Urol., 175(4) (2006) 130.
- [14] Henisch, H.K., Dennis, J. and Hanoka, H.I., J. Phy. Chem. Solids, 26 (1965) 493.
- [15] Joseph, K.C. and Joshi, M.J., Ind. J. Phys., 76A (2002) 159.
- [16] Elizabeth, A., Joseph, C. and Ittyachen, M.A., Bull. Mater. Sci., 24 (2001) 431.
- [17] Patel, A.R. and Venkateswara Rao, A., Bulletin of Materials Science, 4 (5) (1982) 527.
- [18] Srinivasan, N. and Natarajan, S., Indian Journal of Physics, 70 (1996) 563.
- [19] Sivkumar, G.R., Girija, E.K., Narayana Kalkura, S. and Subramanian, C., Crystal Research and Technology, 33(2) (1997) 197.
- [20] Kalkura, S.N., Girija, E.K., Kanakavel, M. and Ramasamy, P., J. Mater. Sci. Mater. Med., 6 (1995) 577.
- [21] Gubkin, A.N. and Skanavi, G.I., t.v. Akad Nauk SSSR SerFiz, 22 (1958) 330.

### Jordan Journal of Physics

#### ARTICLE

# Photoluminescence Behavior of Cu<sub>2+x</sub>Zn<sub>1-x</sub>SnS<sub>4</sub> Thin Films by SILAR Method\*

J. Henry<sup>a</sup>, K. Mohanraj<sup>a</sup> and G. Sivakumar<sup>b</sup>

Received on: 22/5/2017; Accepted on: 19/11/2017

**Abstract:**  $\text{Cu}_2\text{ZnSnS}_4$  thin films were deposited on a glass substrate by chemical method. The XRD pattern confirms the formation of tetragonal structure CZTS and peak shift is noticed for Cu doping. The absorption coefficient is in the order of  $10^4\text{cm}^{-1}$  and the band gap is found to be about 1.9 eV - 1.75 eV. The PL spectra show red shift for higher Cu doping concentrations.

**Keywords:** Photoluminescence, Cu<sub>2</sub>ZnSnS<sub>4</sub> thin films, SILAR Method, XRD.

#### Introduction

Cu<sub>2</sub>ZnSnS<sub>4</sub> (CZTS), a p-type semi-conductor has received significant attention due to its attractive features, such as utilization of abundant metals and high absorbance coefficient of >10<sup>4</sup> cm<sup>-1</sup>[1]. It has a band gap value of about 1.5 eV, which is the optimum value for singlejunction solar cell devices [2]. Optical properties of semi-conductor materials can be tuned by The optical properties of doped doping. nanomaterials differ from those of the corresponding host materials, because the dopants create deep trap levels and act as luminescence centers. Discrete energy states can be introduced in the band gap of semiconducting host by doping with transition metals [3]. Transition metal ion-doped semi-conductors have been investigated intensively, since they can not only retain nearly all intrinsic advantages of semi-conductors, but also possess additional advantages, such as larger Stokes shift to avoid self-absorption/energy transfer, thermal and chemical stability and longer excited state lifetime [4]. Cu plays an irreplaceable role

in modern electronic circuits due to its excellent electrical conductivity [5]. Moreover, optical properties of semi-conductor thin films can be tuned by changing Cu doping concentration.

CZTS thin films have been prepared by physical and chemical methods. There are only few reports available for the preparation of CZTS thin films by low cost Successive Ionic Layer Adsorption and Reaction (SILAR) method. This work aims to study the optical properties of Cu-doped  $Cu_{2+x}Zn_{1-x}SnS_4$  (x=0, 0.02, 0.04, 0.06, 0.08 and 1) thin films.

#### **Experimental Methods**

In this work, A.R.- grade copper chloride (CuCl<sub>2</sub>), zinc chloride (ZnCl<sub>2</sub>), tin chloride (SnCl<sub>2</sub>), sodium sulfide (Na<sub>2</sub>S) and double distilled water were used. Thin films of the Cu<sub>2+x</sub>Zn<sub>1-x</sub>SnS<sub>4</sub> (x = 0, 0.02, 0.04, 0.06, 0.08 and 1) system were deposited on precleaned microscopic glass slides by SILAR method at room temperature. The SILAR method includes

Department of Physics, Manonmaniam Sundaranar University, Tirunelveli- 627 012, Tamilnadu, India.

b CISL, Department of Physics, Annamalai University, Annamalai Nagar-608 002, Tamilnadu, India.

Article Henry et al.

precursor concentration, dipping time and number of cycles. In this work, we have enriched the Cu ion concentration while reducing the Zn ions into the  $\text{Cu}_2\text{ZnSnS}_4$  system.

For synthesis of Cu<sub>2</sub>ZnSnS<sub>4</sub> film, a mixture of cationic precursors (0.1 M CuCl<sub>2</sub>, 0.05 M ZnCl<sub>2</sub> and 0.05 M SnCl<sub>2</sub>) was dissolved in distilled water. The anionic precursor solution was prepared by dissolving 0.2 M Na<sub>2</sub>S in distilled water. First, the precleaned substrates were immersed in the composite cationic solution for 30 s to adsorb Cu<sup>2+</sup>, Zn<sup>2+</sup> and Sn<sup>2+</sup> ions. Then, the substrate was rinsed in distilled water for 10 s to remove the loosely adsorbed ions, if any. After that, the substrate was immersed in the anion solution (S<sup>2</sup>-) for 30 s, where the chemical reaction takes place between anions and cations to form CZTS. The substrate is again rinsed in distilled water for 10 s to remove the powdery precipitate, if any. The above four steps form one SILAR cycle, which was optimized. Similarly, 70 cycles were employed to obtain homogeneous CZTS films. The same procedure was adopted to enrich Cu concentrations (2.02; 2.04; 2.06; 2.08 and 2.10) into the CZTS system. The deposited films were annealed at 200°C for 2h in air atmosphere.

The prepared CZTS films were characterized by using XRD, UV-Vis. and PL techniques. Powder X-ray diffraction (XRD) patterns were performed using a PANalytical X' PERT- PRO diffractometer using Cu K $\alpha$  radiation ( $\lambda$ = 1.5460Å). The diffraction patterns were collected in the range 2 $\theta$ =10°-80°. Optical spectra and PL spectra were recorded using UV-2400PC series, UV-Visible spectrometer and LS-45 Perkin Elmer photoluminescence spectrometer, respectively.

#### **Results and Discussion**

Thickness of the  $Cu_{2+x}Zn_{1-x}SnS_4$  (x = 0, 0.02, 0.04, 0.06, 0.08 and 1) films were determined using optical method [2] given in Table 1. Fig. 1 shows the XRD patterns of CZTS thin films deposited on glass substrates at various x values. The peaks observed at  $2\theta = 28.5^{\circ}$ ,  $32.9^{\circ}$  and 46.39° belong to the (112), (200) and (220) plane, respectively, of tetragonal CZTS phase (JCPDS Card No. 260575). The broad hump is observed around 20 to 30° due to the amorphous glass substrate. The intensity of the (220) plane increases with increase in Cu doping. The prepared CZTS film is polycrystalline in nature. Hence, a large number of grains with various relative positions and orientations variations in the phase difference between the wave scattered by one grain and that by the others. The total intensity scattered by all grains is the sum of individual intensities scattered by each grain [6].

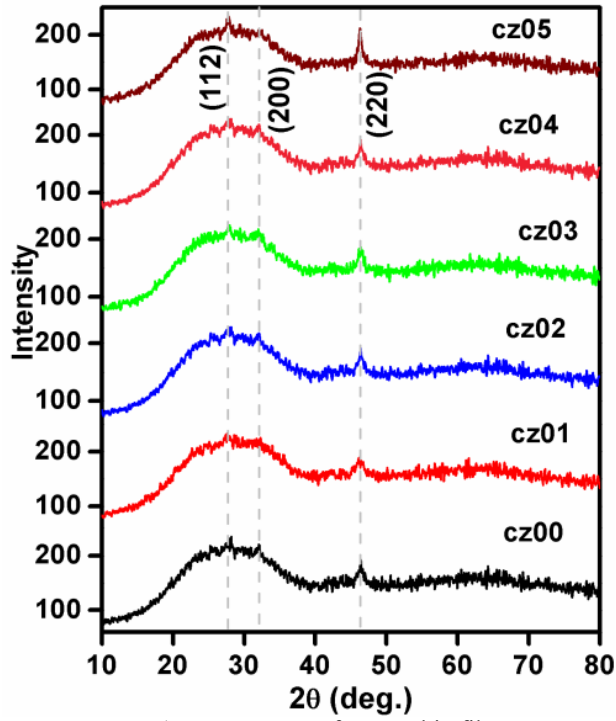


FIG. 1. XRD pattern of CZTS thin film.

The crystalline size was estimated by using Scherrer formula [7]:

$$D = \frac{0.9 \,\lambda}{\beta \cos \theta} \tag{1}$$

where  $\beta$  is full width at half maximum (FWHM),  $\lambda$  is the wavelength of X-ray source and  $\theta$  is the Bragg's angle.

Table 1 shows the thickness and crystalline size of the CZTS thin films deposited at different Cu concentrations. From the table, it is noticed that the crystalline size was found to be increased with increase in cz05. This increase in crystalline size with increase in copper concentration shows the improvement of the CZTS crystallites under Cu-rich conditions [8]. The film thickness is found to be decreased with increase in Cu doping.

TABLE 1. Thickness and crystalline properties of  $Cu_{2+x}Zn_{1-x}SnS_4$  thin films.

		, , ,	2.11	•	
S. No.	Cu:Zn	Name of the	Sample	Thickness of the	Crystalline size
S. NO.	ratio	compound	code	film (nm)	(nm)
1	2.00:1.00	$Cu_2ZnSnS_4$	cz00	800	9
2	2.02:0.98	$Cu_{2.02}Zn_{0.98}SnS_4$	cz01	760	9
3	2.04:0.96	$Cu_{2.04}Zn_{0.96}SnS_4$	cz02	722	8
4	2.06:0.94	$Cu_{2.06}Zn_{0.94}SnS_4$	cz03	617	9
5	2.08:0.92	$Cu_{2.08}Zn_{0.92}SnS_4$	cz04	537	9
6	2.10:0.90	$Cu_{2.10}Zn_{0.9} SnS_4$	cz05	523	17

The optical absorption spectra of the CZTS films are shown in Fig. 2. The optical spectra of CZTS showed good absorption in the range of 400-500 nm. A gradual reduction is noticed in the absorption profile between 400 and 600 nm for all the films, which is attributed to d-d transition of Cu<sup>2+</sup>. The absorption coefficient is

found to be about 10<sup>4</sup> cm<sup>-1</sup>. The band gap plot is shown in Fig. 3 and it is found to be about 1.9-1.75 eV. The band gap is decreased for increased Cu doping. The film cz05 shows lesser bandgap, which may be due to the bigger crystalline size which is confirmed from the XRD analysis.

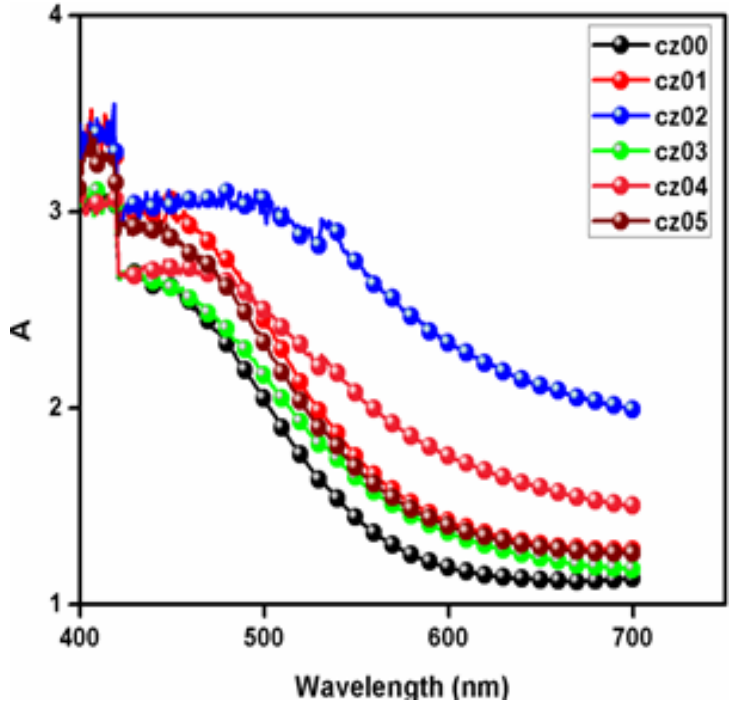


FIG. 2. UV-visible absorption spectra of the CZTS thin films.

Article Henry et al.

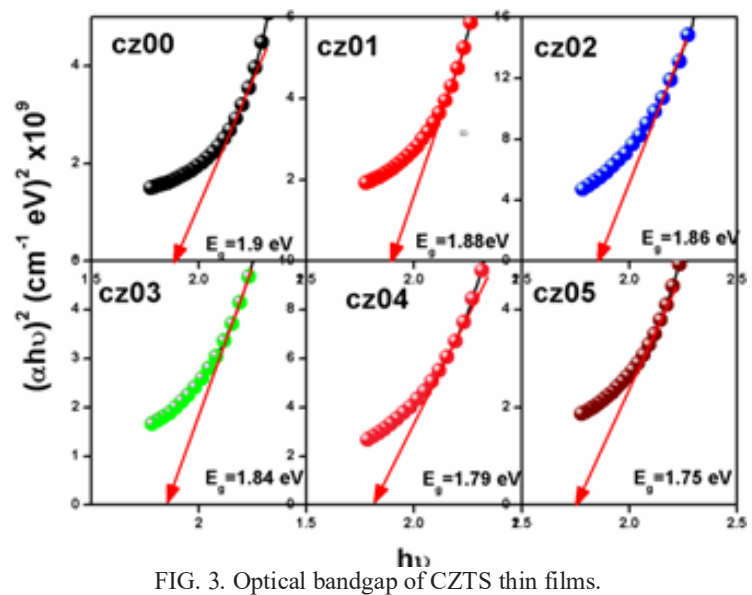


Fig. 4 shows the photoluminescence spectra of  $Cu_{2+x}Zn_{1-x}SnS_4$  (x = 0, 0.02, 0.04, 0.06, 0.08 and 1) thin films in the wavelength range of 300 to 600 nm. It can be seen from the emission spectra that the emission band appears in the visible region around 502 nm for all the deposited films. The result is due to the recombination between the sulphur-vacancyrelated donor and the valence band. The small shift of the PL peak may be due to the indirect recombination of free electrons moving from trap level formed by Cu atoms to the holes in the valence band. These trap levels are in the energy gap and shift toward the valence band on doping [9].

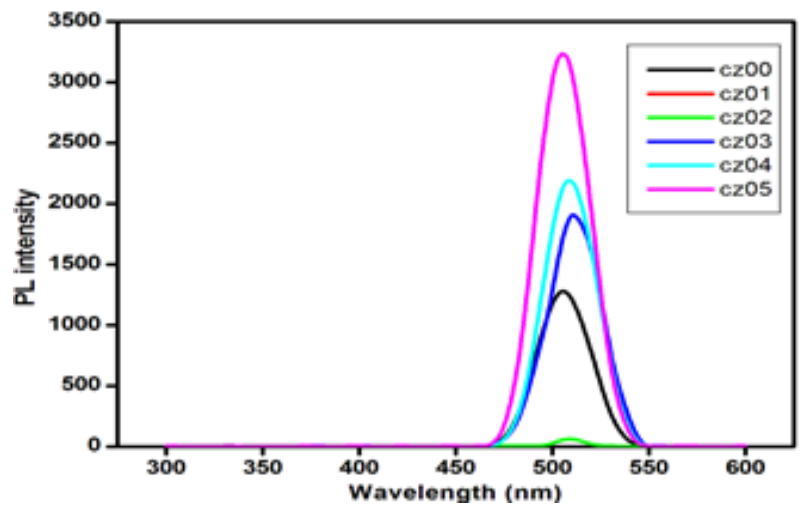


FIG. 4. Photoluminescence spectra of CZTS thin films.

#### Conclusion

 $Cu_{2+x}Zn_{1-x}SnS_4$  (x = 0, 0.02, 0.04, 0.06, 0.08 and 1) thin films were deposited by SILAR method and their optical properties were studied. The XRD pattern confirms the formation of tetragonal structure  $Cu_2ZnSnS_4$ the crystalline size is found to be higher for Cu<sub>20.1</sub>Zn<sub>0.9</sub>SnS<sub>4</sub> thin films. The crystallinity is found to be increased with Cu doping. The 104

deposited CZTS thin films show higher absorption in the visible region and the absorption coefficient is in the order of 10<sup>4</sup>cm<sup>-1</sup>, whereas the band gap is found to be decreased with increase in Cu doping. The PL spectra show red shift for higher Cu doping concentrations. Also, the PL intensity increases with increase in Cu doping.

#### Acknowledgement

The author J. Henry forwards his thanks to University Grants Commission (UGC), New Delhi for providing financial support through UGC Basic Scientific Research (UGC-BSR) fellowship. The authors are thankful to the DST-FIST and UGC-SAP, New Delhi for providing financial support to the Department of Physics, Manonmaniam Sundaranar University.

#### References

- [1] Sarswat, P.K. and Free, M.L. Journal of Crystal Growth, 372 (2013) 87.
- [2] Ge, J., Jiang, J., Yang, P., Peng, C., Huang, Z., Zuo, S., Yang, L. and Chu, J., Solar Energy Materials & Solar Cells, 125 (2014) 20.
- [3] Chawla, A.K., Singhal, S., Nagar, S., Gupta, H.O. and Chandra, R., Journal of Applied Physics, 108 (2010) 123519.
- [4] Han, D., Cao, J., Yang, S., Yang, J., Wang, B., Fan, L., Liu, Q. and Niu, T.W.H., Dalton Trans., 43 (2014) 11019.
- [5] Shyamal, S., Hajra, P., Mandal, H., Singh, J.K., Satpati, A.K., Pande, S. and Bhattacharya, C., ACS Appl. Mater. Interfaces, 7 (2015) 18344.

- [6] Jeyaprakash, B.G., Kesavan, K., Kumar, R.A., Mohan, S. and Amalarani, A., Bull. Mater. Sci., 34 (2011) 601.
- [7] Poormohammadi-Ahandani, Z. and Habibi-Yangjeh, A., Desalination, 271 (2011) 273.
- [8] Suryawanshi, M.P., Shin, S.W., Ghorpade, U.V., Gurav, K.V., Hong, C.W., Agawane, G.L., Vanalakar, S.A., Moon, J.H., Yun, J.H., Patil, P.S., Kim, J.H. and Moholkar, A.V., Electrochimica Acta, 150 (2014) 136.
- [9] Sambasivam, S., Jeong, J.H., Choi, B.C., Lim, K.T., Kim, S.S. and Song, T.K., J. Mater. Res., 26 (2011) 706.

### Jordan Journal of Physics

#### **ARTICLE**

# Dielectric Relaxation Studies on Binary Polar Mixtures of Diethylene Glycol with Ethyl Benzoate Using Time Domain Reflectometry\*

K. Umamakeshvari<sup>a</sup>, A. Mohan<sup>b</sup>, U. Sankar<sup>c</sup> and A.Mozes Ezhil Raj<sup>d</sup>

Received on: 22/5/2017; Accepted on: 25/3/2018

Abstract: It is interesting to study the nature of intermolecular interactions between associative and non-associative polar liquids. Dielectric relaxation measurements on polar-polar binary mixtures of ethyl benzoate with mono diethylene glycol were carried out for eleven different concentrations at temperatures (298K, 303K, 308K and 313K) using Time Domain Reflectometry (TDR) over the frequency range from 10MHz to 10 GHz. The Kirkwood correlation factor and excess dielectric properties were determined and discussed to yield information about the intermolecular interactions in binary system. The non-linear variation has been observed in relaxation time with increasing of alcohol mole concentration. The Bruggeman plot shows a deviation from linearity. This deviation was attributed to some sort of molecular interaction, which may take place between the ester and alcohol molecules. The excess static permittivity and excess inverse relaxation time values are negative for the studied binary systems, indicating the solute-solvent interaction to exist between ester and alcohol, producing a field in such a way that the effective dipole rotation is hindered.

**Keywords:** Dielectric relaxation, Time domain reflectometry, Bruggeman factor, Kirkwood correlation factor.

#### Introduction

Dielectric relaxation study of solute-solvent microwave frequency information about molecular interactions in the system, formation of monomers and multimers. The characterization of dielectric materials includes measurement complex permittivity as a function of frequency at a given temperature or as a function of temperature at a given frequency. The measurement of dielectric properties at wide frequency range gives regarding the conduction information mechanism, interfacial polarization, molecular dynamics and relaxation behavior phenomena [1]. The confirmations of the homogeneous and

heterogeneous molecular interactions in polar binary mixtures are the central topics in liquid state physics and chemistry [1-18]. Dielectric relaxation spectroscopy was proved to be a powerful tool for the investigation of H-bond rearrangement dynamics and has been widely applied to study the pure solvents, solventsolvent mixtures [19, 20]. The presence of hydrogen bonding brings a considerable change in the relaxation time and dipole moment of the binary system, with respect to the corresponding values in the pure components [21]. Dielectric investigation of binary polar liquid mixtures consisting of one associative and other nonassociative provides liquids, valuable

Corresponding Author: K. Umamakeshvari Email: chitra.uma86@gmail.com \*\*\*6<sup>th</sup> National Seminar on Advances in Materials Science NSAMS-2017, held on March 2, 3-2017 at the Department of Physics, Manonmaniam Sundaranar University, Tirunelveli-627 012, Tamilnadu, India".

<sup>&</sup>lt;sup>a</sup> Department of Physics, St. Johns College, Palayamkottai, Tamilnadu, India.

b Department of Physics, VIT University, Katpadi, Vellore, Tamilnadu, India.

<sup>&</sup>lt;sup>c</sup> Department of Physics, Sri KGS Arts College, Srivaikuntam, Tamilnadu, India.

 $<sup>^</sup>d$  Department of Physics, Scott Christian College, Nagercoil, Tamilnadu, India.

Article Umamakeshvari et al.

information regarding molecular complex formation in solution. Esters are non-associated polar liquids with C=0 group. Alcohols are industrially and scientifically important organic compounds and their physical and chemical properties are largely determined by the OH-group. Alcohols are strongly associated in solution because of dipole-dipole interaction and hydrogen bonding.

The strength of the molecular association depends on several factors, including the molecular structure, temperature, solvent and other factors [22]. Therefore, the solution chemistry of these compounds can be strongly influenced by the aggregation phenomena, which can play a significant role in the physical properties of these polar molecules [23]. Dielectric relaxation studies of aromatic esters in the microwave region for different temperatures are reported by Saxena et al. [24] using the Higasi method. There are many studies of the dielectric behavior of alcohol mixtures with structure breaking and structure making [25-30]. The studies of Kirkwood correlation factor provide valuable information regarding the solute-solvent interactions in binary mixtures, especially when one of the components has antiparallel orientation of dipoles [31].

In course of the present study, the dielectric parameters for aromatic ester ethyl benzoate, with diethylene glycol were investigated experimentally for different concentrations in the microwave region (10MHz to 10 GHz) at 298K, 303K, 308K and 313K using time domain reflectometry (TDR). The relaxation behavior of these mixtures was explained by the Debye model. The excess dielectric properties are reported. The Kirkwood correlation factor is used to understand the molecular orientation in the mixture.

#### **Materials and Methods**

#### **Materials and Sample Preparation**

AR grade alcohol (≥99.5% of diethylene glycol) was purchased from Sd Fine Chemicals. AR grade esters (≥99.5% of ethyl benzoate) were supplied by Sigma Aldrich India. The chemical compounds were used without further purification. In each system, nine different solute concentration binary mixtures were prepared gravimetrically.

#### Measurements

The densities of pure compounds were measured by relative density method using 10 ml specific gravity bottle. The mass measurements were performed using digital electronic balance (Adventurer Ohaus AR2140) with an accuracy of Abbe's refractometer (SIPCON  $\pm 0.0001$ g. model) with sodium D line was used to measure the refractive indices of mixture solutions at different temperatures. Constant temperature was maintained by water circulating (ESCY IC 201 model) temperature controller system with an accuracy of 0.1 K. The square of refractive index value was taken as optical frequency dielectric constant ( $n^2 = \varepsilon_{\infty}$ ). The uncertainties of measured density and refractive index were  $\pm 0.2 \text{ kg} \cdot \text{m}^{-3}$ and 0.00005, respectively. Frequency dependent complex dielectric spectra of pure compounds and their binary mixtures were determined by (AgilentnfinijumDCA-J86100 A with sample oscilloscope HP 54754 A model) TDR. A 39 ps rise time step voltage pulse was generated by a tunnel diode and fed through 50  $\Omega$  impedance semi rigid coaxial cable having pin length of 0.135 mm. Coaxial probe was dipped in the sample cell which was shielded by water circulating temperature control system with an accuracy of 0.5 K. All measurements were carried out in an open load condition. The variation in step pulse was monitored after it is reflected from air and sample by sample oscilloscope and recorded in time window of 2 ns. The reflected pulses were digitized into 1200 points and used for further data analysis. The frequency dependent complex spectra were obtained from reflection coefficient spectra. The procedures for data analysis were discussed in previous reports [32, 33]. The measured refractive index and density values were reported in Table 1(a) &1(b), respectively.

TABLE 1(a). Refractive index values of DEG + EB binary mixture at different temperatures.

டம	LB omary mixture at different temperatures.						
$X_2$	298k	303k	308k	313k			
0	1.38723	1.38300	1.37895	1.37484			
0.1	1.38698	1.38273	1.37861	1.37452			
0.2	1.38675	1.38247	1.37831	1.37422			
0.3	1.38650	1.38219	1.37797	1.37389			
0.4	1.38623	1.38189	1.37760	1.37353			
0.5	1.38594	1.38157	1.37722	1.37315			
0.6	1.38565	1.38126	1.37683	1.37278			
0.7	1.38532	1.38089	1.37638	1.37235			
0.8	1.38496	1.38048	1.37590	1.37187			
0.9	1.38458	1.38005	1.37538	1.37136			
1	1.38418	1.37961	1.37484	1.37084			

TABLE 1(b). Density values of DEG and EB at different temperatures.

Toman	Diethyleneelyseel	Ethyl hanzaata
Temp	Diethyleneglycol	Ethyl benzoate
298k	1.12894	1.04152
303k	1.10963	1.03801
308k	1.10372	1.03486
313k	1.09830	1.03099

#### **Results and Discussion**

An example of frequency spectrum of complex dielectric constant ( $\epsilon$ ',  $\epsilon$ ") of diethylene glycol at 298K is shown in Fig. 2. The values of maximum dielectric loss ( $\epsilon$ "<sub>max</sub>) decrease with the increase in degree of polymerization (Fig. 1). It is because of the increase in molecular size of the DEG molecules.

The complex dielectric permittivity

 $\varepsilon^*(\omega) = \varepsilon' - j\varepsilon''$  was fitted with the Havriliak- Negami epression [34]:

$$\varepsilon * (\omega) = \varepsilon_{\infty} + \frac{\left(\varepsilon_{0} - \varepsilon_{\infty}\right)}{\left[1 + \left(j\omega\tau\right)^{1-\alpha}\right]^{\beta}}$$
(1)

with  $\varepsilon_0$ ,  $\varepsilon_\infty$ ,  $\tau$ ,  $\alpha$  and  $\beta$  as fitting parameters.  $\varepsilon_0$  is the static permittivity at limiting low frequency,  $\varepsilon_\infty$  is the limiting high frequency permittivity and is not fitted and assumed to be 3.5 for all concentrations studied here,  $\tau$  is the average relaxation time,  $\alpha$  and  $\beta$  are the distribution parameters and  $\omega$  is the angular frequency.

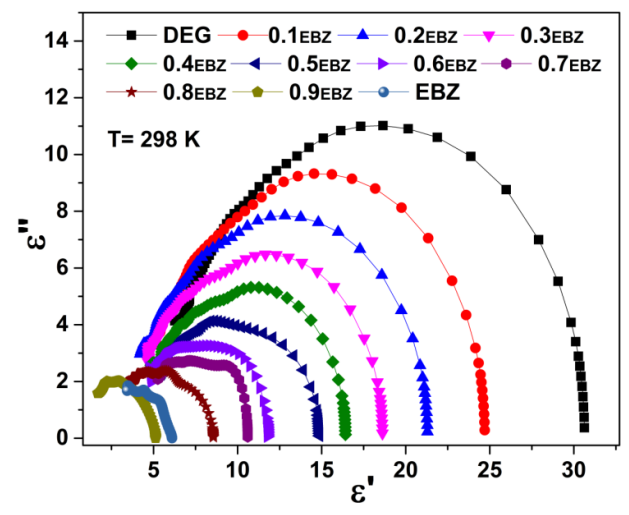


FIG. 1. Cole-cole plot at 298K for 11 different molefractions.

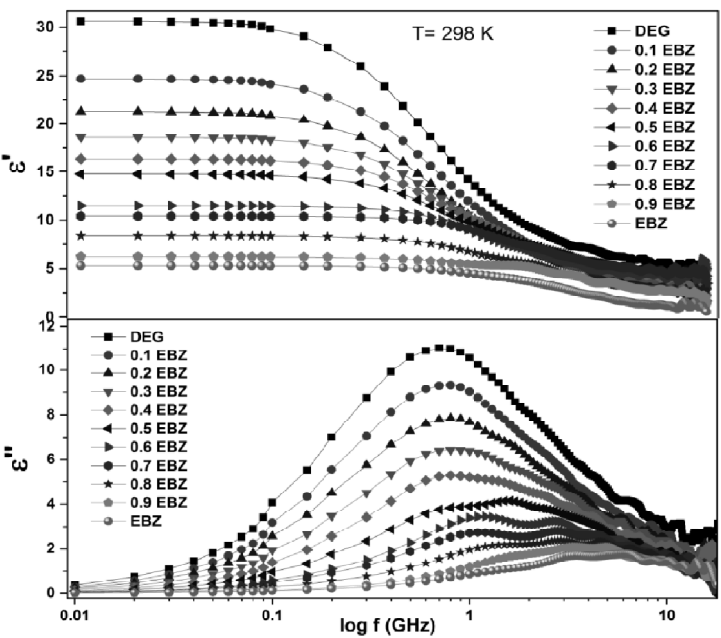


FIG. 2. Complex permittivity spectra of DEG+EB at 298K for 11 different molefractions.

Article Umamakeshvari et al.

The Havriliak-Negami [34] expression includes the Cole-Cole ( $\beta$ =1), Davidson-Cole ( $\alpha$ =0) and Debye ( $\alpha$ =0,  $\beta$ =1) relaxation models. A non- linear least squares fitting method was used to determine the values of the dielectric parameters [35]. Complex permittivity spectra for the binary mixture of DEG + EB are plotted in Fig.2.

The values of different dielectric parameters for DEG + EB binary mixture obtained by the Havriliak-Negami equation are presented in Table 2. It is observed that the dielectric relaxation in these mixtures can be represented by the Davidson-Cole relaxation behavior. However, at higher concentrations of EB in DEG, the dielectric dispersion spectra (Fig. 2) can be fitted with the Debye behavior ( $\alpha$ =0,  $\beta$ =1). The observed values of dielectric

parameter for DEG are in good agreement with those reported earlier [25]. The static dielectric constant decreases with the increase in degree of polymerization (Table 2). This is consistent with the behavior obtained by Sengwa *et al.* [36, 37].

The static dielectric constant decreases with the increase in molefraction of EB. Relaxation time also decreases with the increase in molefraction of EB. The increase in static dielectric constant in DEG + EB combination suggests that a single volume effect arises from the solute particles, thereby reducing their ability to orient in the applied field and so reducing the static dielectric constant. From the dielectric relaxation studies, it has been observed that the relaxation time  $(\tau_0)$  of DEG in EB solutions increases with increasing DEG concentrations.

TABLE 2. Dielectric parameters of DEG + EB mixtures.

	$\epsilon_0$					$\tau_0$	ps)	
$(X_2)$	298K	303K	308K	313K	298K	303K	308K	313K
0.1	30.6	29.6	27.3	26.0	198.1	168.6	143.6	120.0
0.2	24.3	25.1	23.5	23.4	186.0	163.0	135.7	116.5
0.3	20.9	22.1	19.9	19.3	177.8	171.2	126.7	110.2
0.4	18.2	16.8	16.5	16.7	154.5	130.0	110.8	96.3
0.5	16.0	15.2	14.5	14.0	133.3	119.4	98.6	90.5
0.5	14.4	12.6	12.2	12.4	121.2	108.2	86.7	80.5
0.6	11.4	11.0	9.5	10.5	93.0	90.6	60.1	68.5
0.7	10.4	10.2	8.2	8.2	69.4	76.2	62.9	46.0
0.8	8.2	7.2	7.0	6.1	72.5	57.4	44.3	31.6
0.9	6.1	6.3	6.0	5.6	50.7	36.4	35.7	24.3
1.0	5.5	5.5	4.9	5.3	45.6	32.8	25.5	22.1

#### **Kirkwood Correlation Factor**

The Kirkwood correlation factor g gives the association effect due to the hydrogen bonding in the system [34]. The value of g in pure liquid can be obtained by the following equation [38]:

$$\frac{4\pi N\rho}{9kTM}g\mu^{2} = \frac{\left(\varepsilon_{0} - \varepsilon_{\infty}\right)\left(2\varepsilon_{0} + \varepsilon_{\infty}\right)}{\varepsilon_{0}\left(\varepsilon_{\infty} + 2\right)^{2}}.$$
 (2)

For a binary mixture of dipolar liquids, the static dielectric permittivity needs to be considered as the dipole orientation correlation factor [38]. The modified form of Eq. (2) is used to study the orientation of electric dipoles in the binary mixtures as follows:

$$\frac{4\pi N}{9kT} \left( \frac{\mu_1^2 \rho_1}{M_1} X_1 + \frac{\mu_2^2 \rho_2}{M_2} X_2 \right) \times g^{eff} = \frac{\left(\epsilon_{om} - \epsilon_{\infty m}\right) \left(2\epsilon_{om} + \epsilon_{\infty m}\right)}{\epsilon_{om} \left(\epsilon_{\infty m} + 2\right)^2}$$
(3)

where  $\mu_1$ ,  $\rho_1$ ,  $M_1$  and  $X_1$  represent the Diethylene glycol dipole moment in gaseous state, density, molecular weight and molefraction, respectively.  $\mu_2$ ,  $\rho_2$ ,  $M_2$  and  $X_2$  represent the ethyl benzoate dipole moment in gaseous state, density, molecular weight and molefraction, respectively. The  $\epsilon_{0m}$  and  $\epsilon_{\infty m}$  are mixture dielectric constant and mixture dielectric constant at optical frequency ( $n^2 = \epsilon_{\infty m}$ ), respectively.  $g^{eff}$  is the effective Kirkwood correlation factor, that changes from Kirkwood correlation factor of one pure liquid to that of another liquid. If  $g^{eff} = 1$ , it

Dielectric Relaxation Studies on Binary Polar Mixtures of Diethylene Glycol with Ethyl Benzoate Using Time Domain Reflectometry

indicates that no association exists between unlike molecules in the mixture. If  $g^{\rm eff} > 1$ , it indicates the existence of association between unlike molecules through parallel dipole interaction. Similarly, if  $g^{\rm eff} < 1$ , it indicates the existence of association between unlike molecules through anti-parallel dipoles. The Kirkwood correlation factors for DEG in EB at

different temperatures are given in Table 3. The observed ( $g^{eff}$ ) values are greater than unity in all these DEG molecules, which leads to the conclusion that the molecules associate to form a multimer with parallel dipole moment. The Kirkwood correlation factor values for DEG are smaller than the corresponding values in EB.

TABLE 3. Kirkwood correlation factor for DEG + EB binary mixtures	TABLE 3. Kirkwood	correlation f	factor for	DEG + 1	EB bin	ary mixtures
-------------------------------------------------------------------	-------------------	---------------	------------	---------	--------	--------------

	g <sup>eff</sup>						
$(X_2)$	298K	303K	308K	313K			
0.0	3.340	3.298	3.101	3.013			
0.1	2.767	2.932	2.800	2.849			
0.2	2.495	2.705	2.483	2.457			
0.3	2.286	2.149	2.154	2.224			
0.4	2.121	2.045	1.991	1.968			
0.5	2.016	1.783	1.759	1.838			
0.6	1.681	1.644	1.427	1.631			
0.7	1.624	1.627	1.290	1.322			
0.8	1.335	1.170	1.158	0.996			
0.9	1.004	1.075	1.042	0.980			
1.0	0.972	0.983	0.856	0.988			

The excess permittivity  $\varepsilon_0^E$  and the excess inverse of the relaxation time  $(1/\tau)^E$  for diethylene glycol in ethyl benzoate mixtures are determined using the following equations [10, 38]:

$$\varepsilon_0^E = (\varepsilon_0)_{M} - \left[ (\varepsilon_0)_{W} X_2 + (\varepsilon_0)_{S} (1 - X_2) \right]$$
 (4)

$$\left(\frac{1}{\tau}\right)^{E} = \left(\frac{1}{\tau}\right)_{m} - \left[\left(\frac{1}{\tau}\right)_{1} X_{1} + \left(\frac{1}{\tau}\right)_{2} X_{2}\right] \tag{5}$$

Here, the subscripts M, W and S correspond to the mixture, Diethylene glycol and Ethyl benzoate, respectively and  $X_2$  is the molefraction of EB in DEG. The variations of  $(\epsilon_0)^E$  and  $(1/\tau)^E$  with molefraction of EB  $(X_2)$  in DEG are shown in Fig. 3(a, b).

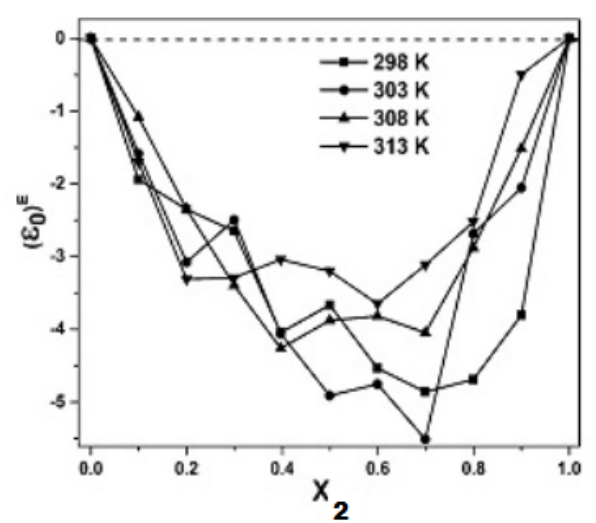


FIG. 3(a). Excess dielectric permittivity  $(\epsilon_0^E)$  versus molefraction of ethyl benzoate  $(X_2)$  in DEG at different temperatures.

Article Umamakeshvari et al.

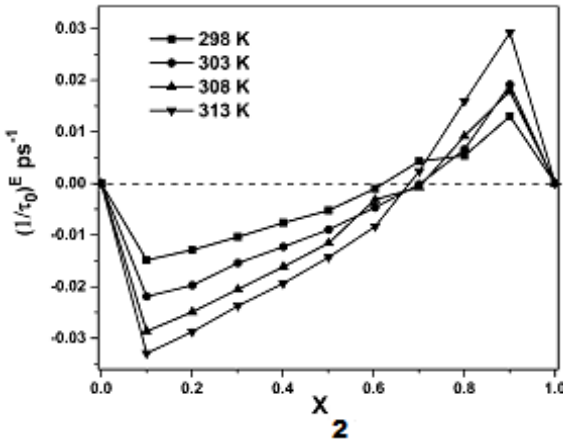


FIG. 3(b). The excess inverse relaxation time  $(1/\tau)^E$ ) in GHz versus molefraction (X<sub>2</sub>) of ethyl benzoate in DEG at different temperatures.

The excess dielectric constants for DEG + EB binary mixtures show negative behavior. The maxima are found to be in the EB-rich region  $(X_2 = 0.7)$ . The negative values of excess parameters suggest that the addition of DEG to EB may create multimeric structure leading to a decrease in total permittivity as indicated by Fig. 3(a). The excess inverse relaxation times of these systems are positive in the EB-rich region. This indicates fast rotation of the dipoles. This may be due to the formation of monomeric structures in this region. In the DEG-rich region, these values are negative. This indicates the formation of structures; probably dimeric, which rotate slowly as in Fig. 3(b).

#### **Bruggeman Dielectric Factor**

The static permittivity of a mixture of two liquids lies in between two extremes of the static permittivity of the components.

Bruggeman [39] equation for binary mixture is given by:

$$f_{B} = \left[ \frac{\left(\varepsilon_{0m} - \varepsilon_{02}\right)}{\left(\varepsilon_{01} - \varepsilon_{02}\right)} \right] \left(\frac{\varepsilon_{01}}{\varepsilon_{0m}}\right)^{1/3} = 1 - X_{2}$$
 (6)

where  $f_B$  is the Bruggeman dielectric factor.  $\epsilon_{0m}$ ,  $\epsilon_{01}$  and  $\epsilon_{02}$  are the static dielectric constants corresponding to mixture DEG.

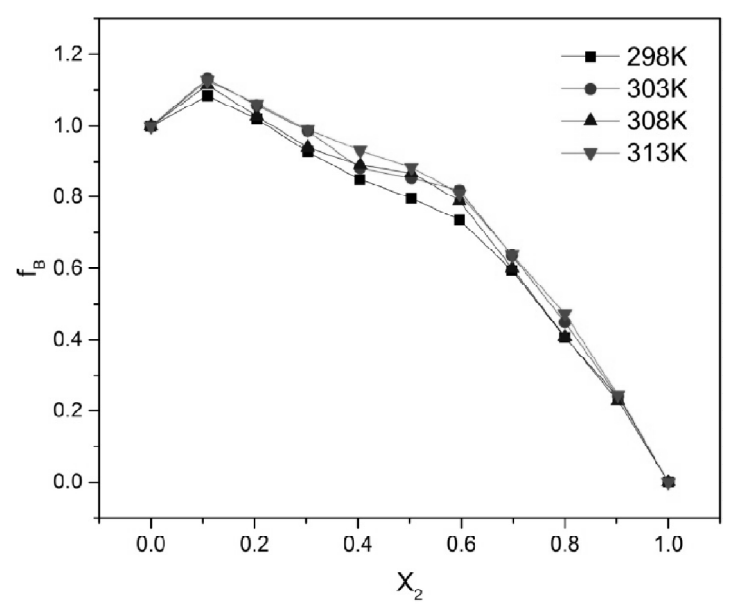


FIG. 4. Bruggeman dielectric factor (f<sub>B</sub>) versus molefraction of EB in DEG at different temperatures.

X<sub>2</sub> is the molefraction of EB. The non-linear variation of Bruggeman factor with molefraction shows hetero-interaction, which may be due to

hydrogen bonding of the-OH group of DEG with C=O of EB. The Bruggeman equation may be modified as:

Dielectric Relaxation Studies on Binary Polar Mixtures of Diethylene Glycol with Ethyl Benzoate Using Time Domain Reflectometry

$$f_B = \left[\frac{\left(\varepsilon_{0m} - \varepsilon_{02}\right)}{\left(\varepsilon_{01} - \varepsilon_{02}\right)}\right] \left(\frac{\varepsilon_{01}}{\varepsilon_{0m}}\right)^{1/3} = 1 - \left[a - \left(a - 1\right)X_2\right]X_2$$

(7)

The molefraction  $(X_2)$  is modified by a factor of  $1-\left[a-\left(a-1\right)X_2\right]X_2$ . The value of a contains the information regarding the change in the orientation of EB molecules in the mixture. The value of a has been determined by the least squares fit method and found to be 1.85 in DEG-EB mixtures. The value of a suggests that the effective volume fraction of diethylene glycol in ethyl benzoate solution is reduced considerably, indicating significant interaction between diethylene glycol and ethyl benzoate in the mixtures.

#### Conclusion

In this study, the concentrationdielectric temperature-dependent complex spectra of ethyl benzoate with diethylene glycol have been investigated in the frequency range from 10 MHz to 10 GHz using Time Domain Reflectometry (TDR) method. The following conclusions could be drawn from the detailed analysis. The value of dielectric parameters shows the systematic change with increase in EB concentration, temperature and alcohol chain formation of intermolecular length. The interaction between solute and solvent molecules in the mixture has been confirmed from nonlinear behavior of dielectric parameters with EB molefraction. The excess dielectric constant results show that the heterogeneous interaction strength increases with the increase in alcohol molecular size and stable aggregates formed at 1:2 ratio in DEG + EB binary systems. The excess inverse relaxation time values confirm that the intermolecular interaction produces the electric field which leads effective dipoles to rotate faster.

#### References

- [1] Lux, A. and Stockhausen, M., Phys. Chem. Liq., 26 (1993) 67.
- [2] Sato, T., Chiba, A. and Nozaki, R., J. Chem. Phys., 112 (2000) 2924.
- [3] Sato, T., Chiba, A. and Nozaki, R., J. Mol. Liq., 96–97 (2002) 325.
- [4] Sato, T. and Buchner, R., J. Chem. Phys., 118 (2003) 4606.
- [5] Sengwa, R.J., Choudhary, R. and Mehrotra, S.C., Molec. Phys., 99 (2001) 1805.
- [6] Sengwa, R.J., Choudhary, R. and Mehrotra, S.C., Polymer, 43 (2002) 1467.
- [7] Sengwa, R.J., Abhilasha and More, N.M., Polymer, 44 (2003) 2577.
- [8] Sengwa, R.J., Abhilasha, More, N.M. and Mehrotra, S.C., J. Polym. Sci.: Part B: Polym. Phys., 43 (2005) 1134.
- [9] Bateman, J.B. and Gabriel, C., J. Chem. Soc., Faraday Trans., 2 (83) (1987) 355.
- [10] Kumbharkhane, A.C., Puranik, S.M. and Mehrotra, S.C., J. Chem. Soc., Faraday Trans., 87 (1991) 1569.

- [11] Hosamani, M.T., Pattepur, R.H., Deshpande, D.K. and Mehrotra, S.C., J. Chem. Soc., Faraday Trans., 91 (1995) 623.
- [12] Pawar, V.P. and Mehrotra, S.C., J. Mol. Liq., 115 (2004) 17.
- [13] Sudo, S., Shinyashiki, N., Kitsuki, Y. and Yagihara, S., J. Phys. Chem., A106 (2002) 458.
- [14] Sudo, S., Shinyashiki, N. and Yagihara, S., J. Mol. Liq., 90 (2001) 113.
- [15] Kaatze, U., Kettler, M. and Pottel, R., J. Phys. Chem., 100 (1996) 2360.
- [16] Wilke, G., Betting, H. and Stockhausen, M., Phys. Chem. Liq., 36 (1998) 199.
- [17] Barthel, J., Bachhuber, K., Buchner, R. and Hetzenauer, H., Chem. Phys. Lett., 165 (1990) 369.
- [18] Chaudhari, A., Chaudhari, H.C. and Mehrotra, S.C., Bull. Korean Chem. Soc., 25 (2004) 1403.
- [19] Ediger, M.D, Angell, C.A. and Nagel, S.R., J. Chem. Phys., 100 (1996) 13200.

Article Umamakeshvari et al.

[20] Nath, G., Sahu, S. and Paikaray, R., Indian J. Phys., 83 (2009) 429.

- [21] Kroegemr, K., J. Molec. Liquids, 36 (1987) 101.
- [22] Gupta, K.K., Bnashal, A.K., Singh, P.J. and Sharma, K.S., Indian J. Pure and Appl. Phys., 41 (2003) 57.
- [23] Rowlinson, J.S. and Swinton, F.L., "Liquids and Liquid Mixtures", 3<sup>rd</sup> Edn., (Butterworth, London, 1982).
- [24] Saxena, S.K. and Saxena, M.C., Indian J. Pure & Appl. Phys., 19 (1981) 550.
- [25] Kumbharkhane, A.C., Puranik, S.M. and Mehrotra, S.C., J. Pure Appl. Phys., 4 (1992) 62.
- [26] Puranik, S.M., Kumbharkhane, A.C. and Mehrotra, S.C., Proc. Natl. Acad. Sci. India, 63 (1993) 415.
- [27] Kumbharkhane, A.C., Puranik, S.M. and Mehrotra, S.C., J. Mol. Liq., 51(1992) 303.
- [28] Chaudhri, A., Khirade, P., Singh, R., Helambe, S.N., Narain, N.K. and Mehrotra, S.C., J. Mol. Liq., 82 (1999) 245.
- [29] Helambe, S.N., Chaudhri, A. and Mehrotra, S.C., J. Mol. Liq., 84 (2000)235.

- [30] Rana, V.A. and Vyas, A.D., J. Mol. Liq., 102 (1–3) (2002) 379.
- [31] Hosamani, M.T., Fattepur, R.H., Deshpande, D.K. and Mehrotra, S.C., J. Chem. Soc., Faraday Trans., 91(4) (1995) 623.
- [32] Kumar, P.M. and Malathi, M., J. Mol. Liq., 145 (2009) 5.
- [33] Chaube, H.A., Rana, V.A., Hudge, P. and Kumbharkhane, A.C., J. Mol. Liq., 193 (2014) 29.
- [34] Havriliak, S. and Negami, S., Polymer, 8 (1967) 161.
- [35] Bevington, P.R., "Data Reduction and Error Analysis for Physical Sciences", (Mc Graw Hill, New York, 1969).
- [36] Sengwa, R.J., Kaur, K. and Chaudhari, R., Polym. Int., 49 (2000) 599.
- [37] Sengwa, R.J., Polym. Int., 45 (1998) 43.
- [38] Kumbharkane, A.C., Helambe, S.N., Doraiswamy, S. and Mehrothra, S.C., J. Chem. Phys., 99(4) (1993) 2405.
- [39] Bruggeman, D.A.G., Ann. Phys., 5 (1935) 636.

### Jordan Journal of Physics

#### **ARTICLE**

# Analysis of the Force Exerted on an Accelerated Beam of Electrons by Its Own Wakefield in the Laser-Driven Rf-gun

N. M. Ershaidat<sup>a</sup> and W. Salah<sup>b</sup>

Received on: 9/9/2017; Accepted on: 12/12/2017

Abstract: Analytical expressions for the wakefield force acting on an electrons beam, in the RF-photoinjector, during the beam extraction from the cathode, are derived. These expressions are obtained by taking space charge effects and beam motion into account. The former is described in terms of the field's components due to Lienard-Wiechert potential and the method of images, close to the cathode surface. The beam motion is emphasized circumstantiating the fast transition, owing to quick acceleration by the high gradient RF-accelerating field, from thermal velocity, near the immediate vicinity of the cathode, to a non-relativistic velocity at the end of the photoemission. Numerical investigation of the beam wakefield force elicited two significant effects on the beam: the first one, attributable to the longitudinal component of the force, influences the trailing electrons in the beam and changes the energy of the individual electrons, depending on their position. The second one, attributable to the transverse component of the force, deflects the beam trajectory. After all, the electrons within the beam feel, over the beam length, an average deflecting force that is proportional to the radial displacement.

**Keywords:** Free electron laser, Beam dynamics, Wakefields, RF-photoinjector.

PACS: 41.75.Jv Laser-driven acceleration, 41.75 Lx Other advanced accelerator concepts, 41.75.Ht Relativistic electron and positron beams.

#### Introduction

The performance of lasing operation of free electron laser (FEL) [1-2] and laser- Compton Xray [3-5] is based on the so-called self-amplified spontaneous emission (SASE) principle. The achievement of X-ray-SASE-FELs notably requires high beam brightness that is currently beyond the state of the art in addition to very low beam emittance [6-7]. Nowadays, laser-driven radio-frequency electron guns are substantially used to generate intense beams with low emittance and high brightness near the thermal source limit [8-9]. Usually, the emittance is defined as a statistical value in phase space [10-13], while the brightness is defined as the ratio of the beam current to the emittance [14-15]. During the emission as well as the acceleration

of the electrons beam from the cathode to the accelerator exit, the beam qualities are degraded by the so-called wakefield.

In non-relativistic regime, the wakefield is the sum of the space charge field and the beam induced field. In ultra-relativistic regime, the wakefield has been addressed numerically, in the last two decades, by many authors using computer codes, such as MAFIA TS3 [16] and ASTRA [17]. The former code calculates the space charge forces of the beam itself; it includes the interaction of the charged particles with the surrounding structure. Despite the accurate results obtained by MAFIA, it is restricted in its application to short sections of the injector due to memory consumption, computation time and

Corresponding Author: Nidal M. Ershaidat Email: n.ershaidat@ju.edu.jo

<sup>&</sup>lt;sup>a</sup> Physics Department, The University of Jordan, Amman 11942, Jordan.

<sup>&</sup>lt;sup>b</sup> Physics Department, The Hashemite University, Zarqa 13115, Jordan.

Article Ershaidat and Salah

numerical noise. The latter code is able to calculate large parts of the accelerator, but it does not take the interaction between the electrons in the beam and the surrounding structure into account. Inappropriately, an unwary common assumption in these codes was the invariance of beam velocity, these codes assuming that the photoelectrons are emerging from the cathode at the speed of light, in congruousness to a situation like that faced in photoinjectors, where the photoelectron beam is hurriedly accelerated by the strong RF-field applied at the cathode surface and attending relativistic velocity at the exit of the photoinjector. Therefore, the electrodynamics of the effects of acceleration-radiation field must be taken into account, in addition to the field produced by the electron beam itself [18].

Over the years, only few works involving the idea of a wakefield driven by an accelerated electron beam are found in the literature [19]. As an example, W. Salah and co-workers have intensely derived analytical expressions for the wakefield driven by an accelerated electron beam in the RF-photoinjector cavity [19-24]. In these works, the beam is traveling substantially with variable velocity less than the velocity of light and hence Kim monokinetic approximation [25] is far from being applied.

On the other hand, the space charge effects and the beam-induced fields are significant within 1cm of the cathode, where the beam is at low energy. At this stage, non-relativistic electrons are very sensitive to space-charge forces and the forces due to the field of the beam image in the cathode. Inside the pulse, electrons experience both longitudinal RF dynamics effects and wakefield effects, both effects leading to degrading the beam quality. The present work is devoted to the quantification of these effects.

In this paper, the authors' intent is to investigate numerically the short-range wakefield forces acting on the beam during the early beam transport; *i.e.*, emitted and strongly accelerated during its photoemission from the cathode. During the beam emission from the cathode, the self-field effects are not of space charge type, consequent to an electrostatic description in some beam proper frame. The self-field is an electromagnetic field, where relativistic effects of retardation and acceleration field play an important role. The wakefield force

excited in this regime will be analyzed in some detail using Lienard-Weichert potential and the method of images [24]. This technique will be applied to parameters of the "ELSA" photoinjector facility [19] as shown in Fig. 1. As was justified in Ref. [23], we restrict our modelling to a "pill-box" type cavity. On the other hand, analytical and semi-empirical results [25-26] indicate that the influence of the exit

hole can be neglected as long as  $r_0/\Re \ll \frac{1}{3}$ ,

where  $r_0$  and  $\Re$  are the hole and cavity radii, respectively (Fig. 1).

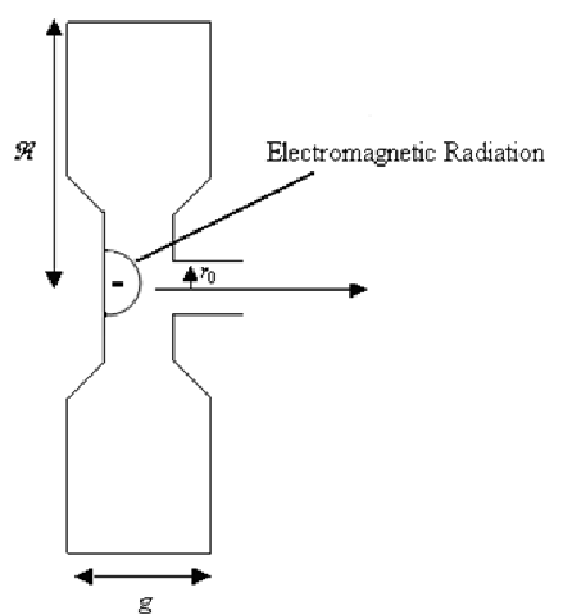


FIG. 1. "ELSA" photo-injector (144 MHz cavity).

# **Equations of Motion of the Beam of Electrons in RF-gun**

It has been shown elsewhere [19] that the beam velocity  $\vec{\beta}(z,t)$  and acceleration  $\vec{\eta}(z,t)$  are parallel to the accelerated field  $\vec{E}_0$  and independent of time. The beam velocity and longitudinal coordinates z are given by [19]:

$$\beta(z) = \frac{\sqrt{(1+Hz)^2 - 1}}{1+Hz} = \frac{dz}{c\,dt}$$
 (1)

The longitudinal coordinate of an electron at time t; z(t) is:

$$z(t) = \frac{1}{H} \left( \sqrt{1 + (Hc(t - t_z))^2} - 1 \right)$$
 (2)

Analysis of the Force Exerted on an Accelerated Beam of Electrons by Its Own Wakefield in the Laser-Driven Rf-gun

where  $t_z$  is the time at which element z of the beam leaves the photocathode and

$$H^{-1} = \frac{mc^2}{eE_0} \,. {3}$$

Here, m is the mass of the electron at rest, e is the electron charge,  $E_0$  is the amplitude of the accelerated field and c is the speed of light.

#### Theoretical Setup: Wakefield Maps

The wakefield components driven by an electron within the beam and the charge images on the cathode are reported elsewhere [24]. These components are obtained by a projection of Lienard-Wiechert fields on the axes illustrated in Fig. 2. As a result of cylindrical symmetry, the non-vanishing components of the electromagnetic fields are given by [24] as:

$$E_{z,\beta}(P,t|W) = \frac{e}{4\pi\varepsilon_0} \frac{\zeta' - z + \beta'\sqrt{s^2 + (\zeta' - z)^2}}{\gamma'^2(\sqrt{s^2 + (\zeta' - z)^2} + \beta'(\zeta' - z)^2)^3}$$
(4)

$$E_{z,\dot{\beta}}(P,t|W) = \frac{e}{4\pi \,\varepsilon_0 \,c} \frac{\dot{\beta}' \,s^2}{\left(\sqrt{s^2 + (\zeta' - z)^2} + \beta' \,(\zeta' - z)^2\right)^3} \tag{5}$$

$$E_{r,\beta}(P,t|W) = \frac{e}{4\pi\varepsilon_0} \frac{s\cos\theta}{\gamma'^2 \left(\sqrt{s^2 + (\zeta' - z)^2} + \beta' (\zeta' - z)^2\right)^3}$$
(6)

$$E_{r,\dot{\beta}}(P,t|W) = -\frac{e}{4\pi\,\varepsilon_0 c} \frac{\dot{\beta}'(\zeta'-z)s\cos\theta}{(\sqrt{s^2 + (\zeta'-z)^2} + \beta'(\zeta'-z)^2)^3} \tag{7}$$

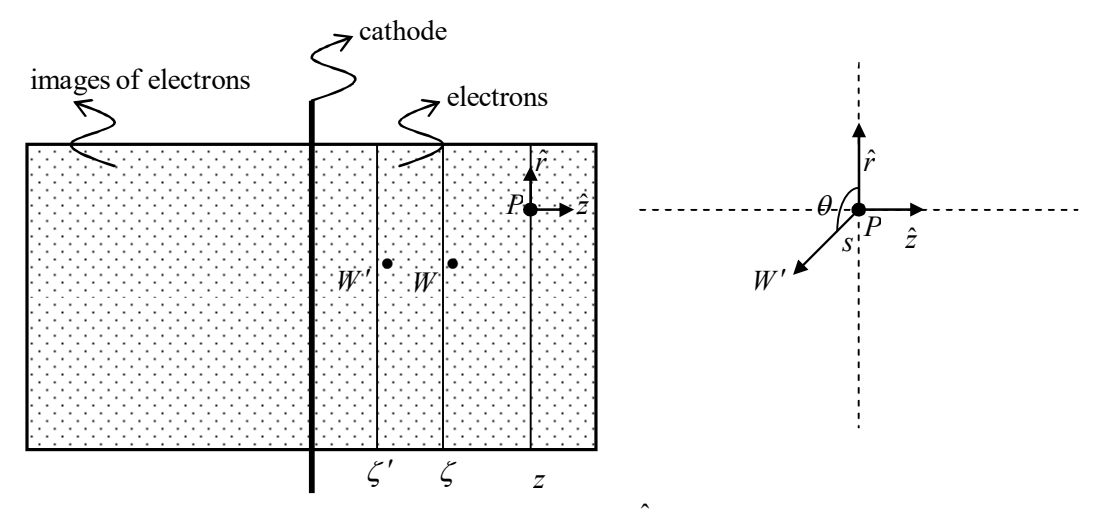


FIG. 2. Cylindrical coordinates s,  $\theta$  and z. The unit vectors  $\hat{r}$ ,  $\hat{\theta}$  and  $\hat{z}$  at point P in the direction of increasing s,  $\theta$  and z, respectively.

Here, 
$$\beta$$
 and  $\dot{\beta} = \frac{\partial \beta}{\partial t}$  exhibit the field

components' dependence on velocity and acceleration, respectively,  $\varepsilon_0$  is the permittivity of free space and the superscript (') denotes values taken at time t'. The electromagnetic fields generated at time t and point P, by an electron moving on a specified trajectory,

depends on the retarded position  $\overrightarrow{W}(t')$  of the electron at time t'. On the other hand, the image of charges on the cathode was obtained by [24] by using a set of symmetric charges +e at each instant t with respect to the cathode. The field component due to these images is then derived by replacing -e with e, e0 with e0 with e0 with e0 with e0 with e0 with e1 or e2 and with e3 and with e5 or e6 and with e6 or e7.

Article Ershaidat and Salah

#### Formulation of Global Fields

The global field is the sum of the fields due to in the cathode. The non-vanishing components the space charge and due to the image of charges of the field are given by [24] as:

$$E_{z}(P,t) = \frac{e}{4\pi \,\varepsilon_{0}} \int_{D(P,\zeta,t)} \frac{J}{e\beta \,c} \left( \frac{\zeta' - z + \beta' \sqrt{s^{2} + (\zeta' - z)^{2}}}{\gamma'^{2} (\sqrt{s^{2} + (\zeta' - z)^{2}} + \beta' (\zeta' - z))^{3}} \right) + \frac{e}{4\pi \,\varepsilon_{0}} + \frac{e}{4\pi \,\varepsilon_{0}} \int_{D(P,\zeta,t)} \frac{J}{e\beta \,c} \left( \frac{\zeta' - z + \beta' \sqrt{s^{2} + (\zeta' - z)^{2}}}{\gamma'^{2} (\sqrt{s^{2} + (\zeta' - z)^{2}} + \beta' (\zeta' - z))^{3}} \right) + \frac{e}{4\pi \,\varepsilon_{0}} \int_{D(P,\zeta,t)} \frac{J}{e\beta \,c} \left( \frac{\zeta' - z + \beta' \sqrt{s^{2} + (\zeta' - z)^{2}}}{\gamma'^{2} (\sqrt{s^{2} + (\zeta' - z)^{2}} + \beta' (\zeta' - z))^{3}} \right) + \frac{e}{4\pi \,\varepsilon_{0}} \int_{D(P,\zeta,t)} \frac{J}{e\beta \,c} \left( \frac{\zeta' - z + \beta' \sqrt{s^{2} + (\zeta' - z)^{2}}}{\gamma'^{2} (\sqrt{s^{2} + (\zeta' - z)^{2}} + \beta' (\zeta' - z))^{3}} \right) + \frac{e}{4\pi \,\varepsilon_{0}} \int_{D(P,\zeta,t)} \frac{J}{e\beta \,c} \left( \frac{\zeta' - z + \beta' \sqrt{s^{2} + (\zeta' - z)^{2}}}{\gamma'^{2} (\sqrt{s^{2} + (\zeta' - z)^{2}} + \beta' (\zeta' - z))^{3}} \right) + \frac{e}{4\pi \,\varepsilon_{0}} \int_{D(P,\zeta,t)} \frac{J}{e\beta \,c} \left( \frac{\zeta' - z + \beta' \sqrt{s^{2} + (\zeta' - z)^{2}}}{\gamma'^{2} (\sqrt{s^{2} + (\zeta' - z)^{2}} + \beta' (\zeta' - z))^{3}} \right) + \frac{e}{4\pi \,\varepsilon_{0}} \int_{D(P,\zeta,t)} \frac{J}{e\beta \,c} \left( \frac{\zeta' - z + \beta' \sqrt{s^{2} + (\zeta' - z)^{2}}}{\gamma'^{2} (\sqrt{s^{2} + (\zeta' - z)^{2}} + \beta' (\zeta' - z))^{3}} \right) + \frac{e}{4\pi \,\varepsilon_{0}} \int_{D(P,\zeta,t)} \frac{J}{e\beta \,c} \left( \frac{\zeta' - z + \beta' \sqrt{s^{2} + (\zeta' - z)^{2}}}{\gamma'^{2} (\sqrt{s^{2} + (\zeta' - z)^{2}} + \beta' (\zeta' - z))^{3}} \right) + \frac{e}{4\pi \,\varepsilon_{0}} \int_{D(P,\zeta,t)} \frac{J}{e\beta \,c} \left( \frac{\zeta' - z + \beta' \sqrt{s^{2} + (\zeta' - z)^{2}}}{\gamma'^{2} (\sqrt{s^{2} + (\zeta' - z)^{2}} + \beta' (\zeta' - z)^{2}} \right) + \frac{e}{4\pi \,\varepsilon_{0}} \int_{D(P,\zeta,t)} \frac{J}{e\beta \,c} \left( \frac{\zeta' - z + \beta' \sqrt{s^{2} + (\zeta' - z)^{2}}}{\gamma'^{2} (\sqrt{s^{2} + (\zeta' - z)^{2}} + \beta' (\zeta' - z)^{2}} \right) + \frac{e}{4\pi \,\varepsilon_{0}} \int_{D(P,\zeta,t)} \frac{J}{e\beta \,c} \left( \frac{\zeta' - z + \beta' \sqrt{s^{2} + (\zeta' - z)^{2}}}{\gamma'^{2} (\sqrt{s^{2} + (\zeta' - z)^{2}} + \beta' (\zeta' - z)^{2}} \right) + \frac{e}{4\pi \,\varepsilon_{0}} \int_{D(P,\zeta,t)} \frac{J}{e\beta \,c} \left( \frac{\zeta' - z + \beta' \sqrt{s^{2} + (\zeta' - z)^{2}}}{\gamma'^{2} (\sqrt{s^{2} + (\zeta' - z)^{2}} + \beta' (\zeta' - z)^{2}} \right) + \frac{e}{4\pi \,\varepsilon_{0}} \int_{D(P,\zeta,t)} \frac{J}{e\beta \,c} \left( \frac{\zeta' - z + \beta' \sqrt{s^{2} + (\zeta' - z)^{2}}} \right) + \frac{e}{4\pi \,\varepsilon_{0}} \int_{D(P,\zeta,t)} \frac{J}{e\beta \,c} \left( \frac{\zeta' - z + \beta' \sqrt{s^{2} + (\zeta' - z)^{2}}} \right) + \frac{e}{4\pi \,\varepsilon_{0}} \int_{D(P,\zeta,t)} \frac{J}{e\beta \,c} \left( \frac{\zeta' - z + \beta' \sqrt{s^{2} + (\zeta' - z)^{2}} \right) + \frac{e}{4\pi \,\varepsilon_{0}} \int_{D(P,\zeta,t)} \frac{J}{e\beta \,c} \left( \frac{\zeta' - z + \beta' \sqrt{s^{2} + (\zeta' -$$

$$\frac{\dot{\beta}' \, s^2}{c \, (\sqrt{s^2 + (\zeta' - z)^2} + \beta' (\zeta' - z))^3}) \, \times \, \frac{\beta}{\beta'} \, (1 - \frac{\beta' (z - \zeta')}{\sqrt{s^2 + (z - \zeta')^2}}) \, s \, ds \, d\theta \, d\zeta' +$$

$$\frac{-e}{4\pi\,\varepsilon_0}\int\limits_{\overline{D}(P,\zeta,t)}\frac{J}{-e\,\overline{\beta}\,c}\left(\frac{\overline{\zeta}'-z+\overline{\beta}'\,\sqrt{s^2+(\overline{\zeta}'-z)^2}}{\gamma'^2\left(\sqrt{s^2+(\overline{\zeta}'-z)^2}+\overline{\beta}'(\overline{\zeta}'-z)\right)^3}+\right.$$

$$\frac{\dot{\overline{\beta}'} s^2}{c \left(\sqrt{s^2 + (\overline{\zeta}' - z)^2} + \overline{\beta}' (\overline{\zeta}' - z)\right)^3}\right) \times \frac{\overline{\beta}}{\overline{\beta}'} \left(1 - \frac{\overline{\beta}' (z - \zeta')}{\sqrt{s^2 + (z - \overline{\zeta}')^2}}\right) s \, ds \, d\theta \, d\overline{\zeta}'$$
(8)

The transverse  $E_r$  and the azimuthal  $B_{ heta}$  components are effortlessly obtained by [24] as:

$$E_{r}(P,t) = \frac{1}{4\pi \,\varepsilon_{0} \,c} \,\left( \int_{D(P,\zeta,t)} J\left( \frac{s^{2}}{\beta' \gamma'^{2} \left(\sqrt{s^{2} + (z - \overline{\zeta}')^{2}} \left(\sqrt{s^{2} + (\zeta' - z)^{2}} + \beta'(\zeta' - z)\right)^{2}} + \beta'(\zeta' - z)\right)^{2} \right)$$

$$+ \frac{s \dot{\beta}' (\zeta'-z)}{\beta' c \sqrt{s^2 + (z-\overline{\zeta}')^2} (\sqrt{s^2 + (\zeta'-z)^2} + \beta' (\zeta'-z))^2}) \cos\theta \ ds \ d\theta \ d\zeta' +$$

$$\int_{\overline{D}(P,\zeta,t)} J\left(\frac{s^2}{\overline{\beta'\gamma'^2}\left(\sqrt{s^2+(z-\overline{\zeta'})^2}\left(\sqrt{s^2+(\overline{\zeta'}-z)^2}+\overline{\beta'}(\overline{\zeta'}-z)\right)^2}\right.\right. +$$

$$\frac{s \, \overline{\beta} \, (\overline{\zeta}' - z)}{\overline{\beta}' c \, \sqrt{s^2 + (z - \overline{\zeta}')^2} \, (\sqrt{s^2 + (\overline{\zeta}' - z)^2} + \overline{\beta}' (\overline{\zeta}' - z))^2} \,) \cos \theta \, s \, ds \, d\theta \, d\overline{\zeta}')$$
(9)

Analysis of the Force Exerted on an Accelerated Beam of Electrons by Its Own Wakefield in the Laser-Driven Rf-gun

$$B_{\theta}(P,t) = \frac{1}{4\pi \,\varepsilon_{0} \,c^{2}} \,\left( \int_{D(P,\zeta,t)} J\left( \frac{s^{2}}{\gamma'^{2} \,\sqrt{s^{2} + (z - \overline{\zeta}')^{2}} \,\left(\sqrt{s^{2} + (\zeta' - z^{2})^{2}} + \beta'(\zeta' - z)\right)^{2}} \right) \,dz$$

$$+ \frac{s^2 \dot{\beta}'}{\beta' c \left(\sqrt{s^2 + (\zeta' - z)^2} + \beta' (\zeta' - z)\right)^2} \right) \cos \theta \ ds \ d\theta \ d\zeta' +$$

$$\int\limits_{\overline{D}(P,\zeta,t)} J\left(\frac{s^2}{\gamma'^2 \sqrt{s^2 + (z - \overline{\zeta}')^2}} \left(\sqrt{s^2 + (\overline{\zeta}' - z)^2} + \overline{\beta}'(\overline{\zeta}' - z)\right)^2\right. +$$

$$\frac{s^2 \, \dot{\overline{\beta}}}{\overline{\beta}' c \, \left(\sqrt{s^2 + (\overline{\zeta}' - z)^2} + \overline{\beta}' (\overline{\zeta}' - z)\right)^2}) \cos\theta \, s \, ds \, d\theta \, d\overline{\zeta}')$$
(10)

where  $D(P,\zeta,t)$  represents a disc located within the beam.

J(r,z,t) is the current density which is related to the charge density by:

$$\rho(r,z,t) = \frac{I \varpi(z,t)}{\pi a^2 \beta(z) c} [1 - \Theta(r-a)]$$

$$\vec{J}(r,z,t) = \beta(z) c \rho(r,z,t) \vec{u}_z$$
(11)

Here,  $\beta(z) = v(z)/c$  denotes the time-independent velocity, I is the total current whose axial profile  $\varpi(z, t)$  is uniform and  $\Theta(r-a)$  is the Heaviside step function.

$$t = \frac{1}{c} \sqrt{\zeta \left(\zeta + \frac{2}{H}\right)} \tag{12}$$

$$t' = t - \frac{WP}{c} = t - \frac{1}{c} \sqrt{s^2 + (z - \zeta)^2}$$
 (13)

All the distances *s* must satisfy the following inequality:

$$s \le s_{\text{max}} = \sqrt{\left(ct - \sqrt{\zeta\left(\zeta + \frac{2}{H}\right)}\right)^2 - \left(\zeta - z\right)^2}$$
 beam with cylindrical symmetric total length  $Z_H - Z_B$  is:
$$d\vec{F} = dq \left(E_z \hat{z} + E_r \hat{r}\right)$$

with

$$\zeta \le \frac{(ct+z)^2}{2(H^{-1}+z+ct)} = \zeta_{\text{max}} \le z_H$$
(15)

where  $z_H$  is the longitudinal coordinates of the beam head.

Here, couples  $(s, \overline{\zeta})$  represent a subset of points in the space of images. An electromagnetic signal is emitted at time t' and arrives to point P at time t. At this time t, all electrons own a longitudinal coordinate within  $z_H$ . To that end, we must have  $\zeta_{\max} \leq z_H$  and  $s_{\max}$  does not exist unless  $\zeta \leq \zeta_{\max}$  as well as

$$\overline{\zeta} \le -\frac{(ct-z)^2}{2(ct+H^{-1}-z)} = \overline{\zeta}_{\text{max}}$$
 (16)

#### The Short-Range Wakefield Force Exerted on the Beam

The electromagnetic fields  $\vec{E}$  and  $\vec{B}$  induced by the beam are known as short-range wakefields. These fields act back on the beam and influence its motion. The Lorentz force acting on an amount of charge dq within the beam with cylindrical symmetry of radius a and total length  $Z_H - Z_B$  is:

$$d\vec{F} = dq \left( E_z \, \hat{z} + E_r \, \hat{r} \right) + dq \, \beta c \, \hat{z} \times B \, \hat{\theta}$$
(17)

where  $Z_H$  and  $Z_B$  are the longitudinal coordinates of the beam head and tail, respectively.

Article Ershaidat and Salah

Given that:

$$dq = \rho(r, z, t) \, dV \tag{18}$$

Then, equation (17) becomes

$$d\vec{F} = \rho(r, z, t) [E_z \,\hat{z} + (E_r - \beta c \, B_\theta) \hat{r} \,] dV$$
(19)

Here, dV is the element of volume in cylindrical coordinates.

#### **Numerical Results and Discussion.**

Mathematica® is used in order to calculate the components of the force on the beam at different stages of the photo-emission of the beam from the cathode.

For numerical calculation of the wakefield forces, the following parameters, which are also harmonious with the "ELSA" facility, are adopted: I=100 A, electron beam cross-sectional area  $\pi a^2=1$  cm<sup>2</sup> (a is the radius of the beam), beam time length  $\tau=100$  ps and the accelerated field  $E_0=30$  MV/m. These forces will be displayed as a function of the longitudinal reduced coordinates Z=Hz, A=Ha, R=Hr and  $T=Hc\tau$  based on the characteristic length  $H^{-1}$  (Eq. 3).

#### Wakefield and Wakefield Force at Different Emission Times

Figs. 3 and 4 display the longitudinal and transverse force acting on the beam, while Fig. 5 displays the total force acting on the beam at time  $T = 2Hc\tau/5$ . Figs. 6, 7 and 8 repeat Figs. 3, 4 and 5, but at time  $T = Hc\tau$  (at the end of the photoemission). Figs. 3 and 6 indicate that the beam is found to be attracted towards the cathode by the positive field due to the images of charge on the cathode. This attractive force varies along the beam length; it is strongest on the drive electrons and decreasing as one moves from the beam head towards the trailing electrons. Figs. 4 and 7 show the salient features of the radial force on the entire beam. Briefly, the beam is defocusing towards the negative radial direction and the defocusing of the trailing electrons is less than that of driving ones. The transverse forces on the different slices of the beam along the beam lead to an augmentation in the transverse momentum of the beam. This augmentation is incoherent from the beam tail to the beam head. Consequently, the transverse phase space of the beam will be distorted and this distortion may alleviate the growth of the beam instability and brightness.

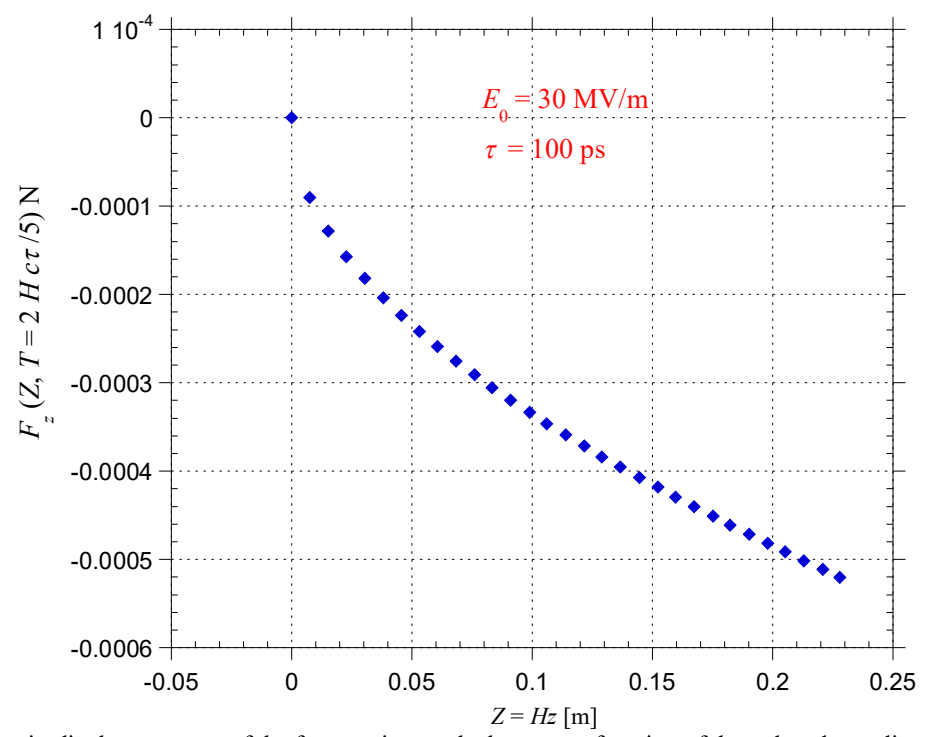


FIG. 3. Longitudinal component of the force acting on the beam as a function of the reduced coordinates Z along the axis of the RF-gun at time  $T = 2Hc\tau/5$ .

Analysis of the Force Exerted on an Accelerated Beam of Electrons by Its Own Wakefield in the Laser-Driven Rf-gun

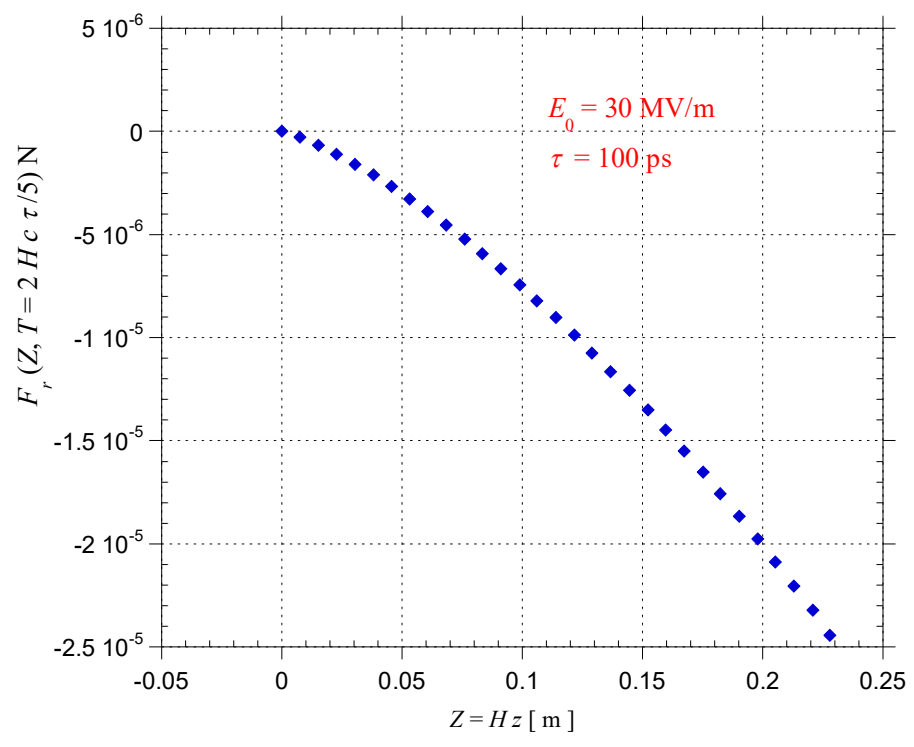


FIG. 4. Transverse component of the force acting on the beam as a function of the reduced coordinates Z along the axis of the RF-gun at time  $T=2Hc\tau/5$ .

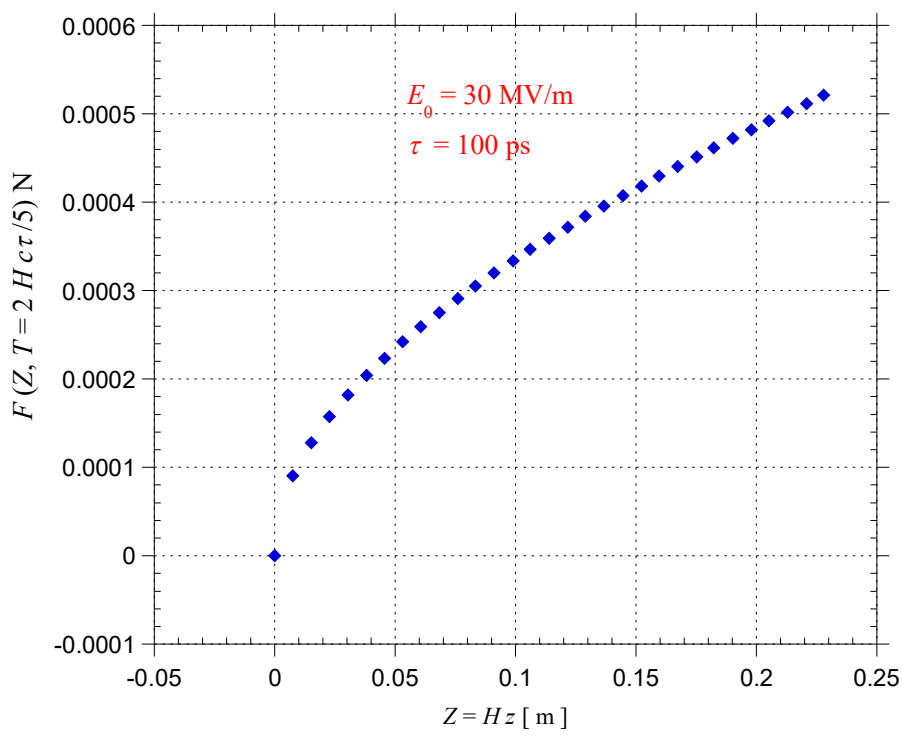


FIG. 5. Total force acting on the beam as a function of the reduced coordinates Z along the axis of the RF-gun at time  $T=2Hc\tau/5$ .

Article Ershaidat and Salah

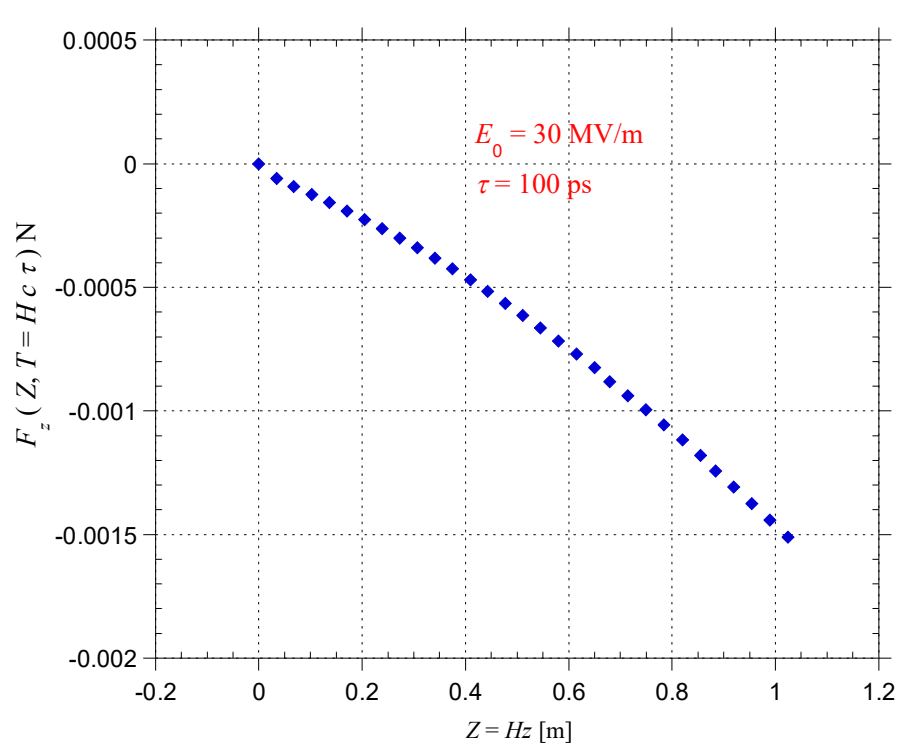


FIG. 6. Longitudinal component of the force acting on the beam as a function of the reduced coordinates Z along the axis of the RF-gun at the end of photoemission (at time  $T = Hc\tau$ ).

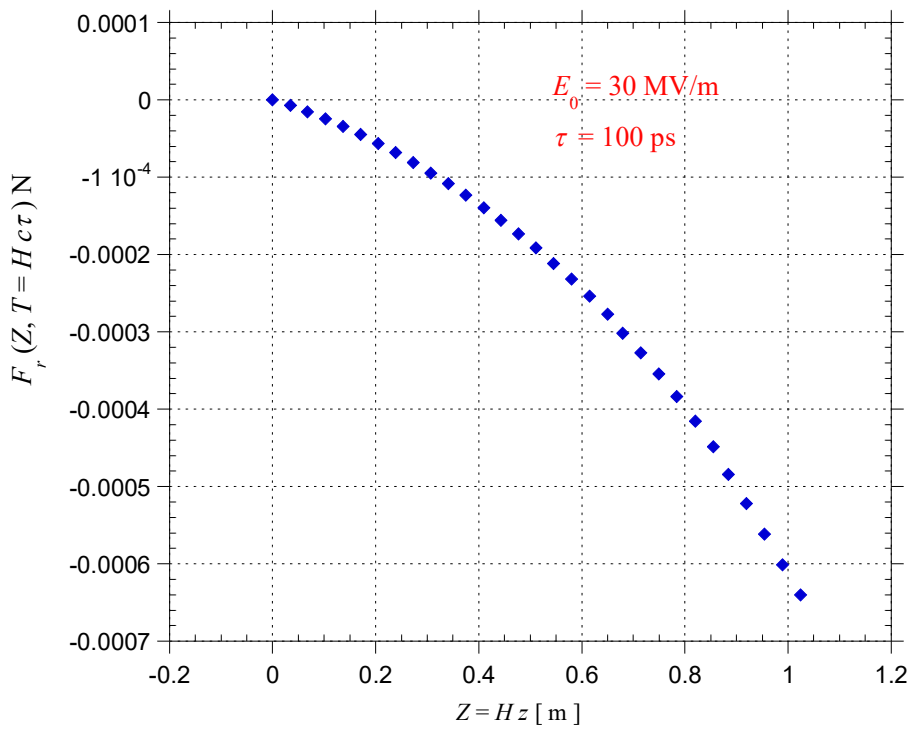


FIG. 7. Transverse component of the force acting on the beam as a function of the reduced coordinates Z along the axis of the RF-gun at the end of photoemission (at time  $T = Hc\tau$ ).

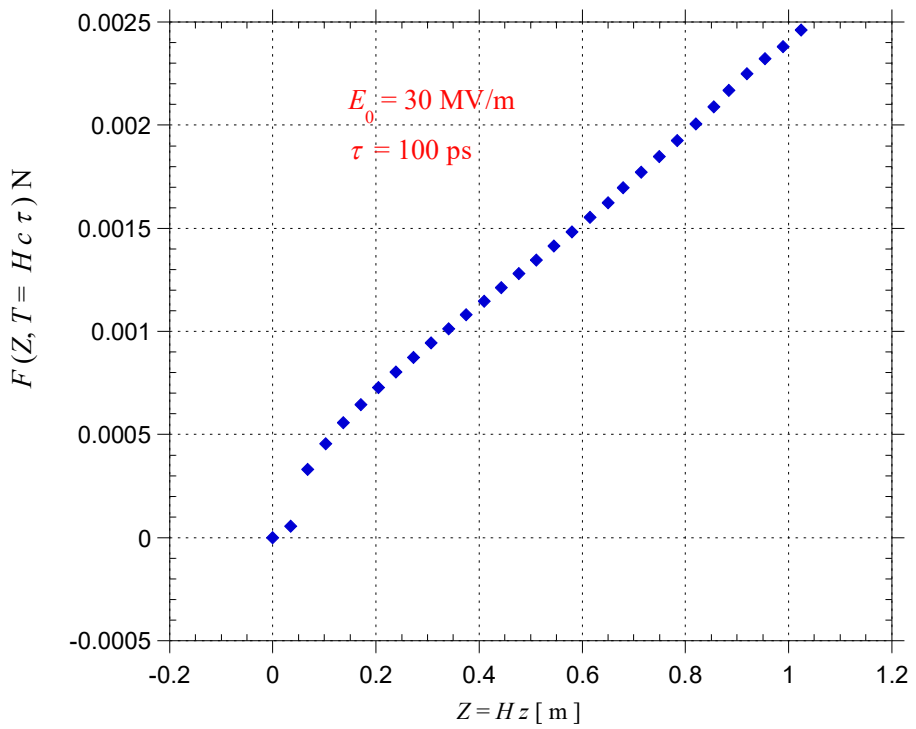


FIG. 8. The magnitude of the total force acting on the beam as a function of the reduced coordinates Z along the axis of the RF-gun at the end of photoemission (at time  $T = Hc\tau$ ).

All of these figures and Equation (19) reveal two effects on the beam: the first one, due to the longitudinal component of the force, affecting the trailing electrons in the beam, changes the energy of individual electrons in the beam, depending on their position. Consequently, the short-range wakefield induces energy spread in the beam.

The second effect, due to the transverse component of the force, deflects the beam trajectory. The electrons within the beam are decelerated by the positive charge image field. Consequently, these electrons lose more energy than those situated at the beam head. The negative transverse force illustrated in Figs. 4 and 7 means that this force is defocusing. The electrons within the beam experience over the beam length an average deflecting force that is proportional to the radial displacement r (0 < r < a) and dependent on the distance z. Figs. 3 to 8 show that the short-range space charge forces move together with the beam. They are not constant along the RF-cavity. Therefore, in a single bunch beam, the transverse wake forces from the bunch head deflect the tail of the beam; this deflection works towards distorting the beam into a banana-like shape in the initial stage of the acceleration and a spherical one at the exit aperture of the RF- cavity.

#### Conclusion

We have shown that it is possible to investigate numerically the force acting on an accelerated electron beam in the initial stage of acceleration, during the photoemission of the electrons from the cathode. The formula of the Lorentz force is expressed as an integral form of the components of the wakefield over the entire beam volume.

The components of wakefield generated by an accelerated electron beam that has just been emitted from the cathode in a "Pill-Box" cavity are derived from the Lienard-Wiechert potential and the method of images during the photoemission of the electron beam from the cathode [24].

Numerical calculations of the beam wakefield forces revealed two major effects on the beam: the first one is ascribed to the longitudinal component of the force, which affects the trailing electrons in the beam and changes the energy of the individual electrons, depending on their position. As a result, the short-range longitudinal component of the wakefield force will give rise to energy spread in the beam.

Article Ershaidat and Salah

The second effect, due to the transverse component of the force, deflects the beam trajectory. The electrons within the beam experience over the beam length an average deflecting force that is proportional to the radial displacement r (0 < r < a) and dependent on the distance z. This deflection might lead to the tilting of the tail of the beam into a nearly "banana" shape in the initial stage of the acceleration and a spherical one at the exit of the RF-gun. Particle loss will occur when the tilted

beam hits the cavity's lateral wall. This would be the cause of the beam breakup.

Since the forces that onset the electrons beam emanate from the beam itself, our numerical results and discussion of these forces represent a significant step towards an advanced understanding of wakefield accelerator technology [27-29]. These results could be an important background reference for the experimental layout and design of laser-driven plasma wakefield accelerators [30].

#### References

- [1] Madey, J.M., J. Appl. Phys., 42(5) (1971) 1906.
- [2] Deacon, D. et al., Phys. Rev. Lett., 38 (1977) 892.
- [3] Carlsten, B.E. et al., J. Phys. B: At. Mol. Opt. Phys., 47 (2014) 234012.
- [4] Hartemann, F.V. et al., Rev. Spec. Top. Accel. Beams, 8 (2005) 100702.
- [5] Hartemann, F.V. et al., Laser Part. Beams, 22 (2004) 221.
- [6] Di Mitri, S. and Cornacchia, M., Phys. Rep., 539 (2014) 1.
- [7] Di Mitri, S., Photonics, 2 (2015) 317.
- [8] Schaer, M. et al., Phys. Rev. Accel. Beams, 9 (2016) 072001.
- [9] Kikuchi, T. et al., Phys. Rev. Accel. Beams, 19 (2016) 06420.
- [10] Davidson, R.C. and Qin, H., "Physics of Intense Charged Particle Beams in High-Energy Accelerators", (Imperial College Press, Singapore, 2001).
- [11] Wangler, T.P., "RF Linear Accelerators", (Wiley-VCH, New York, 2008).
- [12] Reiser, M., "Theory and Design of Charged Particle Beams", (Wiley, New York, 1994).
- [13] Reiser, M., J. Appl. Phys., 70 (1991) 1919.
- [14] Kapchinskij, J.M. and Ladimirskij, V.V., Proc. International Conference on High Energy Accelerators, (CERN 274, 1959).
- [15] Fraser, J.S. et al., Particle Accelerator Conference PAC85, 1791 (1985).

- [16] CST GmbH, Bad Nauheimer Strasse 19, D-64289, Darmstadt, Germany.
- [17] Floettmann, K., ASTRA User Manual, www.desy.de/~mpyflo/Astra\_dokumentation. Accessed on Sep. 09, 2017.
- [18] Nogales, J. et al., Radio Sci., 47 (2012) RS5006.
- [19] Salah, W. and Dolique, J-M., Nucl. Inst. and Meth. A, 431 (1999) 27.
- [20] Salah, W. et al., Nucl. Inst. and Meth. A, 564(1) (2006) 66.
- [21] Salah, W. and Dolique, J-M., Nucl. Inst. and Meth. A, 447 (2000) 309.
- [22] Salah, W. and Hallak, A.B., J. Phys. D, Applied Physics, 38 (2005) 2292.
- [23] Salah, W., Nucl. Inst. and Meth. A, 480 (2002) 398.
- [24] Salah, W. et al., Nucl. Inst. and Meth. A, 607 (2009) 498.
- [25] Kim, K.-J. et al., J. Appl. Phys., 68 (1990) 4942.
- [26] Figuera, H. et al., Phys. Rev. Lett., 60 (1988) 2144.
- [27] Adli, E. et al., New J. Phys., 18 (2016) 103013.
- [28] Floettmann, K., Phys. Rev. Spec. Top. Accel. Beams, 18 (2015) 064801.
- [29] Guillaume, E. et al., Phys. Rev. Lett., 115 (2015) 155002.
- [30] Litos, M. et al., Nature, 515 (2014) 92.

### Jordan Journal of Physics

#### Communication

# Synthesis and Characterization of Monovalent, Divalent and Trivalent Cation Doping of Cu<sub>2</sub>Se Thin Films Using Chemical Bath Deposition Method\*

### A. P. Sudha<sup>a</sup>, J. Henry<sup>b</sup>, K. Mohanraj<sup>b</sup> and G. Sivakumar<sup>c</sup>

<sup>a</sup> Department of Physics, Vellalar College for Women (Autonomous), Thindal, Erode 638 012, India.

Received on: 22/5/2017; Accepted on: 5/11/2017

**Abstract:** In this work, pure and Bi<sup>3+</sup>, Cd<sup>2+</sup>, Na<sup>+</sup> - doped Cu<sub>2</sub>Se thin films were prepared by chemical bath deposition (CBD) method. The effect of doping on optostructural properties was analyzed. XRD patterns show the cubic phase for pure and Bi<sup>3+</sup>, Cd<sup>2+</sup>, Na<sup>+</sup> - doped Cu<sub>2</sub>Se thin films. The doped films show higher absorption than Cu<sub>2</sub>Se in the visible region. The band gap energies of the films were found to be 1.75 eV, 1.70 eV, 3.66 eV, 2.55 eV for pure and Bi<sup>3+</sup>, Cd<sup>2+</sup>, Na<sup>+</sup> - doped Cu<sub>2</sub>Se thin films, respectively.

**Keywords:** Cu<sub>2</sub>Se thin films, Cation doping, chemical bath deposition (CBD), XRD.

#### Introduction

Copper selenide is a p-type semi-conductor which is a cost-effective heterojunction solar cell used in solar energy conversion devices with high efficiency [1, 2]. Intensive research has been performed in fabrication and characterization of copper selenide in the form of thin films because of its band gap energy (1.2) eV - 2.3 eV), high optical absorption coefficient, low toxicity and relative abundance [3]. Pathan et al. [4] have reported a band gap energy of 2.35 eV for Cu<sub>2</sub>Se thin films. However, the bandgap is greater than the optimum value of solar cells. Hence, it is necessary to enhance the optical properties of the films to use them as a high-efficiency absorbing material.

Doping is the suitable way to tune the optical band gap, because incorporation of foreign atoms in parent material produces discrete energy levels in the intrinsic quantum energy levels, which in turn enhances the optical, electronic and magnetic properties of the host semi-conductor. These properties of a semiconductor could be modified by doping with divalent and trivalent metal cations due to the fact that they provide extra electrons, which enhances or modifies the properties [5]. Recently, trivalent Bi<sup>3+</sup> - doped SnS thin films showed the lowest resistivity of 4.788 x 10<sup>-1</sup>  $\Omega$ cm [6]. Luo et al. reported that the addition of Bi<sup>3+</sup> trivalent ions into  $Mg_2Si_{0:8}Sn_{0:2}$ significantly decreases thermal conductivity and increases electrical conductivity and the Seebeck coefficient [7]. Patel et al. stated that Mn-doped CdS nanoparticles can be used for application in dilute magnetic semi-conductors and fabrication of solar cells [8]. Kumar et al. [9] have reported that the optical band gap energy was decreased for divalent Cd<sup>2+</sup> - doped ZnO thin films. Mondal and Mitra (2011) reported that divalent Cd2+ doping in ZnO decreases the optical bandgap [10]. Bera and Saha reported higher efficiency for divalent Zn<sup>2+</sup> - doped dye sensitized solar cells [11]. Ali et al. [12] reported high refractive index for Ag<sup>+</sup> - doped ZnO films. Kumar and Thangavel reported that monovalent Na<sup>+</sup> doping has modified the band gap ZnO thin films [13]. From the literature, it is found that the doping of

Corresponding Author: K. Mohanraj

Email: kmohanraj.msu@gmail.com; mohanraj@msuniv.ac.in

b Department of Physics, Manonmaniam Sundaranar University, Tirunelveli 627 012, Tamilnadu, India.

<sup>&</sup>lt;sup>c</sup> Centralized Instrumentation and Service Laboratory, Department of Physics, Annamalai University, Annamalai Nagar, Chidambaram, Tamilnadu 608 002, India.

<sup>\*&</sup>quot;6<sup>th</sup> National Seminar on Advances in Materials Science NSAMS-2017, held on March 2, 3-2017 at the Department of Physics, Manonmaniam Sundaranar University, Tirunelveli-627 012, Tamilnadu, India".

Communication Sudha et al.

monovalent, divalent and trivalent cations modifies the optical and electrical properties of semi-conductor materials. Hence, the objective of this work is to prepare monovalent (Na<sup>+</sup>), divalent (Cd<sup>2+</sup>) and trivalent (Bi<sup>3+</sup>) ion-doped Cu<sub>2</sub>Se thin films by CBD method to study their optical properties

#### **Experimental Procedure**

Pure and Bi3+, Cd2+, Na+ - doped Cu2Se thin films were prepared by chemical bath deposition method. The following A.R. grade chemicals were used: copper chloride  $(CuCl_2.5H_2O)$ , bismuth nitrate (Bi(NO<sub>3</sub>)<sub>3</sub>.5H<sub>2</sub>O), cadmium chloride (CdCl<sub>2</sub>.5H<sub>2</sub>O), selenium (Se), sodium sulphite (Na<sub>2</sub>SO<sub>3.5</sub>H<sub>2</sub>O), acetone, HCl, ammonia, glass substrates and distilled water. The substrate cleaning was performed by immersion in chromic acid. Then, the substrates were washed with double distilled water and immersed in HCl solution for etching process for 15 min. The washed substrates were immersed in a 2proponal solution, then the solution was placed in an ultrasonic bath for 15 min. The ultrasonic bath gives the scrubbing effect on the substrates and removes dust particles from the substrates. Finally, the substrates were washed with double distilled water and cleaned with acetone. Then, they were used for thin film deposition.

Sodium selenosulphate (Na<sub>2</sub>SeSO<sub>3</sub>) was prepared by refluxing of 0.1 M of selenium and 0.25 M sodium sulphite dissolved in 400 ml distilled water at 70°C for 6 hrs. After refluxing, the collected sodium selenosulphate solution was cooled to room temperature. Then, it was filtered and used for the deposition process.

0.1 M of CuCl<sub>2</sub>.5H<sub>2</sub>O was dissolved in 40 ml distilled water. Ammonia solution was added drop by drop into the copper solution under constant stirring. The color of the solution changed from light green to blue, which indicates the formation of Cu (OH)2, followed by  $[Cu (NH_3)_4]^{2+}$  complex. Further, the blue colour solution turns into deep blue while adding excess ammonia into the solution. Finally, an amount of 40 ml of freshly prepared sodium selenosulphate (Na<sub>2</sub>SeSO<sub>3</sub>) solution was slowly added to the Cu complex solution. The colour of the solution again changed to dark green and then to brown, which indicates the of Cu<sub>2</sub>Se. The pre-cleaned microscope glass substrates (75mm x 25mm) were vertically immersed in the solution and

deposition was carried out at 70°C for 2 h. The Bi<sup>3+</sup>, Cd<sup>2+</sup>, Na<sup>+</sup> - doped Cu<sub>2</sub>Se thin films were deposited by adding Bi(NO<sub>3</sub>)<sub>3</sub>, CdCl<sub>2</sub>.5H<sub>2</sub>O and Na<sub>2</sub>SO<sub>3</sub>.5H<sub>2</sub>O into the CuCl<sub>2</sub> solution, respectively. Afterwards, the substrates were removed from the bath solution and washed several times using distilled water. The deposited films were annealed at 200 °C for 2 h for further characterization.

The prepared pure and doped films were characterized using XRD, FESEM and DRS techniques. X-ray diffraction (XRD) patterns were obtained using a PANalytical X` PERT-PRO diffractometer using Cu K $\alpha$  radiation ( $\lambda$  = 1.5460 Å). The diffraction patterns were collected in the range of  $2\theta$  =  $10^{\circ}$ – $80^{\circ}$ . To investigate the surface morphology and roughness of the particles, Field Emission Scanning Electron Microscopy (FESEM) was carried out using FEI - QUANTA–FEG 250. Diffuse Reflection Spectroscopy (DRS) spectra were recorded using a UV- 400 PC series UV-visible spectrometer.

#### **Results and Discussion**

Fig. 1 shows the XRD patterns of pure and Bi<sup>3+</sup>, Cd<sup>2+</sup>, Na<sup>+</sup> - doped Cu<sub>2</sub>Se thin films. In the diffraction patterns, the polycrystalline peaks seen at  $2\theta = 26.77^{\circ}$  (111), 44.41° (220), 52.60° (311),  $64.97^{\circ}$  (400),  $71.66^{\circ}$  (331),  $81.78^{\circ}$  (422)and 98.87° (440) belong to the cubic structure of Cu<sub>2</sub>Se and are in good agreement with the standard JCPDS card no. 65-2982. It is also noticed that no extra peaks were observed for the substitution of Bi<sup>3+</sup>, Cd<sup>2+</sup> - doped Cu<sub>2</sub>Se thin films, indicating that the films were in single cubic phase, whereas additional peaks were observed for Na<sup>+</sup> - doped Cu<sub>2</sub>Se thin films. The intensity of the primary (220) peak was suppressed and shifted toward lower angle due to doping; hence, the crystallinity of the films was deteriorated (Fig 2). The (220) plane is shifted towards the lower angle for Bi<sup>3+</sup>, Cd<sup>2+</sup>, Na<sup>+</sup> - doped Cu<sub>2</sub>Se thin films (Fig. 2). The shift is due to the higher ionic radii of  $Bi^{3+}$  (1.17 Å),  $Cd^{2+}$  (1.09 Å) and Na<sup>+</sup> (1.16 Å) than that of  $Cu^{+}$ (0.91 Å). The crystalline size of doped films was slightly reduced in comparison to the pure Cu<sub>2</sub>Se thin films (Table 1). A similar result (peak shift) was observed by Peng et al. [14] for Zn, Mn, Ni, Fe, In and Sm-doped β-Cu<sub>2</sub>Se. These results confirm the incorporation of Bi<sup>3+</sup>, Cd<sup>2+</sup> and Na<sup>+</sup> ions in the cubic structure of Cu<sub>2</sub>Se.

TABLE 1. Crystalline parameter of pure and Bi<sup>3+</sup>, Cd<sup>2+</sup>, Na<sup>+</sup> doped Cu<sub>2</sub>Se thin films.

···	Tire Personalization	or pont onn	, ,	uropeu cuza	• •••••	
S.No.	Sample	D (nm)	$\delta$ (lines/m <sup>2</sup> )	ε	a (Å)	$V (A)^3$
1	Cu <sub>2</sub> Se	84.18	$1.411 \times 10^{14}$	2.3 x 10 <sup>-3</sup>	5.73	188.12
2	Bi:Cu <sub>2</sub> Se	70.13	$2.033 \times 10^{14}$	$2.9 \times 10^{-3}$	5.746	189.71
3	Cd:Cu <sub>2</sub> Se	69	$2.06 \times 10^{14}$	$4.9 \times 10^{-3}$	5.768	191.90
4	Na:Cu <sub>2</sub> Se	81	$1.51 \times 10^{14}$	$3.4 \times 10^{-3}$	5.763	191.40

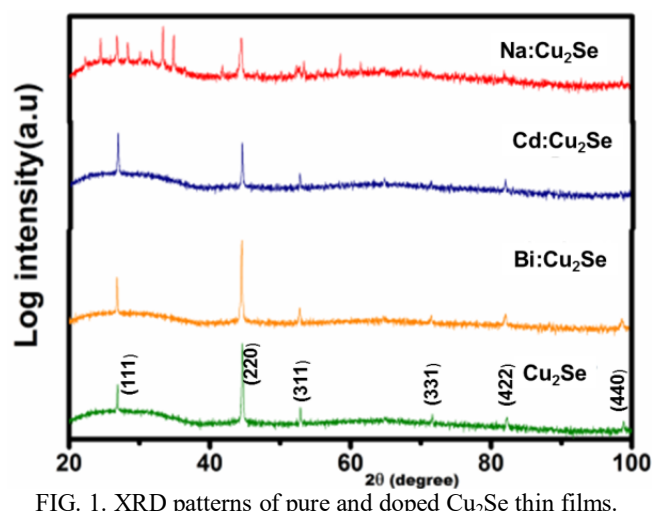


FIG. 1. XRD patterns of pure and doped Cu<sub>2</sub>Se thin films.

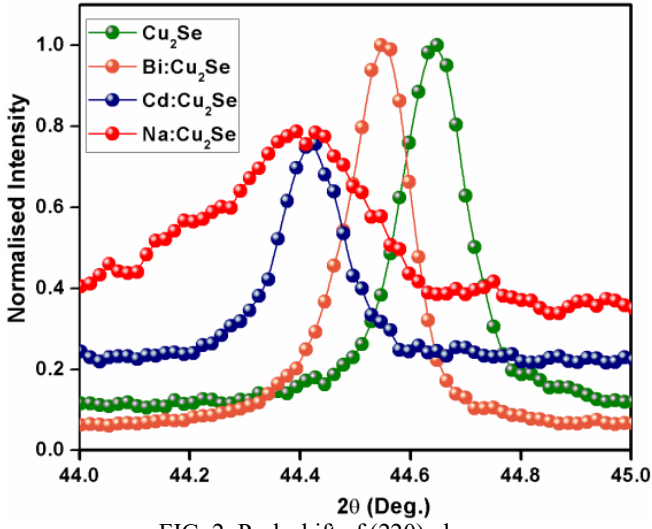


FIG. 2. Peak shift of (220) plane.

The crystalline size was estimated by using Scherrer formula [15]:

$$D = \frac{0.9 \,\lambda}{\beta \cos \theta} \tag{1}$$

where  $\beta$  is full width at half maximum (FWHM),  $\lambda$  is the wavelength of X-ray source and  $\theta$  is the Bragg's angle. Dislocation density (δ) was evaluated by the following formula [15] to

obtain information about the amount of defects in the films:

$$\delta = \frac{1}{D^2} \,. \tag{2}$$

The micro-strain can be calculated from the following relation [15]:

$$\varepsilon = \frac{\beta \cos \theta}{4} \,. \tag{3}$$

Communication Sudha et al.

The calculated values of crystalline size, dislocation density and microstrain were tabulated in Table 1. It is clear, from Table 1, that the crystalline size of Bi<sup>3+</sup>, Cd<sup>2+</sup>, Na<sup>+</sup> - doped Cu<sub>2</sub>Se is smaller than that of pure Cu<sub>2</sub>Se. This is attributed to the incorporation of foreign atoms in the parent network that alters the nucleation step during particle growth, limiting the nucleations, which consequently reduces the crystalline size. The dislocation density and stress are found to increase for doped samples. The result is evident for the substitution of Bi<sup>3+</sup>, Cd<sup>2+</sup>, Na<sup>+</sup> ions into the Cu sites. The lattice parameter a, and the cell volume were calculated

using the unit cell software (method of TJB Holland & SAT Redfern 1995). The calculated values are presented in Table 1. The lattice parameter, a is found to increase after doping, which confirms the incorporation of larger dopants into smaller Cu sites.

Fig. 3 shows the FESEM images of pure and Bi<sup>3+</sup>, Cd<sup>2+</sup>, Na<sup>+</sup> - doped Cu<sub>2</sub>Se films. The films show that the well defined, almost similar size particles, were uniformly distributed over the entire surface without any observable voids.

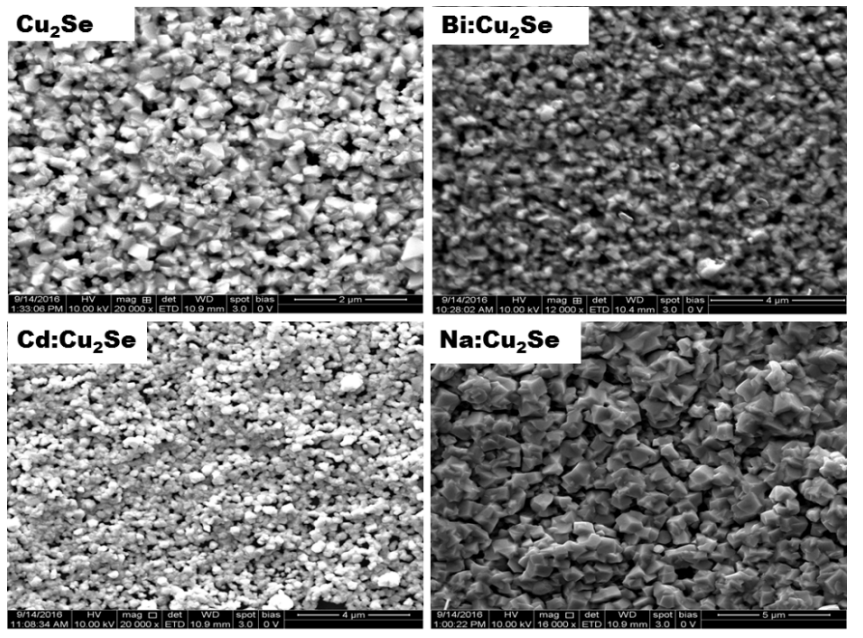


FIG. 3. FESEM images of pure and doped Cu<sub>2</sub>Se thin films.

Fig. 4 shows the DRS absorption spectra of pure and Bi<sup>3+</sup>, Cd<sup>2+</sup>, Na<sup>+</sup> - doped Cu<sub>2</sub>Se films. All films showed higher optical absorption than Cu<sub>2</sub>Se in the visible region. The increase in absorbance may be due to the overgrowth of particles on the film surface, which implies scattering losses as suggested by Saima Mushtaq *et al.* (2016) [16]. The calculated band gap values of Cu<sub>2</sub>Se and Bi, Cd, Na - doped Cu<sub>2</sub>Se films were found to be 1.75 eV,1.70eV,3.66 eV and 2.55 eV, respectively (Fig.5) It is obviously visible that doping tailors the band gap of the parent material. The Cd<sup>2+</sup> and Na<sup>+</sup> - doped Cu<sub>2</sub>Se

films show higher band gap values than those of the other films due to the higher carrier concentration that moved the optical edge towards lower energy and broadened the energy gap. The dopant may dominantly contribute to the width of localized states within the optical band of Cu<sub>2</sub>Se. Introduction of Cd<sup>2+</sup> and Na<sup>+</sup> into Cu<sub>2</sub>Se increases the width of the localized states, hence resulting in increasing the band gap. Similar trends of these results were reported for trivalent Sb<sup>3+</sup> - doped ZnO and trivalent Al<sup>3+</sup> - doped ZnS films studied by other researchers [5, 17].

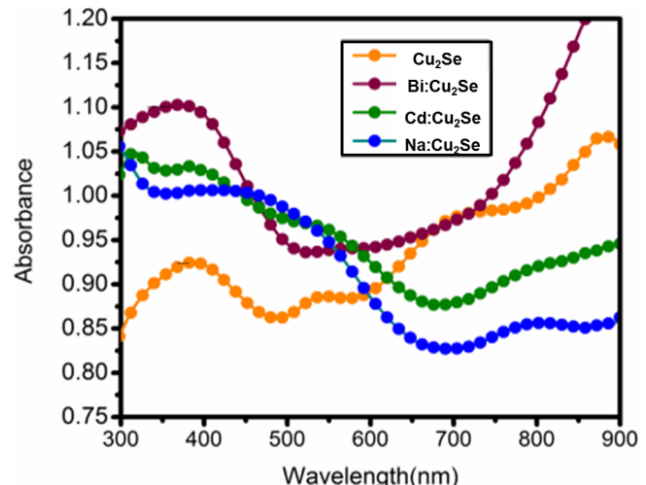
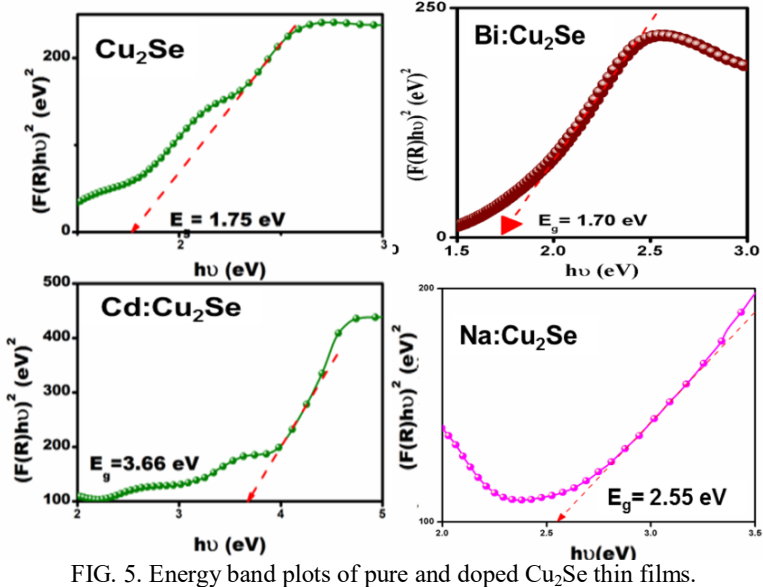


FIG. 4. Absorpance spectra of pure and doped Cu<sub>2</sub>Se thin films.



#### **Conclusions**

Pure and Bi3+, Cd2+, Na+ - doped Cu2Se thin films with cubic phase have been deposited successfully by chemical bath deposition method and the crystalline size was decreased from 84 nm to almost 70 nm for Bi- and Cd-doped and to 81 nm for Na-doped Cu<sub>2</sub> Se films. The films were homogeneous and uniform size particles were covering the surface. The optical absorbance study reveals that Bi-doped films show lower band gap of 1.70 eV, whereas Cdand Na-doped films show higher values of 3.66 eV and 2.55 eV when compared to the band gap of 1.75 eV of pure Cu<sub>2</sub>Se films.

#### Acknowledgements

The authors are thankful to the DST-FIST and UGC-SAP, New Delhi for providing financial support to the Department of Physics, Manonmaniam Sundaranar University.

Communication Sudha et al.

#### References

- [1] Thirumavalavan, S., Mani, K. and Sagadevan, S., Materials Research, 18 (2015) 1000.
- [2] Zhao, Y., Zhu, L., Jiang, Y., Xie, H., Zhang, G. and Ba, N., Mater. Lett., 147 (2015) 82.
- [3] Rong, F., Bai, Y., Chen, T. and Zheng, W., Mater. Res. Bul., 47 (2012) 92.
- [4] Pathan, H.M., Lokhande, C.D., Amalnerkar, D.P. and Seth, T., Appl. Surf. Sci., 211 (2003) 48.
- [5] Reddy, D.A., Liu, C., Vijayalakshmi, R.P. and Reddy, B.K., J. Alloys Compd., 582 (2014) 257.
- [6] Manohari, A.G., Dhanapandian, S., Manoharan, C. and Kumar, K.S., Materials Science, in: Semiconductor Processing, 17 (2014) 138.
- [7] Luo, W., Yang, M., Chen, F., Shen, Q., Jiang, H. and Zha, L., Materials Transactions, 51 (2010) 288.
- [8] Patel, N.H., Deshpande, M.P., Bhatt, S.V., Patel, K.R. and Chaki, S.H., Adv. Mat. Lett., 5 (2014) 671.

- [9] Kumar, A.G.S., Obulapathi, L., Sarmash, T.S., Rani, D.J., Maddaiah, M., Rao, T.S. and Asokan, K., JOM, 67 (2015) 834.
- [10] Mondal, S. and Mitra, P., Bull. Mater. Sci., 35 (2012) 751.
- [11] Bera, S.R. and Saha, S., IOSR Journal of Electrical and Electronics Engineering (IOSR-JEEE), 11 (2016) 11.
- [12] Ali, S.M., Farooq, W.A., Baig, M.R., Shar, M.A., Atif, M., Alghamdi, S.S., Algarawi, M.S., Naeem-Ur-Rehman and Aziz, M.H., Materials Science-Poland, 33 (2015) 601.
- [13] Kumar, S. and Thangavel, R., J. Sol-Gel Sci. Technol., 67 (2013) 50.
- [14] Peng, P., Gong, Z.N., Liu, F.S., Huang, M.J., Ao, W.Q., Li, Y. and Li, J.Q., Intermetallics, 75 (2016) 72.
- [15] Jassim, S.A., Zumaila, A.A.R.A. and Waly, G.A.A.A., Results in Physics, 3 (2013) 173.
- [16] Mushtaq, S., Ismail, B., Raheel, M. and Zeb, A., Natural Science, 8 (2016) 33.
- [17] Rana, S.B., Singh, A. and Singh. S., Int. J. Nanoelectron. Mater., 6 (2013) 44.

### Jordan Journal of Physics

#### Communication

# Hydrothermally Synthesized CoSn(OH)<sub>6</sub> Nanoparticles for Electrochemical Performance\*

#### V. K. Premkumar<sup>a</sup> and G. Sivakumar<sup>b</sup>

Department of Physics, Annamalai University, Chidambaram – 608002, Tamilnadu, India.

Received on: 22/5/2017; Accepted on: 5/11/2017

Abstract: Cubic phase CoSn(OH)<sub>6</sub> nanoparticles were successfully synthesized by a facile hydrothermal method using NaOH as a mineralizer. The prepared sample was analyzed by using X-ray diffraction (XRD) and the analysis confirmed that the CoSn(OH)<sub>6</sub> nanoparticles have a spinel cubic structure with lattice space group Pn3m and mean crystalline size of 25 nm. Field emission scanning electron microscope (FE-SEM) study showed that the cubic with polyhedral shaped surface morphology of the CoSn(OH)<sub>6</sub> nanoparticles was seen. The specific capacitance value of 450 Fg<sup>-1</sup> was calculated at the scan rate of 2 mVs<sup>-1</sup> as measured by using cyclic voltammetry. In the present investigation, the prepared CoSn(OH)<sub>6</sub> nanoparticles are suggested as a potential candidate for supercapacitor applications.

**Keywords:** Hydrothermal, Nanoparticles, Cubic, Cyclic voltammetry, Specific capacitance.

#### Introduction

In recent decades, stannate nanostructure materials have attracted special attention because of their tailor-made properties in a wide range of applications in energy storage [1-3]. Among various materials, transition metal oxide-based material play a very important role in supercapacitor applications [4, 5]. However, RuO2 is considered a good electrode material for supercapacitor because of its high specific capacity of 720 F/g in aqueous acid electrolytes [6]. Nevertheless, the disadvantages are high cost and toxic behavior. Owing to this, the capacitance behavior of different oxide materials such as MnO<sub>2</sub>, NiO, Bi<sub>2</sub>O<sub>3</sub> and SnO<sub>2</sub> was studied using various electrochemical techniques [7-10]. So, researchers focused on generating alternate materials for supercapacitor applications due to the rising demand and in order to enhance the

electrochemical performance of the supercapacitor. Hence, we designed metal stannate hydroxide-based nanomaterials due to their most impressive properties, such as high electron mobility, high power density and long cycle life [11-13]. In this investigation, CoSn(OH)<sub>6</sub> nanoparticles are synthesized by using the facile hydrothermal method in the presence of NaOH as a mineralizer to study the structural, morphological and electrochemical performance of the synthesized material.

#### **Experimental Procedure**

The chemical reagents (CoCl<sub>2</sub>. 6H<sub>2</sub>O, SnCl<sub>4</sub>.5H<sub>2</sub>O and NaOH) were purchased from Merck chemicals (99% pure) and the experiment was carried out without any further purification. CoSn(OH)<sub>6</sub> was successfully synthesized by

Corresponding Author: G. Sivakumar

Email: gsk cisl@yahoo.com

b CISL, Department of Physics, Annamalai University, Chidambaram – 608002, Tamilnadu, India.

<sup>\*&</sup>quot;6<sup>th</sup> National Seminar on Advances in Materials Science NSAMS-2017, held on March 2, 3-2017 at the Department of Physics, Manonmaniam Sundaranar University, Tirunelveli-627 012, Tamilnadu, India".

Communication Premkumar and Sivakumar

using the hydrothermal method [14]. An amount of 30 ml containing 0.06 M of CoCl<sub>2</sub>.6H<sub>2</sub>O and 0.03 M of SnCl<sub>4</sub>.5H<sub>2</sub>O was dissolved using deionized water separately to form a transparent solution and then mixed together. An appropriate amount of 3M NaOH solution was added to the mixed solution drop-wise to adjust the pH level up to ~10 under constant stirring. The resultant solution suddenly formed blue color precipitates, which indicates the formation of cobalt stannate hydroxide colloidal suspension. The solution was transferred to a Teflon-coated stainless steel autoclave at 200 °C for 24 h in hot air oven for hydrothermal reaction. After hydrothermal reaction, the resultant solution was washed with deionized water and ethanol several times and further dried in an oven at 100 °C for 6 hours. The resultant product was prepared for further characterization.

The synthesized CoSn(OH)<sub>6</sub> nanoparticles were characterized by X-ray diffraction (XRD), Field emission scanning electron microscopy (FE-SEM) and Cyclic voltammetry (CV) analyses.

Crystalline structure and size of  $CoSn(OH)_6$  were determined by using powder X-ray diffractometer (PAN alytical, Model: PW3040/60 X'pert PRO) with CuK  $\alpha$  radiation ( $\lambda = 1.54060 \text{Å}$ ) at 40 kV and 30 mA. The step scan was recorded for 2 $\theta$  values in the angular range from 10° to 80° with a scanning speed of 10°min<sup>-1</sup>. The morphology of the  $CoSn(OH)_6$ 

nanoparticles was observed through the FE-SEM (ZEISS Supra 40VP). Electrochemical performance of the synthesized nanoparticles was measured by cyclic voltammeter (CV) model CHI 660 and the CV measurement was carried out at a potential window between -1.5 V and 2 V.

#### Results and Discussion

FIG. 1 shows the X-ray diffraction pattern of CoSn(OH)<sub>6</sub> nanoparticles. The XRD pattern exhibits strong reflection of hkl planes (111), (200), (220) and (420), indicating that the corresponding 2θ values of 19.3°, 22.8°, 32.5° and 52.2° are indexed for the spinel cubic phase of CoSn(OH)<sub>6</sub> from JCPDS card no. 74-0365. The average crystal size was determined by Debye Scherer formula [15].

$$D = \frac{\kappa \lambda}{\beta Cos\theta}; \tag{1}$$

where D is the crystallite size, K (= 0.89) is a constant related to the shape of the crystal,  $\lambda$  is the wavelength of the radiation employed,  $\beta$  is the full width at half maximum (FWHM) of the obtained reflection peak in radians and  $\theta$  is the Bragg diffraction angle. The calculated mean crystalline size was found to be 25 nm. The XRD study confirmed that the as prepared sample was cubic structured CoSn(OH)<sub>6</sub> nanoparticles without any impurities and with primitive lattice Pn3m space group.

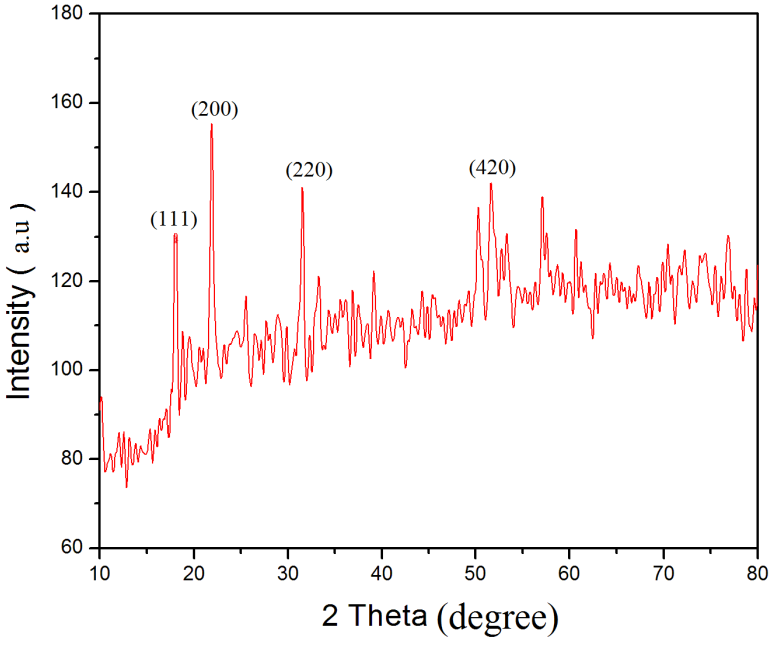


FIG. 1. XRD pattern of CoSn(OH)<sub>6</sub> nanoparticles.

The morphology of CoSn(OH)<sub>6</sub> nanoparticles was observed by FE-SEM micrograph measurements. FIG. 2 shows the FE-SEM image of CoSn(OH)<sub>6</sub> nanoparticles. It clearly demonstrates that the nanoparticles are aggregated in polyhedral and cubic shape [16].

From the figure, it can be seen that the CoSn(OH)<sub>6</sub> nanoparticles are evenly distributed in the range of 20-50 nm, which indicates that the FESEM result of CoSn(OH)<sub>6</sub> nanoparticles closely matches the XRD result.

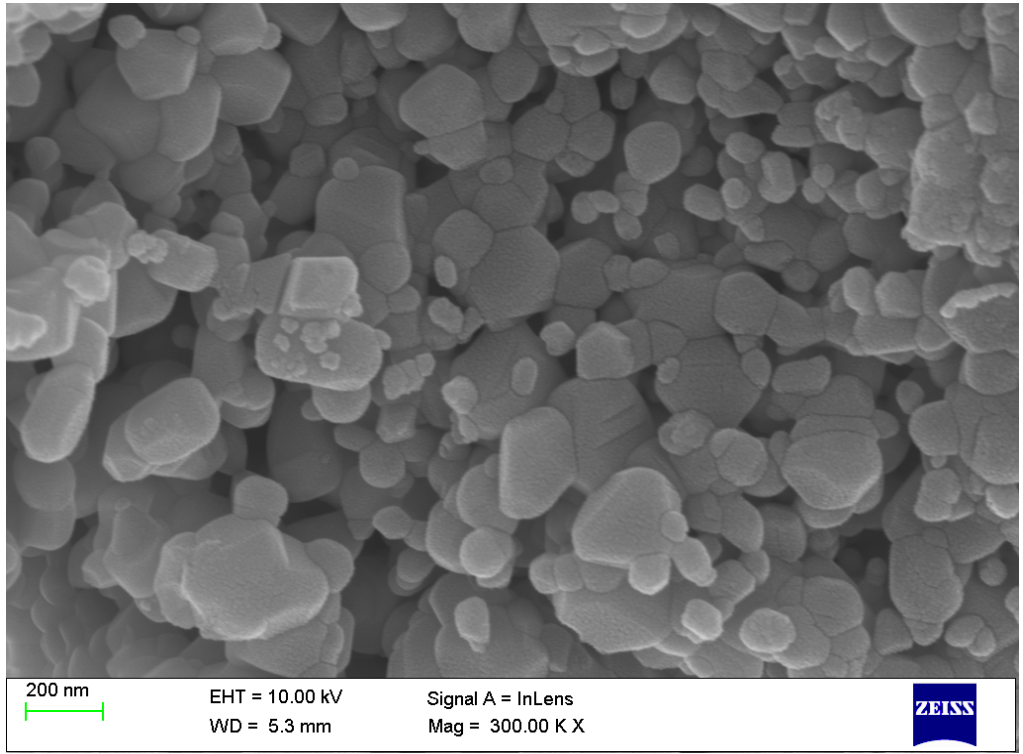


FIG. 2. FE-SEM image of CoSn(OH)6 nanoparticles.

For investigating electrochemical performance, the CV analysis was carried out in the potential window between -1.5 V and 2 V at different scan rates as shown in FIG. 3. The CoSn(OH)<sub>6</sub> nanoparticles were tested as an electrode to evaluate the electrochemical performance in a three-electrode system [17]. It exhibits quasi rectangular shape of CV curve with scan rate values from 2 to 50 mVs<sup>-1</sup>. The specific capacitance of synthesized CoSn(OH)<sub>6</sub> nanoparticles can be calculated using the following formula [18]:

$$Cs = \frac{Q}{\Delta v.m} (2)$$

where Cs is the specific capacitance, Q is the anodic charge, m is the mass of the electrode material (mg) and  $\Delta v$  is the scan rate (mV s<sup>-1</sup>). While increasing the scan rate, the shape of curve reduction indicates that the change in the specific capacitance value gets decreased from

 $450~Fg^{\text{--}1}$  at  $~2~mVs^{\text{--}1}$  to  $23~Fg^{\text{--}1}$  at  $50~mVs^{\text{--}1}$  as shown in Table 1. The CV curve exhibits a shape different from the identical rectangular shape, which indicates the pseudo capacitance nature of the CoSn(OH)<sub>6</sub> nanoparticles [19]. In addition, it confirms the changes in specific capacitance while increasing scan rate owing to the pseudo capacitance nature of CoSn(OH)<sub>6</sub> nanoparticles. It indicates that at lower scan rates, ionic diffusion takes place and electrons interact with the inner and outer surfaces of the nanoparticles due to Faradaic reaction [16]. At increased scan rates, ionic diffusion takes place only at the outer surface of the nanoparticles [20]. The CoSn(OH)<sub>6</sub> nanoparticles have a high specific capacitance value of 450 Fg<sup>-1</sup> at a scan rate of 2 mVs<sup>-1</sup>. It can be concluded that CoSn(OH)<sub>6</sub> nanoparticles are suitable for supercapacitor applications.

Communication Premkumar and Sivakumar

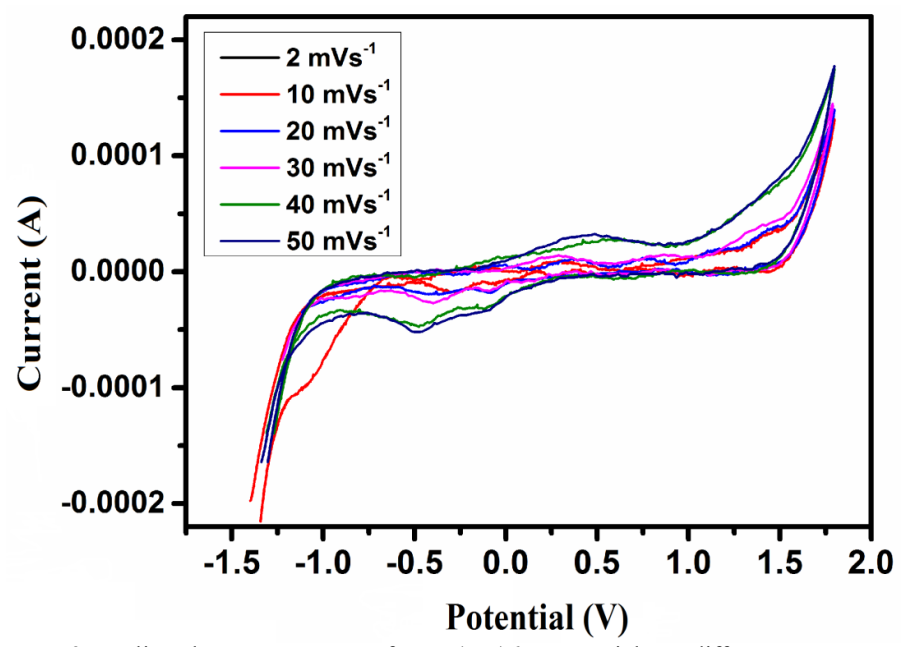


FIG. 3. Cyclic voltammetry curves of CoSn(OH)6 nanoparticles at different scan rates.

TABLE 1. Specific capacitance of CoSn(OH)<sub>6</sub> nanoparticles at different scan rates.

CoSn(OH) <sub>6</sub> nanoparticles						
Scan rate (mVs <sup>-1</sup> )	2	10	20	30	40	50
Specific capacitance (Fg <sup>-1</sup> )	450	136	65	44	32	23

#### **Conclusions**

CoSn(OH)<sub>6</sub> nanoparticles were synthesized successfully by using the facile hydrothermal method. The XRD analysis confirmed cubic structure of CoSn(OH)<sub>6</sub> and a mean crystal size of 25 nm. FE-SEM reveals the synthesized product to be in polyhedral with agglomerated cubic shape. The average crystalline size from

XRD matches well the FE-SEM result. The superior specific capacitance value of 450 Fg<sup>-1</sup> was obtained at the scanning rate of 2 mVs<sup>-1</sup>. We deem that this facile process and specific capacitance performance enlighten the CoSn(OH)<sub>6</sub> nanoparticles to be a potential candidate for supercapacitor applications.

#### References

- [1] Xia, X., Tu, J., Mai, Y., Wang, X., Gu, C. and Zhao, X., Journal of Materials Chemistry, 21 (25) (2011) 9319.
- [2] Liu, Y., Jiao, Y., Zhang, Z., Qu, F., Umar, A. and Wu, X., ACS Applied Materials & Interfaces, 6 (3) (2014) 2174.
- [3] Chen, S., Zhu. J., Wu, X., Han, Q. and Wang, X., ACS Nano, 4 (5) (2010) 2822.
- [4] Li, F., Song, J., Yang, H., Gan, S., Zhang, Q., Han, D., Ivaska, A. and Niu, L., Nanotechnology, 20 (45) (2009) 455602.
- [5] Meher, S.K. and Rao, G.R., The Journal of Physical Chemistry C, 115 (31) (2011) 15646.

- [6] Hu, C., Chang, K., Lin, M. and Wu, Y., Nano-letters, 6 (12) (2006) 2690.
- [7] Yuan, L., Lu, X., Xiao, X., Zhai, T., Dai, J., Zhang, F., Hu, B. et al., ACS Nano, 6 (1) (2011) 656.
- [8] Yuan, C., Zhang, X., Su, L., Gao, B. and Shen, L., Journal of Materials Chemistry, 19 (32) (2009) 5772.
- [9] Xu, H., Hu, X., Yang, H., Sun, Y., Hu, C. and Huang, Y., Adv. Energy Mater., 5(6) (2015) 1401882.
- [10] Ng, K.C., Zhang, S., Peng, C. and Chen, G. Z., Journal of the Electrochemical Society, 156 (11) (2009) A846.

- [11] Wang, Z., Wang, Z., Wu, H. and Lou, X.W.D., Scientific Reports, 3 (2013) 1391.
- [12] Hu, X., Tang, Y., Xiao, T., Jiang, J., Jia, Z., Li, D., Li, B. and Luo, L., The Journal of Physical Chemistry C, 114 (2) (2009) 947.
- [13] Wang, G., Sun, X., Lu, F., Yu, Q., Liu, C. and Lian, J., Journal of Solid State Chemistry, 185 (2012) 172.
- [14] Zhang, J., Liang, J., Zhu, Y., Wei, D., Fan, L. and Qian, Y., Journal of Materials Chemistry A, 2 (8) (2014) 2728.
- [15] Dinesh, S., Barathan, S., Premkumar, V.K., Sivakumar, G. and Anandhan, N., Journal of Materials Science: Materials in Electronics, 27 (9) (2016) 9668.

- [16] Premkumar, V.K., Dinesh, S., Sivakumar, G. and Barathan, S., Journal of Materials Science: Materials in Electronics, 28 (6) (2017) 4780.
- [17] Sivagurunathan, P. and Gibin, S.R., Journal of Materials Science: Materials in Electronics, 27 (3) (2016) 2601.
- [18] Dinesh, S., Anandan, M., Premkumar, V.K., Barathan, S., Sivakumar, G. and Anandhan, N., Materials Science and Engineering B, 214 (2016) 37.
- [19] Dinesh, S., Thirugnanam, N., Anandan, M., Barathan, S. and Anandhan, N., Journal of Materials Science: Materials in Electronics, 27 (2016) 12786.
- [20] Premkumar, V.K. and Sivakumar, G., Journal of Materials Science: Materials in Electronics, 28 (19) (2017) 14226.

# Jordan Journal of Physics

## Communication

# Synthesis and Characterization of CuMS<sub>2</sub> (M= Bi, Sb) Thin Films Prepared by CBD Method\*

T. Daniel<sup>a</sup>, K. Mohanraj<sup>a</sup> and G. Sivakumar<sup>b</sup>

Received on: 22/5/2017; Accepted on: 14/9/2017

**Abstract:** CuMS $_2$  (M= Bi, Sb) thin films (0.1 M) were deposited by chemical bath deposition (CBD) method and characterized by X-ray diffraction (XRD) and UV-Visible (UV) analyses. The XRD pattern confirms the formation of orthorhombic structured CuBiS $_2$  with Cu $_2$ S phases as an impurity and orthorhombic structured CuSbS $_2$ . UV studies show higher optical absorption in the visible region, which indicates that the resulting material can be used as an absorbing material in solar cells.

**Keywords:** CuBiS<sub>2</sub>, CuSbS<sub>2</sub>, CBD, XRD, Orthorhombic, Absorbing materials.

#### Introduction

Metal-based ternary chalcogenide semiconductors ABX<sub>2</sub> (A= Cu, Ag; B= Bi, Sb, In; X= S, Se, Te) have considerable applications for a wide variety of IR detectors, p-n junction solar cells and thermoelectric materials [1]. CuSbS<sub>2</sub> and CuBiS<sub>2</sub> are semi-conducting materials having the capability of covering maximum part of the visible region and infra-red region in the electromagnetic spectrum ( $E_g = 1.5$  to 2.2 eV), higher optical absorption coefficient (>10<sup>4</sup> cm<sup>-1</sup>) [2] and can be easily obtained in the form of thin films. The advantages of these materials are: 1) earth abundance 2) low cost when compared to Ag, In and Te and 3) lower toxicity. Hence, the present study aims to deposit CuMS<sub>2</sub> (M= Bi, Sb) thin films by simple CBD method and to study their structural and optical properties.

#### **Experimental Details**

AR grade chemicals were used in this study.  $CuMS_2$  (M = Bi, Sb) thin films have been prepared by CBD technique. For the preparation of  $CuBiS_2$  thin films, 0.1M of  $Cu(NO_3)_2$  and 0.1M of  $Na_2S_2O_3$  were dissolved in double

distilled water and added into ethylene glycol dissolved 0.1M of Bi(NO<sub>3</sub>)<sub>3</sub> solution at room temperature under vigorous stirring. Then, ultrasonically cleaned substrates were immersed in the prepared solution at rest for 24 h. The preparation of CuSbS<sub>2</sub> thin film process was similar to that of CuBiS<sub>2</sub>; here, 0.1 M of acetone dissolved SbCl<sub>3</sub> was used instead of Bi(NO<sub>3</sub>)<sub>3</sub>. After dipping for 24h, the substrates were taken out of the bath, rinsed with double distilled water and dried in room temperature. The prepared films were annealed at 200 °C in air atmosphere for 1h and characterized by X-ray diffraction (XRD) and UV-Visible (UV) analyses.

## **Results and Discussion**

Film thickness was calculated by using Swanepoel method [3] and found to be 1191 nm for  $CuBiS_2$  and 303 nm for  $CuSbS_2$  thin films. Fig. 1 shows the XRD patterns of  $CuBiS_2$  and  $CuSbS_2$  thin films. The  $CuBiS_2$  film shows the prominent peaks at  $2\theta = 30.09^{\circ}$  and  $54.05^{\circ}$  corresponding to the reflection of (013) and (216) planes, respectively, for orthorhombic

 $<sup>^{</sup>a}$  Department of Physics, Manonmaniam Sundaranar University, Tamilnadu, India.

<sup>&</sup>lt;sup>b</sup> CISL, Department of Physics, Annamalai University, Tamilnadu, India.

Communication Daniel et al.

CuBiS<sub>2</sub> [JCPDS Card No. 65-1300 and 89-2670]. An additional peak is observed at  $2\theta$ =37.88° belonging to (102) plane of hexagonal structured Cu<sub>2</sub>S [JCPDS Card No. 89-2670]. In the case of CuSbS<sub>2</sub>, the peaks at  $2\theta$  =28.78° and 25.33° correspond to the planes of (111) and (011), which confirms the formation of

orthorhombic CuSbS<sub>2</sub>. The low intensity of the peaks indicates that the films consist of coarsely fine grains/or are nanocrystalline in nature. Crystalline size was calculated using Scherrer formula and found to be 68 nm and 20 nm for CuBiS<sub>2</sub> and CuSbS<sub>2</sub>, respectively.

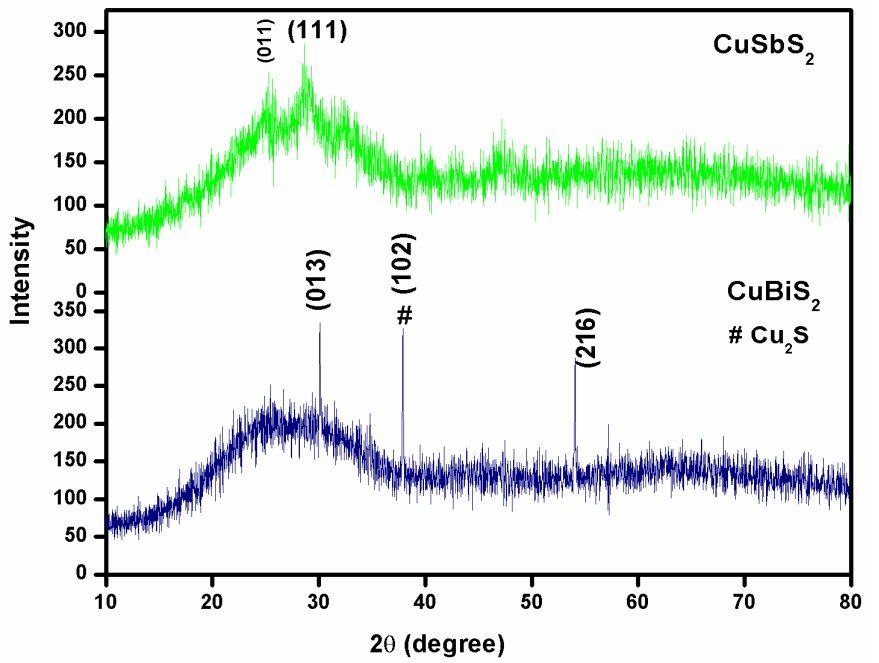


FIG. 1. XRD patterns of CuBiS<sub>2</sub> and CuSbS<sub>2</sub> thin films.

Fig. 2 shows the optical absorption spectra of CuBiS<sub>2</sub> and CuSbS<sub>2</sub> thin films. It can be seen from the spectra that the CuBiS<sub>2</sub> film showed better absorption in the visible region (300 -700 nm) compared to CuSbS<sub>2</sub> film. Optical absorption coefficient (a) was calculated and found in the range of  $10^{\circ}$  cm<sup>-1</sup>. This higher  $\alpha$ value confirms that the deposited films are potential candidates for solar cell applications. Eg plot (Fig. 2 inset) was drawn using Tauc's plot [1] and found to be 1.69 eV and 1.8 eV for CuBiS<sub>2</sub> and CuSbS<sub>2</sub> thin films, respectively, which is comparable to earlier literature (1.5 -1.9 eV) [1,2]. ON the other hand, the thin films are having direct bandgap energy [4-7]. In the case of CuBiS<sub>2</sub>, the band gap is comparatively lower than in the case of CuSbS<sub>2</sub> because of Bi<sup>3</sup> having higher anisotropic electronic behaviour, low conduction band effective mass and high electron mobility [8]. The Eg values lie closer to optimum value for solar cells.

#### **Conclusion**

In this work, CuMS<sub>2</sub> (M= Bi, Sb) thin films (0.1 M) were deposited by chemical bath deposition method. The XRD pattern confirms the polycrystalline nature of orthorhombic structured CuBiS<sub>2</sub> and CuSbS<sub>2</sub>. UV studies show higher optical absorption coefficient ( $\alpha$  >10<sup>4</sup> cm<sup>-1</sup>). Band gap energy was found to be 1.69 and 1.8 eV for CuBiS<sub>2</sub> and CuSbS<sub>2</sub> thin films, respectively, which indicates that the materials have potential applications in the field of solar cells.

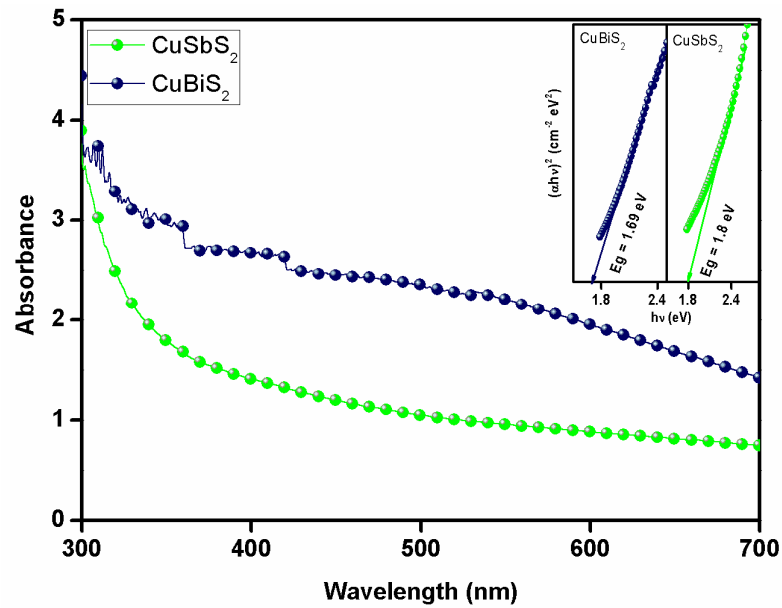


FIG. 2. UV-visible spectra of CuBiS<sub>2</sub> & CuSbS<sub>2</sub> thin films; inset: Eg plotplot.

#### **Acknowledgements**

The author T. Daniel expresses his sincere thanks to University Grants Commission (UGC), New Delhi for providing financial support under

the scheme of UGC Basic Scientific Research (UGC-BSR) fellowship.

#### References

- [1] Thongtem, T., Jaroenchaichana, J. and Thongtem, S., Mat. Lett., 63 (2009) 2163.
- [2] Ramasamy, K., Sims, H., Butler, W.H. and Gupta, A., J. Am. Chem. Soc., 136 (2014) 1587.
- [3] Vijila, J.J.J., Mohanraj, K. and Sivakumar, G., Mater. Res. Express, 3 (2016) 076408.
- [4] Garza, C., Shaji, S., Arato, A., Tijerina, E.P., Castillo, G.A., Roy, T.K.D. and Krishnan, B., Sol. Energ. Mat. Sol. Cells, 95 (2011) 2001.
- [5] Yang, B., Wang, L., Han, J., Zhou, Y., Song, H., Chen, S., Zhong, J., Lv, L., Niu, D. and Tang, J., Chem. Mater., 26 (2014) 3135.
- [6] Li, J., Jiang, L., Wang, B., Liu, F., Yang, J., Tang, D., Lai, Y. and Li, J., Electrochem. Acta, 87 (2013) 153.
- [7] Sonawane, P.S., Wani, P.A., Patil, L.A. and Seth, T., Mater. Chem. Phys., 84 (2004) 221.
- [8] Mahendran, C. and Suriyanarayanan, N., Physica B, 408 (2013) 62.

## **Authors Index**

A. M. Ezhil Raj	107
A. Mohan	107
A. P. Sudha.	125
G. Anushya	91
G. Sivakumar	101,125,131,137
J. Henry	101,125
K. A. Al-Khaza'leh	85
K. Mohanraj	101,125,137
K. Umamakeshvari	107
M. Mahdavi	77
N. M. Ershaidat	115
T. Daniel	137
T.H. Freeda	91
U. Sankar	107
V. K. Premkumar	131
W. Salah	115

# Subject Index

Absorbing materials	137
Annual effective dose	85
Beam dynamics	115
Bruggeman factor	107
Cancer risk.	85
Cation doping	125
chemical bath deposition (CBD)	125, 137
CHPD crystals	91
Concentration	85
Cu <sub>2</sub> Se thin films	125
Cu <sub>2</sub> ZnSnS <sub>4</sub> thin films	101
Cubic	131
CuBiS <sub>2</sub>	137
CuSbS <sub>2</sub>	137
Cyclic voltammetry	131
Dielectric relaxation	107
Free electron laser.	115
Growth inhibition	91
Hydrothermal	131
Kirkwood correlation factor	107
Muonic atoms	77
Nanoparticles	131
Natural foods	91
Orthorhombic	137
Photoluminescence	101
Radionuclides	85
Resonance molecular formation	77
RF-photoinjector	115
SILAR Method	101
Specific capacitance	131
Thickness layers	77
Time domain reflectometry	107
Transport theory	77
Wakefields	115
YRD	101 125 13

المراجع: يجب طباعة المراجع بأسطر مزدوجة ومرقمة حسب تسلسلها في النص. وتكتب المراجع في النص بين قوسين مربعين. ويتم اعتماد اختصارات الدوريات حسب نظام Wordlist of Scientific Reviewers.

الجداول: تعطى الجداول أرقاما متسلسلة يشار إليها في النص. ويجب طباعة كل جدول على صفحة منفصلة مع عنوان فوق الجدول. أما الحواشى التفسيرية، التى يشار إليها بحرف فوقى، فتكتب أسفل الجدول.

الرسوم التوضيحية: يتم ترقيم الأشكال والرسومات والرسومات البيانية (المخططات) والصور، بصورة متسلسلة كما وردت في النص.

تقبل الرسوم التوضيحية المستخرجة من الحاسوب والصور الرقمية ذات النوعية الجيدة بالأبيض والأسود، على ان تكون أصيلة وليست نسخة عنها، وكل منها على ورقة منفصلة ومعرفة برقمها بالمقابل. ويجب تزويد المجلة بالرسومات بحجمها الأصلي بحيث لا تحتاج إلى معالجة لاحقة، وألا تقل الحروف عن الحجم 8 من نوع Times New Roman وألا تقل سماكة الخطوط عن 0.5 وبكثافة متجانسة. ويجب إزالة جميع الألوان من الرسومات ما عدا تلك التي ستنشر ملونة. وفي حالة إرسال الرسومات بصورة رقمية، يجب أن تتوافق مع متطلبات الحد الأدنى من التمايز (times Resolution) لرسومات الأبيض والأسود الخطية، و 600 dpi للرسومات باللون الرمادي، وأن ترسل الرسوم التوضيحية بالحجم الفعلي الذي سيظهر في المجلة. وسواء أرسل المخطوط بالبريد أو عن طريق الشبكة (Online)، يجب أرسال نسخة ورقية أصلية ذات نوعية جيدة للرسومات التوضيحية.

مواد إضافية: تشجع المجلة الباحثين على إرفاق جميع المواد الإضافية التي يمكن أن تسهل عملية التحكيم. وتشمل المواد الإضافية أي اشتقاقات رياضية مفصلة لا تظهر في المخطوط.

المخطوط المنقح (المعدل) والأقراص المدمجة: بعد قبول البحث للنشر وإجراء جميع التعديلات المطلوبة، فعلى الباحثين تقديم نسخة أضلية ونسخة أخرى مطابقة للأصلية مطبوعة بأسطر مزدوجة، وكذلك تقديم نسخة إلكترونية تحتوي على المخطوط كاملا مكتوبا على Microsoft Word for Windows 2000 أو ما هو استجد منه. ويجب إرفاق الأشكال الأصلية مع المخطوط النهائي المعدل حتى لو تم تقديم الأشكال إلكترونيا. وتخزن جميع ملفات الرسومات على شكل (jpg)، وتقدم جميع الرسومات التوضيحية بالحجم الحقيقي الذي ستظهر به في المجلة. ويجب إرفاق قائمة ببرامج الحاسوب التي استعملت في كتابة النص، وأسماء الملفات على قرص مدمج، حيث يعلم القرص بالاسم الأخير للباحث، وبالرقم المرجعي للمخطوط للمراسلة، وعنوان المقالة، والتاريخ. ويحفظ في مغلف واق.

#### حقوق الطبع

يُشَكِّلُ تقديم مخطوط البحث للمجلة اعترافاً صريحاً من الباحثين بأنَ مخطوط البحث لم يُنْشَر ولم يُقَدُم للنشر لدى أي جهة أخرى كانت وبأي صيغة ورقية أو إلكترونية أو غيرها. ويُشترط على الباحثين ملء أنموذج يَنُصُ على نقْل حقوق الطبع لتُصبح ملكاً لجامعة اليرموك قبل الموافقة على نشر المخطوط. ويقوم رئيس التحرير بتزويد الباحثين بإنموذج نقُل حقوق الطبع مع النسخة المُرْسَلَة للتنقيح. كما ويُمنع إعادة إنتاج أيّ جزء من الأعمال المنشورة في المجلّة من دون إذن خَطّيً مُسبَق من رئيس التحرير.

#### إخلاء المسؤولية

إن ما ورد في هذه المجلة يعبر عن آراء المؤلفين، ولا يعكس بالضرورة آراء هيئة التحرير أو الجامعة أو سياسة اللجنة العليا للبحث العلمي أو وزارة التعليم العالي والبحث العلمي. ولا يتحمل ناشر المجلة أي تبعات مادية أو معنوية أو مسؤوليات عن استعمال المعلومات المنشورة في المجلة أو سوء استعمالها.

#### الفهرسة: المجلة مفهرسة في:



Emerging Sources Citation Index (ESCI)



#### معلومات عامة

المجلة الأردنية للفيزياء هي مجلة بحوث علمية عالمية متخصصة مُحكمة تصدر بدعم من صندوق دعم البحث العلمي، وزارة التعليم العالي والبحث العلمي، عمان، الأردن. وتقوم بنشر المجلة عمادة البحث العلمي والدراسات العليا في جامعة اليرموك، إربد، الأردن. وتنشر البحوث العلمية الأصيلة، إضافة إلى المراسلات القصيرة Short Communications، والملاحظات الفنية الأصيلة، إضافة إلى المراسلات القصيرة Review Articles، في مجالات الفيزياء النظرية والتجريبية، باللغتين العربية والإنجليزية.

#### تقديم مخطوط البحث

تقدم البحوث عن طريق إرسالها إلى البريد الإلكتروني : jjp@yu.edu.jo

تقديم المخطوطات إلكترونيًا: اتبع التعليمات في موقع المجلة على الشبكة العنكبوتية.

ويجري تحكيمُ البحوثِ الأصيلة والمراسلات القصيرة والملاحظات الفنية من جانب مُحكِّمين اثنين في الأقل من ذوي الاختصاص والخبرة. وتُشَجِّع المجلة الباحثين على اقتراح أسماء المحكمين. أما نشر المقالات الخاصّة في المجالات الفيزيائية النَشِطّة، فيتم بدعوة من هيئة التحرير، ويُشار إليها كذلك عند النشر. ويُطلَّب من كاتب المقال الخاص تقديم تقرير واضح يتسم بالدقة والإيجاز عن مجال البحث تمهيداً للمقال. وتنشر المجلة أيضاً مقالات المراجعة في الحقول الفيزيائية النشطة سريعة التغير، وتُشَجِّع كاتبي مقالات المراجعة أو مُستكتبيها على إرسال مقترح من صفحتين إلى رئيس التحرير. ويُرْفَق مع البحث المكتوب باللغة العربية ملخص (Abstract) وكلمات دالة (Keywords) باللغة الإنجليزية.

#### ترتيب مخطوط البحث

يجب أن تتم طباعة مخطوط البحث ببنط 12 نوعه Times New Roman، وبسطر مزدوج، على وجه واحد من ورق A (21.6 × 27.9 سم) مع حواشي 3.71 سم، باستخدام معالج كلمات ميكروسوفت وورد 2000 أو ما استتجد منه. ويجري تنظيم أجزاء المخطوط وفق الترتيب التالي: صفحة العنوان، الملخص، رموز التصنيف (PACS)، المقدّمة، طرق البحث، النتائج، المناقشة، الخلاصة، الشكر والعرفان، المراجع، الجداول، قائمة بدليل الأشكال والصور والإيضاحات، ثم الأشكال والصور والإيضاحات. وتُكتّب العناوين الرئيسة بخط عامق، بينما تكتّب العناوين الفرعية بخط مانل.

صفحة العنوان: وتشمل عنوان المقالة، أسماء الباحثين الكاملة وعناوين العمل كاملة. ويكتب الباحث المسؤول عن المراسلات اسمه مشارا إليه بنجمة، والبريد الإلكتروني الخاص به. ويجب أن يكون عنوان المقالة موجزا وواضحا ومعبرا عن فحوى (محتوى) المخطوط، وذلك لأهمية هذا العنوان لأغراض استرجاع المعلومات.

الملخص: المطلوب كتابة فقرة واحدة لا تزيد على مائتي كلمة، موضحة هدف البحث، والمنهج المتبع فيه والنتائج وأهم ما توصل إليه الباحثون.

الكلمات الدالة: يجب أن يلى الملخص قائمة من 4-6 كلمات دالة تعبر عن المحتوى الدقيق للمخطوط لأغراض الفهرسة.

PACS: يجب إرفاق الرموز التصنيفية، وهي متوافرة في الموقع Phttp://www.aip.org/pacs/pacs06/pacs06-toc.html:

المقدمة: يجب أن توضّح الهدف من الدراسة وعلاقتها بالأعمال السابقة في المجال، لا أن تكون مراجعة مكثفة لما نشر (لا تزيد المقدمة عن صفحة ونصف الصفحة مطبوعة).

طرائق البحث (التجريبية / النظرية): يجب أن تكون هذه الطرائق موضحة بتفصيل كاف لإتاحة إعادة إجرائها بكفاءة، ولكن باختصار مناسب، حتى لا تكون تكرارا للطرائق المنشورة سابقا.

النتائج: يستحسن عرض النتائج على صورة جداول وأشكال حيثما أمكن، مع شرح قليل في النص ومن دون مناقشة تفصيلية.

المناقشة: يجب أن تكون موجزة وتركز على تفسير النتائج.

الاستنتاج: يجب أن يكون وصفا موجزا لأهم ما توصلت إليه الدراسة ولا يزيد عن صفحة مطبوعة واحدة.

الشكر والعرفان: الشكر والإشارة إلى مصدر المنح والدعم المالي يكتبان في فقرة واحدة تسبق المراجع مباشرة.

Subscription Form

Jordan Journal of

# **PHYSICS**

An International Peer-Reviewed Research Journal issued by the Support of the Scientific Research Support Fund

Published by the Deanship of Research & Graduate Studies, Yarmouk University, Irbid, Jordan

Name:	الأسم:	
Specialty:	التخصص:	
Address:	العنوان:	
P.O. Box:	صندوق البريد:	
City & Postal Code:	المدينة/الرمز البريدي:	
Country:	الدولة:	
Phone:	رقم الهاتف:	
Fax No:	رقم الفاكس:	
E-mail:	البريد الإلكتروني:	
No. of Subscription:	عدد الإشتراكات:	
Method of Payment:	طريقة الدفع:	
Amount Enclosed:	المبلغ المرفق:	
Signature:	التوقيع:	
negues should be naid to Deanship of Research and Graduate Studies - Varmouk University		

I would like to subscribe to the Journal

#### For

- One Year
- Three Years

One Year Subscr	iption Ka	tes
Inside Iordan	Outside	Iorda

Inside Jordan	Outside Jordan
Individuals JD 8	€ 40
Students JD 4	€ 20
Institutions JD 12	€ 60

#### Correspondence

#### **Subscriptions and Sales:**

#### Prof. Ibrahim O. Abu Al-Jarayesh

Deanship of Research and Graduate Studies
Yarmouk University
Irbid – Jordan
Telephone: 00 962 2 711111 Ext. 2075

**Fax No.**: 00 962 2 711111 Ext. 2075



جامعة اليرموك

# المجلة الأردنية للفيزياء

مجلة بحوث علمية عالمية متخصصة محكّمة تصدر بدعم من صندوق دعم البحث العلمي



## المجلد (11)، العدد (2)، آب 2018م / ذو الحجة 1439هـ

المجلة الأردنية للفيزياء: مجلة علمية عالمية متخصصة محكّمة تصدر بدعم من صندوق دعم البحث العلمي، عمان، الأردن، وتصدر عن عمادة البحث العلمي والدراسات العليا، جامعة اليرموك، إربد، الأردن.

#### رئيس التحرير:

ابراهيم عثمان أبو الجرايش

قسم الفيزياء، جامعة اليرموك، إربد، الأردن. ijaraysh@yu.edu.jo

#### هيئة التحرير:

ضياء الدين محمود عرفة

رئيس جامعة آل البيت، المفرق، الأردن.

darafah@ju.edu.jo

نبيل يوسف أيوب

رئيس الجامعة الأمريكية في مادبا، مادبا، الأردن.

nabil.ayoub@gju.edu.jo

جميل محمود خليفة

قسم الفيزياء، الجامعة الأردنية، عمان، الأردن.

jkalifa@ju.edu.jo

سامى حسين محمود

قسم الفيزياء، الجامعة الأردنية، عمان، الأردن.

s.mahmood@ju.edu.jo

نهاد عبدالرؤوف يوسف

قسم الفيزياء، جامعة الأميرة سمية للتكنولوجيا، عمان، الأردن

<u>o n.yusuf@psut.edu.j</u>

مروان سليمان الموسى

قسم الفيزياء، جامعة مؤتة، الكرك، الأردن.

mmousa@mutah.edu.jo

أكرم عبد المجيد الروسان

قسم الفيزياء التطبيقية، جامعة العلوم والتكنولوجيا الأردنية، إربد، الأردن.

akram@just.edu.jo

محمد خالد الصغير

قسم الفيزياء، الجامعة الهاشمية ، الزرقاء، الأردن.

msugh@hu.edu.jo

#### سكرتير التحرير: مجدي الشناق

#### ترسل البحوث إلى العنوان التالي:

الأستاذ الدكتور إبراهيم عثمان أبو الجرايش رئيس تحرير المجلة الأردنية للفيزياء عمادة البحث العلمي والدراسات العليا، جامعة اليرموك إربد ، الأردن

هاتف 7211111 2 962 00 فرعى 2075

E-mail: jjp@yu.edu.jo Website: http://Journals.yu.edu.jo/jjp